Chip geometry, cutting force, and elastic deformation prediction for gear hobbing

by

Milad Azvar

A thesis
presented to the University of Waterloo
in fulfillment of the
thesis requirement for the degree of
Doctor of Philosophy
in
Mechanical and Mechatronics Engineering

Waterloo, Ontario, Canada, 2023

Author's Declaration

I hereby declare that I am the sole author of this thesis. This is a true copy of the thesis, including any required final revisions, as accepted by my examiners.

I understand that my thesis may be made electronically available to the public.

Abstract

The machining industry is constantly challenged through increasing demands for productivity and stringent part quality requirements such as dimensional accuracy and surface quality. Physics-based models are becoming more commonly employed in the manufacturing industry for traditional machining processes like turning, milling, and drilling. By utilizing such models, machining process planners can optimize productivity while preserving or improving part quality, through virtual manufacturing of the components ahead of time via realistic simulations. In this context, cutting force prediction models are essential for machining process simulations. For traditional machining operations, where the cutter and workpiece geometries and kinematics are simple, cutting forces can be calculated via analytical equations. However, in complex processes like 5-axis milling, turn-milling and gear machining, the cutter-workpiece engagement is very complex and is best calculated using geometric CAD modelers. This engagement information allows for cutting forces along the cutting edge of the tool to be computed and summed up. Modeling the cutting forces also provides insight into the torque/power requirement, elastic deformation, vibrations, and machining stability (chatter) during the process, which are the primary factors that contribute to dimensional inaccuracies, surface location errors, and poor surface finish. By integrating these models, a comprehensive physics-based approach to machining processes can be developed, allowing for accurate simulation, prediction, and optimization of part quality. The main objective of this thesis is to establish the very first steps of such an integrated simulation environment for the gear hobbing process, by investigating the efficient prediction of cutting forces and elastic deformations.

Hobbing is a high-speed and accurate gear cutting process used extensively to produce external gears – which are essential components in power transmission, automotive, aerospace, and automation (e.g., robotics) applications. The hobging process involves feeding a rotating cutting tool (known as a 'hob') into a workpiece (referred to as blank gear) that is rotating while the two are meshed together, as would be in worm-gear mechanism. This results in the continuous removal of chips during the process. Unlike conventional machining operations, hobbing has complex tool and workpiece geometries, and complicated

kinematics with multi-axis motions. In this thesis, a mathematical model of the hobbing kinematics is developed and validated through collected CNC signals obtained using the Siemens 840D controller of Liebherr LC500 hobbing machine.

The cutter-workpiece engagement is calculated using an efficient discrete geometric modeler in tri-dexel format. Using Delaunay triangulation and alpha shape reconstruction, the 2D cross-section of the uncut chip is created from its internal data. This cross-section is then utilized to approximate the local chip geometry along the discretized cutting edge of the tool. Each node along the cutting edge represents a generalized oblique cutting force model with specific rake and inclination angles, and principal directions (i.e., tangential, feed, and radial). At each time step, the incremental forces for the engaged cutting edge nodes are computed and ultimately integrated to obtain the total cutting forces. Using a rotary dynamometer, the proposed cutting force model has been validated through cutting trials on a Liebherr LC500 CNC hobbing machine. The tests involved cutting of several spur and helical external gears with varying process parameters in single and two-pass processes. The model reasonably captures the overall behavior of the measured forces, min/max force envelopes and cutting strokes with the RMS error being 7-21% for roughing passes and 24-36% for finishing passes throughout the tests, which is reasonable for machining process planning. In the finishing cut, due to the forces being smaller, the signal-to-noise ratio and apparent prediction accuracy are worse.

The elastic deformation is modeled based on the static stiffness of the tooling and workpiece assemblies. The stiffness is approximated from experimentally-measured mechanical frequency response functions (FRFs). The expected elastic deformations are computed by dividing the cutting forces by the static stiffness values. The calculated deflections are then used to superpose the tool's nominal position in the time-domain simulation of the gear machining operation, thereby gears to be 'virtually-machined' with errors originating both from the kinematics of the hobbing feeding process, as well as the mechanical elastic deformations. The virtually-produced gears are then measured according to the ANSI/AGMA standard for gear inspection, using the integrated gear cutting simulation and metrology software developed at the University of Waterloo, and the prediction results are compared with the quality inspection measurements taken from physically machined gears, using a

v

GLEASON 300GMS Lead & Involute Checker. The lead deviation predictions showed good correlation, while profile deviations require further research.

Overall, this thesis has achieved a detailed physics-based model for hobbing, which focuses on the kinematics, chip geometry, cutting forces, and elastic deformation. Future research will explore error sources in the cutting force model prediction, enhancing the elastic deformation model, and developing models for vibrations and chatter.

Acknowledgements

This thesis would not have been possible without the support, guidance, and encouragement of several individuals and organizations. First and foremost, I express my sincere gratitude to my supervisor Professor Kaan Erkorkmaz for his unwavering support, invaluable ideas, and enthusiasm throughout my studies. His expertise and guidance played an instrumental role in enabling me to achieve my research objectives.

My gratitude also goes to my colleague at the Precision Controls Lab, University of Waterloo, Mr. Andrew Katz, whose research on modeling gear shaping laid the groundwork for my own research on modeling gear hobbing. His invaluable support and guidance were pivotal to the success of my work.

I extend my appreciation to my thesis committee members, Professor Hans-Christian Moehring, Professor Sriram Narasimhan, Professor Duane Cronin, and Professor Fathy Ismail, for taking the time to read my thesis and providing constructive feedback.

I would like to extend my appreciation to Ontario Drive & Gear (Bob Reiter, Jacob Van Dorp, Iulius Jora, Jacob Dickie, and all other team members) for their kind support in sponsoring this project and offering invaluable resources such as machine time, materials, tools, and expert knowledge. These contributions played a crucial role in the successful completion of my research, and I am truly grateful for their generosity.

I am also grateful to the technical staff at MME, particularly Karl Janzen, Jason Benninger, and Robert Wagner, for their assistance with the experimental setups.

Lastly, I extend my heartfelt appreciation to my colleagues at the Precision Controls Laboratory, my friends, my family and my wife for their unwavering support during my degree program.

Dedication

To my beloved wife, supportive parents and loving sisters.

Table of Contents

List of Figures

xv

xvi

xvii

xviii

List of Tables

Chapter 1

Introduction

1.1   Background

Gear hobbing is a machining process that is used to produce accurate spur and helical external gears. This process involves the use of the hob, which is a cutting tool with teeth that shaped like those of a worm-gear. The hob is rotated and fed into a rotating blank gear, cutting away excess material and leaving behind the desired gear shape (see Figure 1.1 which illustrates three of the most widely used gear machining processes).
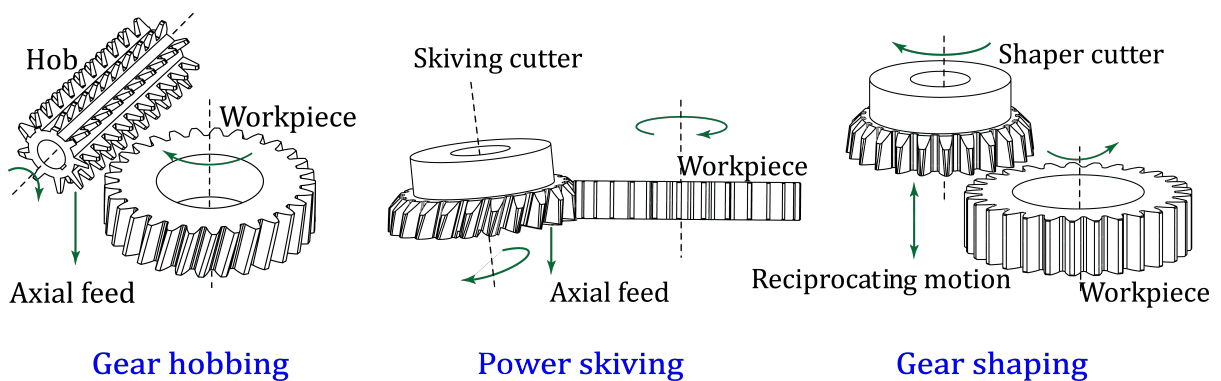
Figure 1.1: Schematic overview of different gear-cutting processes

In general, gear hobbing is a more efficient manufacturing process than gear shaping, which loses time due to its reciprocating action, and it is also more rigid compared to gear power skiving, which necessitates a motion delivery elements than introduce extra structural flexibility. However, due to the hob geometry and its alignment with the workpiece, the hobbing process is not suitable for producing internal gears. Despite this limitation, hobbing is a versatile operation that can be used to manufacture a variety of externally-toothed gears, such as spur, helical, spiral, or worm gears [1].

It is crucial to have a thorough understanding of the underlying physics behind hobbing, given its extensive use in gear manufacturing. Gears are used in nearly every industry sector, including automotive (e.g., E-vehicles), aerospace, energy production, automation (e.g., robotics) and many others. By fully understanding a gear machining process, a physics-based model can be developed which ultimately assists process planners to efficiently design and optimize processes, in order to improve or maintain accuracy requirements, while reducing the cycle time, and energy consumption. This is also a step toward Industry 4.0 objectives, where reliable production with minimum human interference can be achieved [2].

1.2 Thesis Objective

Physics-based models for the gear hobbing operation have been developed with an emphasis on cutting force prediction. As with other metal cutting methods, the cutting force in hobbing is directly proportional to the amount of material removed from the workpiece by the cutter. Force prediction is also at the heart of predicting other process attributes and outcomes, such as power/torque consumption, and final part quality. In machining terminology, the geometry of the removed material is often referred to as the Cutter-Workpiece-Engagement (CWE). In hobbing, most of the studies focus on the prediction of cutting forces using solid modelers as CWE calculators. Although highly precise, in solid modeling engines, complex equations (of the spline curves or surfaces) must be solved analytically to obtain intersection information, which makes them computationally inefficient, especially

as the complexity of the workpiece increases with successive cutting motions. Additionally, physics-based models have not yet been developed to predict the elastic deformations, vibrations, and their effect on the finished gear quality.

This thesis aims to develop a comprehensive hobbing model which uses a discrete geometric modeler to calculate CWE. Discrete modelers approximate the cutter and workpiece utilizing orthogonal lines (dexels) or cubes (voxels), which allow for simple and time-efficient 3D intersection calculations. Discrete geometric modelers provide computational efficiency which make them suitable to be used in CAD/CAM software and be successfully embedded inside Industry 4.0 type systems. Motivated by these ideas, the main objectives of this thesis have been to:

- Develop cutting force model for gear hobbing operation using a tri-dexel discrete geometric modeler

- Model the elastic deformation of the cutter and workpiece, and their influence on the finished gear quality

The components of the developed virtual model are shown in Figure 1.2.

1.3 Thesis Layout

The existing literature on conventional metal cutting operations as well as gear machining is reviewed in Chapter 2. In conventional cutting operations (e.g., turning, boring, milling and drilling), analytical expressions can be used to describe the uncut chip geometry. Thus, the cutting forces can be predicted analytically. This allows the employment of analytical methods to model elastic deformations, vibrations, chatter stability, and finished part quality. However, analytical models are limited and inefficient in modeling processes where the tool path or the workpiece geometry is complicated (e.g., in 5-axis machining of an airfoil), and in operations where the CWE is complex (e.g., in gear cutting via generative methods, like shaping, hobbing, and power skiving). In such processes, it is practical to use

geometric modelers in extracting the CWE information. After reviewing the gear hobbing literature, it has been found that there is a lack of a comprehensive physics-based model which can be utilized efficiently and fast computational speeds.

The kinematic model of the gear hobbing is described in Chapter 3. The kinematic model is a vital component in achieving the cutting force prediction, since it defines the precise multi-axis cutting motion. The mathematical model is established based on the geometry of the hob and workpiece, as well as the process parameters (e.g., cutting speed, feeding strategy, feedrate values, depth of cut, number of passes). In this context, homogeneous matrix transformations are used to represent the position of each point located on the cutting edge of the tool in different coordinate systems, such as the tool, workpiece, and machine coordinate systems (TCS, WCS, and MCS). The simulated kinematic model is compared with the captured CNC (Computer Numerical Control) data of a Liebherr LC500 CNC hobbing machine during cutting trials and good agreement is observed. The kinematic model is also coupled with the tri-dexel based simulation engine, which was then verified to produce the expected gear geometries.

In Chapter 4, the calculation of CWE and the prediction of cutting force are explained. This is the core chapter of this thesis. The chapter begins with extraction of the uncut chip geometry, which is necessary for the calculation of the cutting forces. To simulate the material removal process and CWE, the ModuleWorks engine is utilized, which is an efficient and robust commercial tri-dexel discrete modeler, utilized in CAM (Computer-Aided Manufacturing) software. At every time step, the CWE information is populated as a 3D point cloud. The 3D point cloud encapsulated by contours is intersected with the hob's rake face to form a 2D point cloud. Then, Delaunay triangulation is applied to the point cloud, creating a convex hull. Finally, alpha shape reconstruction is used to estimate the uncut chip geometry in 2D. The chapter then proceeds to explain the developed cutting force model. With the knowledge of the kinematics, the model is able to successfully resolve the local inclination and normal rake angles along the discretized length of the cutting edge, as required by the oblique cutting force model. The localized 2D chip geometry and cutting conditions (e.g., rake and inclination angles) are used in a generalized oblique cutting force model to predict the forces in three principal directions

(i.e., tangential, feed and radial) along each discretized node. The overall cutting forces are obtained through the summation of these incremental force contributions.

Chapter 5 discusses the validation of the proposed cutting force model via gear hobbing cutting tests. Due to the complex geometric topology and kinematics of the hobing process, direct measurement of cutting forces is very challenging and has rarely been implemented in literature. In this thesis, the cutting forces were measured with a Kistler 9123C rotary dynamometer (originally designed for milling) that was attached with a specially designed apparatus to a Liebherr LC500 hobbing machine using. To compensate for measurement distortions caused by the vibrations of the fixture/dynamometer assembly, Kalman Filtering technique was implemented. Using a small portion of the data (i.e., only 40 seconds of a 200 second trial), the parameters of different cutting force models were calibrated. The identified parameters were then used to simulate the forces for all of the cutting trials, which involved spur and helical gears machining with different axial feed rates in single- and two-pass processes. The prediction results are in good agreement with the measurements throughout the cutting trials, with the root mean square (RMS) error ranging from 7-20% for roughing passes and 24-36% for finishing passes, which is considered reasonable in industrial machining process planning. Additionally, the accuracy with the three different cutting force models developed in Chapter 4 are compared, and it is shown that the Kienzle model exhibited the best performance.

Chapter 6 introduces a model for calculating the elastic deformation of the hob and the gear. The static stiffness of the hob and gear are determined through impact hammer testing. This test provides an estimate of the stiffness, which is used to calculate the bending deflection of the components based on the cutting forces. After production, gears from two different setups were inspected on a GLEASON 300GMS Lead & Involute Checker and compared with the virtual gear quality predictions obtained with the elastic deformation model – as evaluated using University of Waterloo's integrated gear cutting simulation and virtual metrology software. The results from virtual gear metrology exhibited a good correlation with the actual measurements in predicting the lead errors. However, additional research is still necessary to enhance the predictions for profile deviations. Nevertheless, this thesis presented for the first time an integrated hobbing process simulation environ-

ment, based on discrete geometric modeling, which achieves both force and part quality prediction.
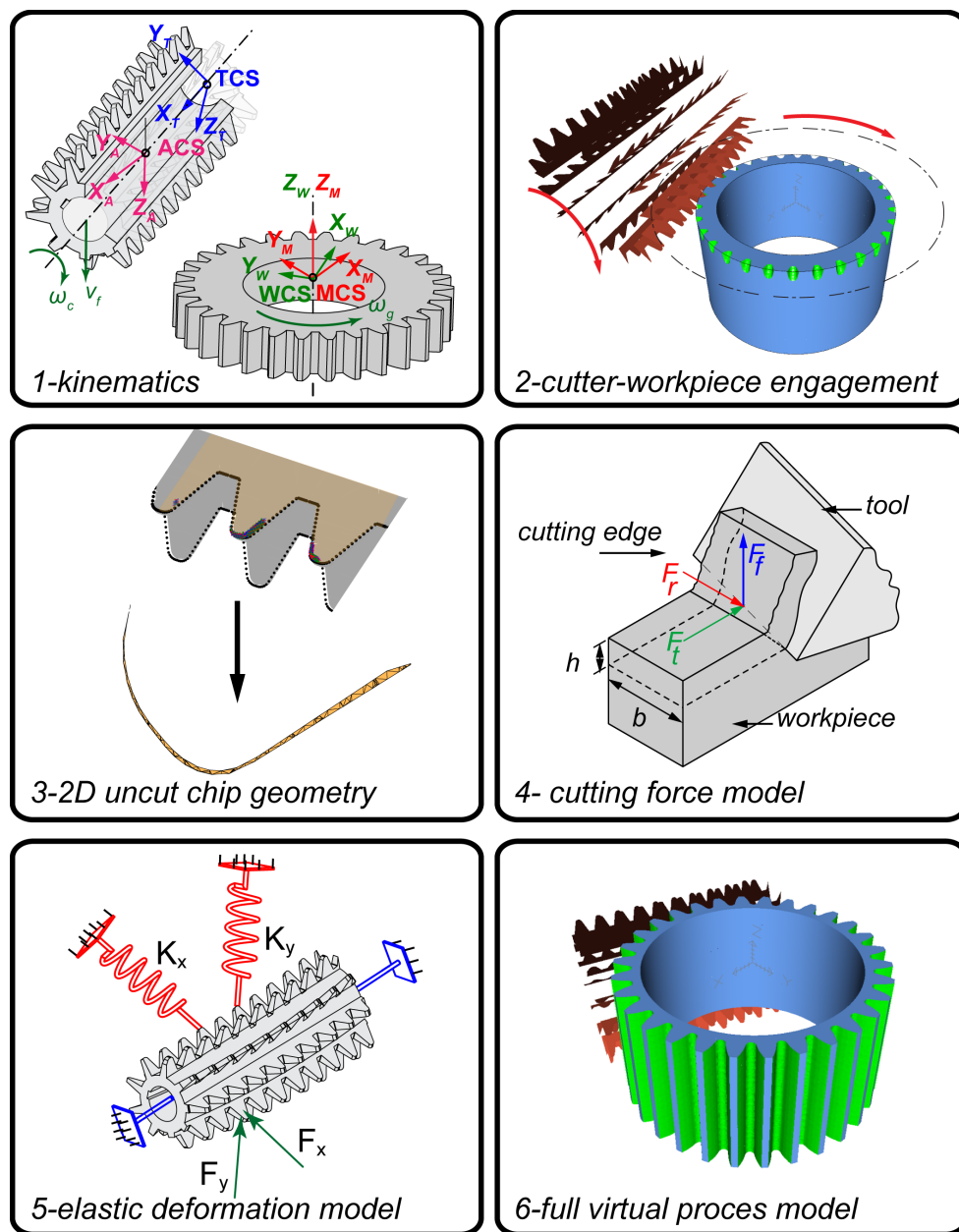
Figure 1.2: Components of a comprehensive virtual model for gear hobbing

This thesis makes the following contributions:

- Development of a cutting force model using a multi-dexel geometric engine, which provides a comprehensive understanding of the forces involved in the hobbing process. This model takes into account various factors such as tool and gear geometry, material properties, and cutting parameters, allowing for accurate predictions of cutting forces.

- Development of an elastic deformation model, which considers the deflection of the workpiece and tool during the hobbing process. This model helps to analyze the effects of cutting forces on the manufactured gear quality, enabling a better understanding of the process and the potential for improving the machining performance.

- Measurement of cutting forces in hobbing using a rotary dynamometer, addressing a gap in reported literature for this process. This has been achieved by developing a specialized mounting fixture, applying dynamics (modal) analysis, and Kalman filtering to correct for measurement distortions due to structural vibrations. Direct cutting force measurements provided deeper insights into the hobbing process, and also the validation of the developed simulation model.

Chapter 2

Literature review

2.1   Introduction

Since the beginning of the new century, novel manufacturing techniques, along with material sciences, more advanced automation, and computational capability, have achieved significant progress [3]. While there have been improvements in additive and hybrid manufacturing, metal-cutting processes are still the preferred method in most manufacturing industries due to their higher productivity, better quality finished parts, and well-understood physics. That being said, the perpetual demand of manufacturers for enhanced productivity while maintaining part quality, challenges researchers to advance beyond current machining technology.

Several factors may limit the productivity and quality of the machined workpieces. Among them, chatter vibrations, forced vibrations, and elastic deformations are of utmost importance due to their catastrophic threats to the process productivity, quality of the parts, and in severe cases the machine tool itself. To address these limitations, researchers have created physics-based models that simulate machining processes to predict process stability and finished part quality before cutting the actual part on a machine tool. These models can eliminate the expensive process of trial and error and assist the machining engineer in properly selecting the process parameters such as feed rate, depth of cut,

and spindle speed. Physics-based models for the common cutting processes (e.g., turning, boring, milling, and drilling) have been thoroughly developed, and systematically are being applied in industry. The research in gear hobbing, however, is still in its nascent stages, primarily because of the complicated geometry and kinematics of the process. This chapter starts with reviewing the existing physics-based model for common metal cutting processes in Section 2.1.1 and then continues with covering these models for gear cutting processes in Section 2.1.2.

2.1.1 Common metal cutting processes

2.1.1.1 Cutter-workpiece engagement calculation

The primary objective of physics-based models has been to determine the uncut chip geometry. Accurate resolution of uncut chip geometry allows for cutting forces, elastic deformations, stability, and finished part quality predictions. In cutting processes wherein the governing kinematics and cutter-workpiece engagement (CWE) are simple, uncut chip geometry is approximated analytically. For example, in orthogonal turning of tubes, uncut chip thickness is simply equal to the axial feed rate of the cutting tool. In turning operation, however, the uncut chip thickness depends on the axial feed rate, depth of cut, and the insert's geometry as well (see Figure 2.1). For general turning, Enders [4] presented an analytical expression for uncut chip thickness in which the effects of the insert's true geometry, axial feed rate and radial depth of cut, are considered (see Figure 2.2.a). As an alternative approach, Ozlu [5] divided the cutting edge of the insert into small segments and summed the uncut chip area of each segment to obtain the total chip area. The extraction of uncut chip geometry in boring operation is similar to that of turning operation due to their similar kinematics and CWE mechanism. Lazoglu [6], for instance, discretized the cutting edge of the boring bar into several elements and determined the local uncut chip area considering the effects of the axial feed rate, depth of cut, and the insert's nose radius and side edge cutting angle. Despite being a more complex and time-varying process, it is possible to use a similar approach to calculate the CWE in milling. To achieve this, the

9
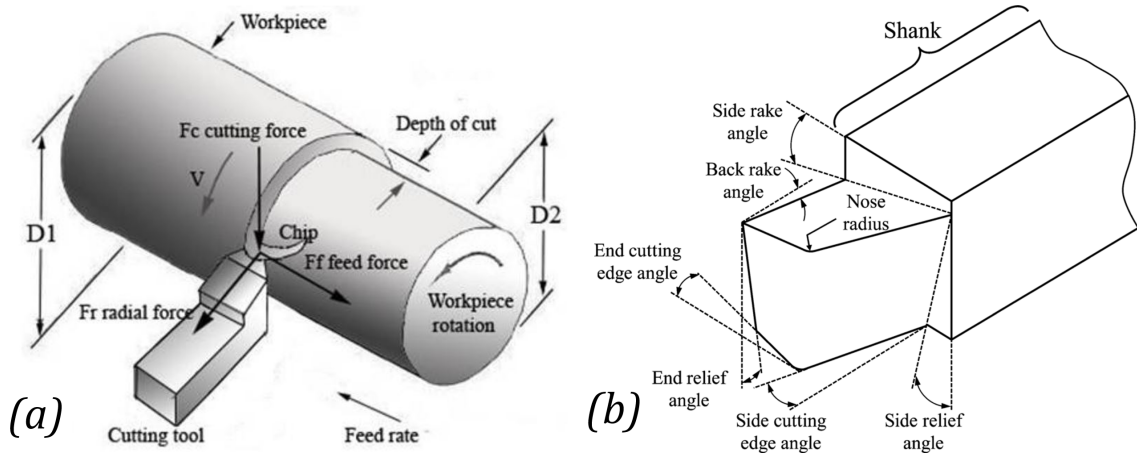
Figure 2.1: (a) Turning operation, (b) True geometry of the insert [3]

length of the mill is discretized into smaller segments and at any time step (small rotation of the cutter), the contribution of each segment to the total chip thickness is integrated (see Figure 2.2.b). This method has been also applied to the face milling [7][8], helical end milling [9][10] and ball end milling [11][12][13] operations. Despite the increased complexity
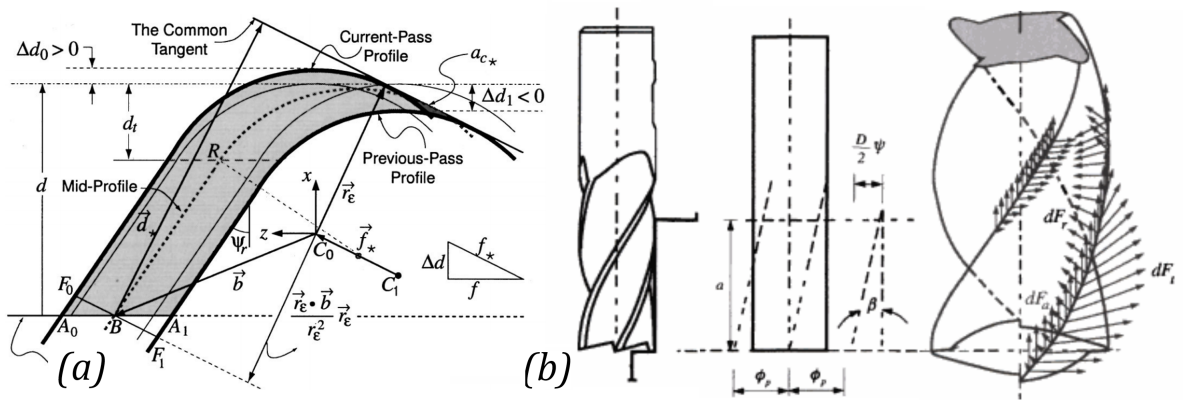
Figure 2.2: (a) uncut chip geometry in turning [4], (b) discretized helical end mill [3]

in the analysis of 5-axis milling, which involves the effects of the tilt and lead angle of the mill, an analytical model for the uncut chip geometry is introduced by Ozturk [14]. A similar approach is adopted in the extraction of the uncut chip geometry in drilling [15],

10

orbital drilling operation [16] and multi-point thread turning [17]. Kaymakci [18] presented a generic model for extraction of uncut chip geometry in turning, boring, drilling, and milling operations with inserted tools. Analytical representations of uncut chip geometry are available for various machining operations. It is worth noting though, it is necessary to sufficiently simplify the geometries of the workpiece, cutter, and tool path in order to obtain such models.

As an alternative to analytical approaches, geometric (also called solid) modeling kernels which include exact and discrete-based engines can be used. These kernels are most suitable to be embedded in CAD/CAD software wherein free-form geometries (e.g., airfoils and turbine blades) are programmed to be machined in long and complicated tool paths. In such operations, the kinematics of the process is complex, and therefore, the CWE is irregular and time-varying rendering analytical derivation rather difficult. In exact solid modelers (e.g., Parasolid and ACIS), the tool and workpiece are represented as continuous volumes using mathematical equations. These representations can be mainly done in two ways: (1) using Constructive Solid Geometry (CSG), and (2) using Boundary Representation (BREP) [19]. In the CSG-based CWE calculation, the swept volume is represented by Boolean operations (i.e., union, difference, intersection) of primitive geometries such as cubes, spheres and cylinders (for example, [20]). In the BREP-based CWE calculation, the boundaries of the cutter and workpiece (e.g., surfaces, vertices, B-splines and circular edges) are intersected analytically over the length of the tool path. For instance, Larue [21] modeled the geometry of a tapered ball end mill analytically for the flank milling process and determined the immersion angles over the course of the tool motion. Then, the CWE is determined by intersecting the cutter surface with workpiece surface in ACIS. In a similar manner, this method has been applied to the CWE calculation of 3-axis milling [22][23][24] and 5-axis milling [25] (see Figure 2.3.a). In exact modelers, the engagement calculations have to be performed at every cutter location point; hence, it requires intensive numerical computations.

In contrast to exact modelers, discrete modelers represents the workpiece and tool geometry approximately. One such discrete model is the multi-dexel representation in which the workpiece and tool are represented using a series of orthogonal 3D line seg-

11
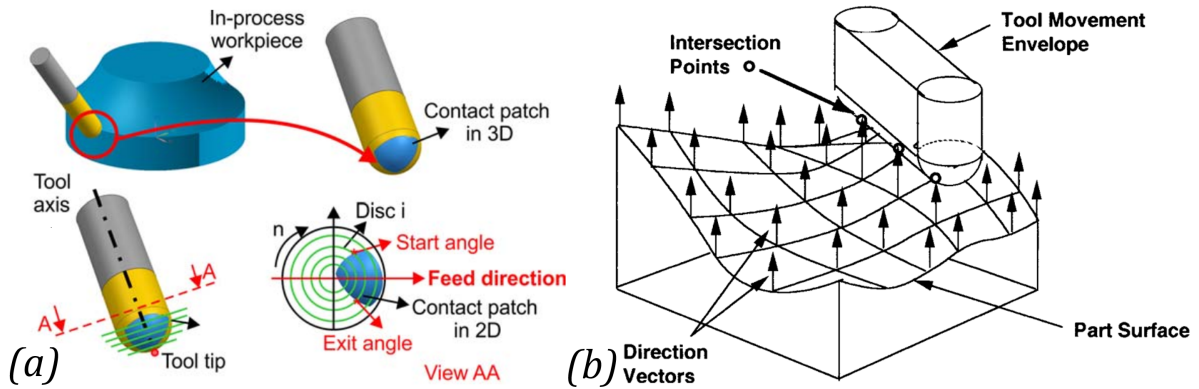
Figure 2.3: (a) CWE calculation in 5-axes milling using BREP [25], (b) Representing the workpiece geometry using the Z-buffer method [26]

ments. Based on the swept volume of the tool, the dexels of the workpiece are updated (shortened, removed or split) [27], and then the engagement calculations are performed. Dexel-based representation is the extension of the Z-buffer method [28] wherein a series of one-dimensional lines determine the boundary of the geometries, as shown in Figure 2.3.b. Works of Fussell, [29] and [26], are the exemplary application of discrete modelers in the CWE calculations of 3-axis and 5-axis milling using the Z-buffer method, respectively. Recently, Comak [30] used MACHPro-Virtual Machining [31] software, which uses a tri-dexel-based engine, to extract the CWE in turn-milling operation, which is more complex than the conventional turning or milling due to the simultaneous rotation of the cutter and workpiece. Due to the analytical schemes used in exact modelers, CWE can be accurately determined at the expense of computational effort, whereas discrete modelers approximate the CWE in a faster manner. The main advantage of these geometric kernels is realized when they are coupled with physics-based cutting models in CAD/CAM software. When implemented successfully, it allows complex geometries and tool paths to be virtually machined in parallel with the physics of the cutting process. This is a step toward meeting the stringent requirements of the industry, as it enables precise process simulation, analysis, and optimization.

2.1.1.2 Cutting force models

With knowledge of the CWE and uncut chip geometry, the cutting forces are predicted using available cutting force models. The magnitude of cutting forces are related to chip thickness and width of cut by cutting force coefficients. The orthogonal cutting model is the simplest model which is based on 2D mechanics of metal removal [32], and is often used to explain the general case of cutting mechanics. For example in the simple case of
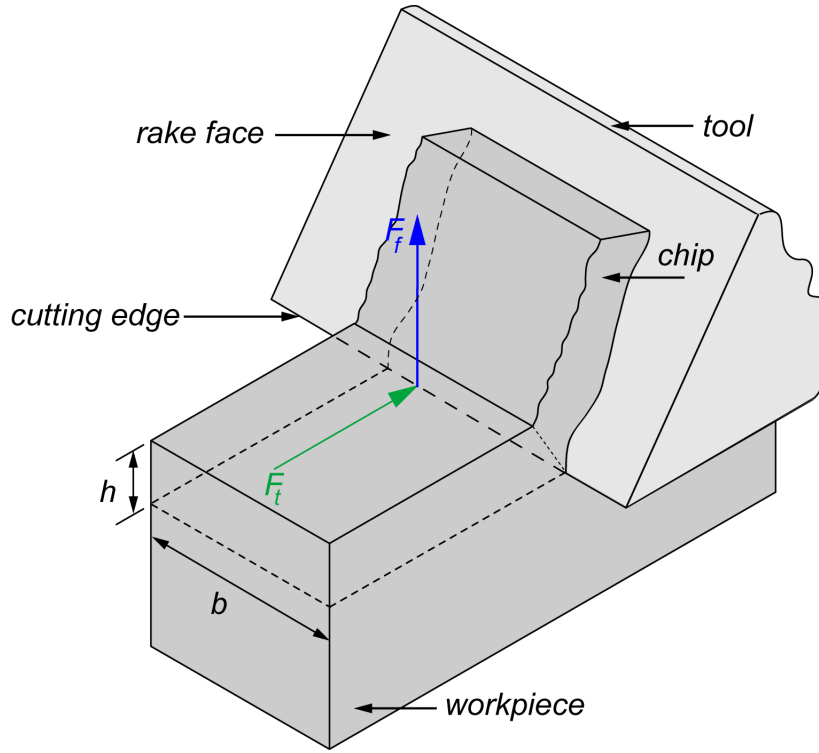
Figure 2.4: Orthogonal cutting force model (adopted from [3])

tube turning, the orthogonal cutting model can accurately capture the forces in the feed (F_f) and tangential (F_t) directions as shown in Figure 2.4.

$$
\begin{aligned}
F_t &= F_{tc} + F_{te} = K_{tc}bh + K_{te}b \\
F_f &= F_{fc} + F_{fe} = K_{fc}bh + K_{fe}b
\end{aligned}
\tag{2.1}
$$

13

where b and h are the chip width and thickness, respectively. Also, K_{tc}, K_{fc}, K_{te} and K_{fe} are cutting force and cutting edge coefficients in their respective directions.

Yet, most cutting operations are governed by 3D physics, and can only be accurately modeled using the general oblique cutting model. In this model, the mechanics of cutting process are described in three distinct directions (i.e., tangential (F_t), feed (F_f) and radial (F_r) as shown in 2.5) [3].
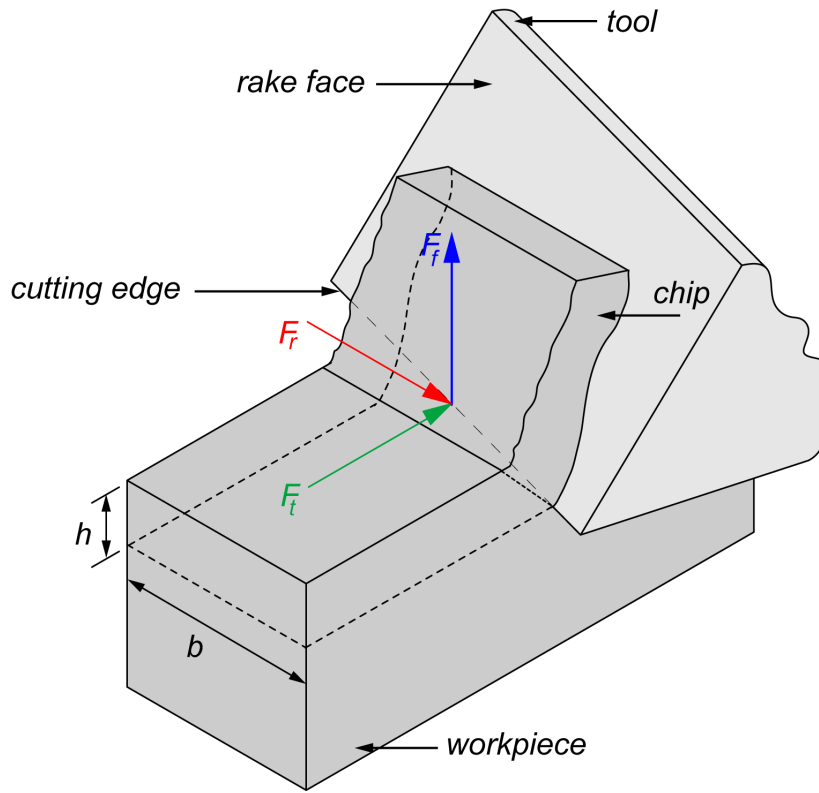
Figure 2.5: Oblique cutting force model (adopted from [3])

$$
\begin{aligned}
F_t &= F_{tc} + F_{te} = K_{tc}bh + K_{te}b \\
F_f &= F_{fc} + F_{fe} = K_{fc}bh + K_{fe}b \\
F_r &= F_{rc} + F_{re} = K_{rc}bh + K_{re}b
\end{aligned}
\tag{2.2}
$$

Above, K_{rc} and K_{re} are the cutting force and cutting edge coefficients, respectively. The tangential and feed equations and parameters are similar for the oblique and orthogonal cutting force models.

There are two main approaches in determining the cutting force coefficients: a mechanistic approach and an orthogonal-to-oblique transformation approach[1][33]. In the mechanistic approach, the coefficients are directly determined in cutting tests for each combination of workpiece material and tool geometry. In the orthogonal-to-oblique transformation approach, fundamental of oblique cutting analysis is used in parallel with basic cutting parameters from orthogonal database to establish coefficients for various tool geometries. Although the mechanistic model is the most accurate, it requires a significant amount of testing for each material-tool geometry pair. In contrast, the orthogonal-to-oblique transformation method provides insights into the physics of the process, reduces the number of testings, and can still yield acceptable results [33]. Cutting force models are simplified assumptions of the cutting process, often neglecting nonlinearities or representing their effects with bulk terms / parameters. However, these models and cutting force coefficients may ultimately not be able to capture the complexities in full, leading to deviations between predicted and actual forces. In such cases, having additional calibration data partially ameliorates this shortcoming. While this section has provided an overview of the basic principles, Chapter 4 will further discuss the available cutting force models and methods for determining cutting force coefficients.

2.1.1.3   Form errors due to elastic deformations

Dimensional form errors are one of the main factors in finished part quality. In practice, the tool and workpiece are not rigid, and therefore, they deviate from their nominal positions during the cutting process causing poor part quality. For milling operation, Budak [34] modeled the end mill as a cantilever beam and calculated the elastic deformation of the tool under the static cutting forces (see Figure 2.6). The predicted deflection of the tool is translated as dimensional errors on the workpiece. Later, Budak [35] improved the

---

[1]it is also called mechanics of cutting approach
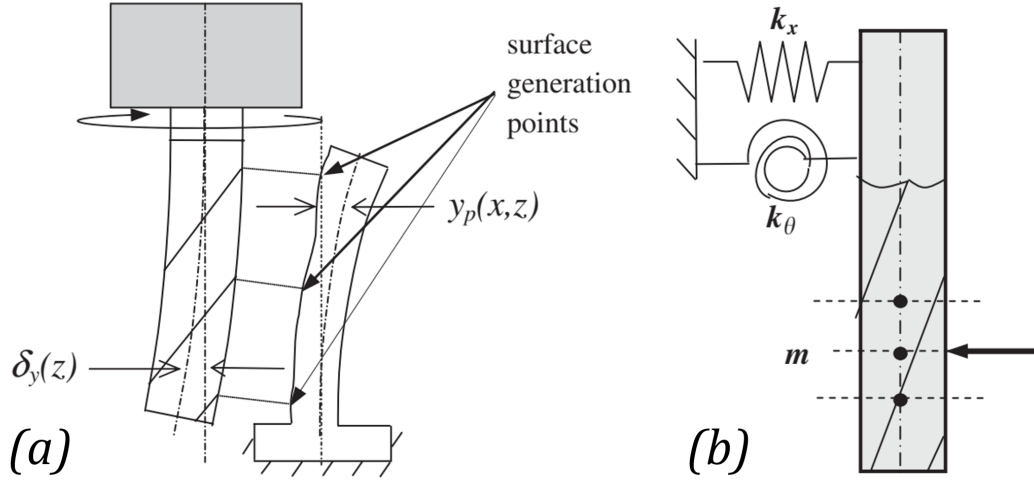
Figure 2.6: (a) Elastic deformation and imprinted surface in milling, (b) torsional and bending stiffness modeling of an end mill [9]

model presented in [34] to account for the effects of varying workpiece dynamics during peripheral milling of flexible plates. To achieve this, a Finite Element (FE) model of the plate is created and nodal displacements are approximated from nodal cutting force and stiffness matrices. In each feed location, the stiffness matrix is updated to include the variable workpiece dynamics. Effects of different process parameters on the machined surface are investigated which allowed for controlling the accuracy of the machined part while maintaining the Material Removal Rate (MRR). Based on Budak's works in [34] and [35], several researchers attempted to improve the surface error predictions by using higher order tool deformation theories [36], improving the FE model [37] and enhancing the computational efficiency [38].

2.1.1.4 Vibrations in machining

Surface finish quality is also a decisive factor in determining the finished part quality. As opposed to form errors, poor surface finish can originates from vibrations of the cutter and workpiece. Vibrations may also lead to reduced productivity, and in severe cases may

16

result in tool failure or machine tool damage. There are two main categories of vibrations that occur during the cutting process: (1) chatter (regenerative or self-excited) vibrations; and (2) forced vibrations.

Chatter is a self-excited vibration which initiates when one of the natural modes of the system is excited by the cutting forces. Take orthogonal turning process as an example as shown in Figure 2.7. When the cutting tool vibrates, it leaves a wavy surface on the part (inner modulation) which will be cut in the next revolution of the workpiece (outer modulation). The oscillations results in a time-varying chip thickness (also called dynamic chip thickness $h(t)$), which in turn creates vibratory cutting forces. The phase difference between in inner and outer modulation (ϵ) is the most important factor in the regeneration process which depends on the cutting conditions and dynamic characteristics of the system [39]. If the phase shift between the subsequent surface waves is very small, the system will remain stable while producing a wavy-surfaced part. If the waves are out of phase, however, the magnitude of the cutting force grows, and the system will become unstable. Regenerative chatter can be modeled as a positive closed feedback loop block diagram (see Figure 2.7). In this model, the vibration of the tool at the current time $y(t)$ is subtracted from its vibration at one revolution before $y(t - T)$ to obtain the dynamic chip thickness. In Figure 2.7, K_f and a are the cutting force coefficient and depth of cut, respectively. Also, m, c and k are the mass, damping and stiffness of the structure, respectively.

The theory of regenerative chatter was developed by Tlusty and Polacek [40] for a simple but practical case of orthogonal turning, and then improved for milling [41]. To improve the performance of these models, a truncated time-domain model was presented in [42] that captured the real physics of chatter vibration in milling. For the first time, Altintas and Budak [43] presented an analytical solution for the chatter problem in milling by establishing a relationship between chatter frequency and spindle speed. By only including the constant factor in the Fourier series expansion, which is called Zero Order Approximation (ZOA), of time-varying terms they constructed the stability lobe diagrams (SLD) in a fast manner[2]. The ZOA approximation only holds in milling with high immersion cutting conditions. To develop the SLD for low immersion cutting cases, Budak,

---

[2]SLD assist the machinist to select a pair of the spindle speed and depth of cut to ensure a stable cut
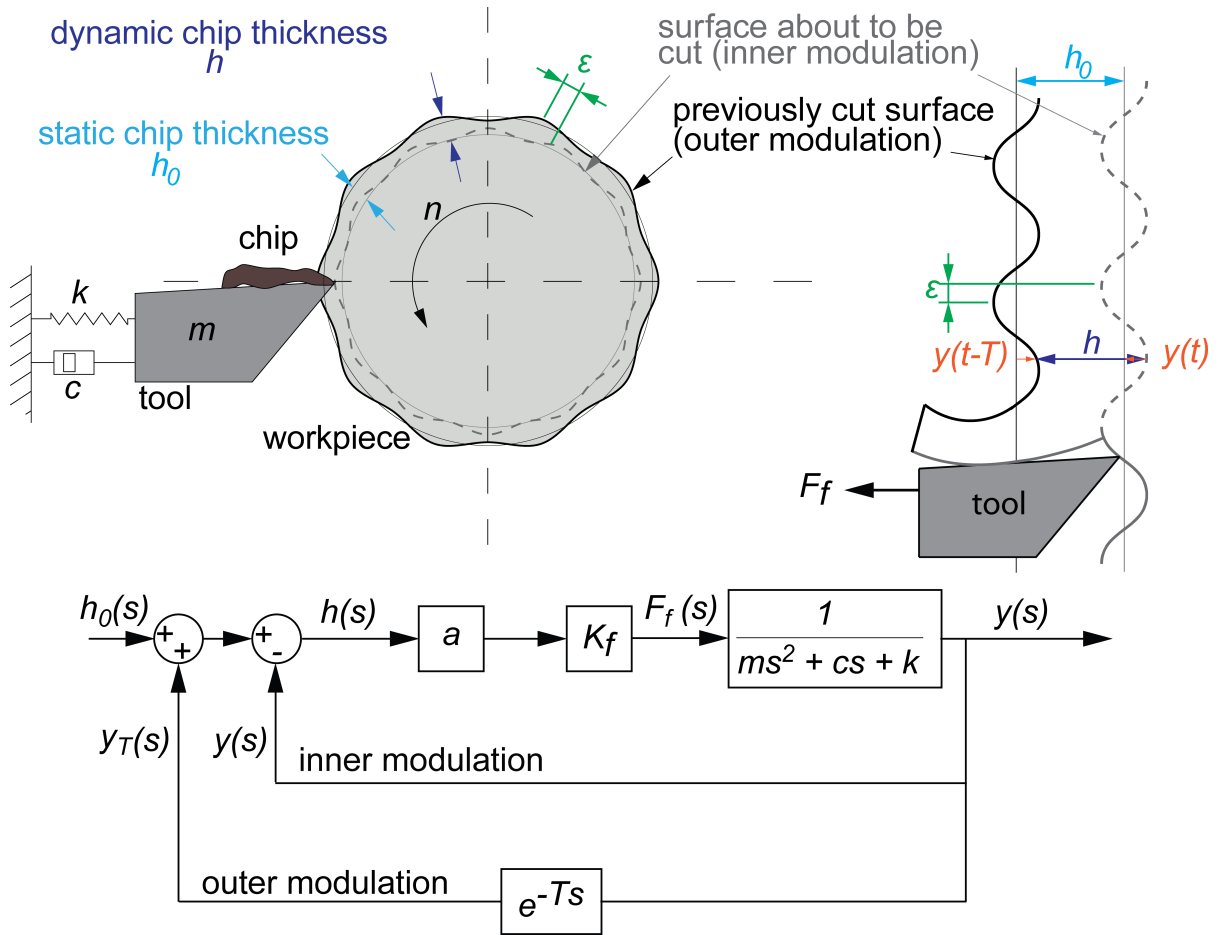
Figure 2.7: Self-excited chatter vibration in orthogonal cutting for a single degree of freedom system (adopted from [3])

in [44] and [45], included a higher number of harmonics in the Fourier series expansion of the time-dependent factors. Using similar approaches, the chatter problem was also investigated for 5-axis milling [46][14], turning [5][47], drilling [48][49] and boring [5].

The dynamics of the milling process can greatly affect its efficiency, with chatter being a major cause of poor surface quality due to large forces and displacements. However, productivity can also be restricted by forced vibrations that cause surface location errors, or

---

for a specific cutting process
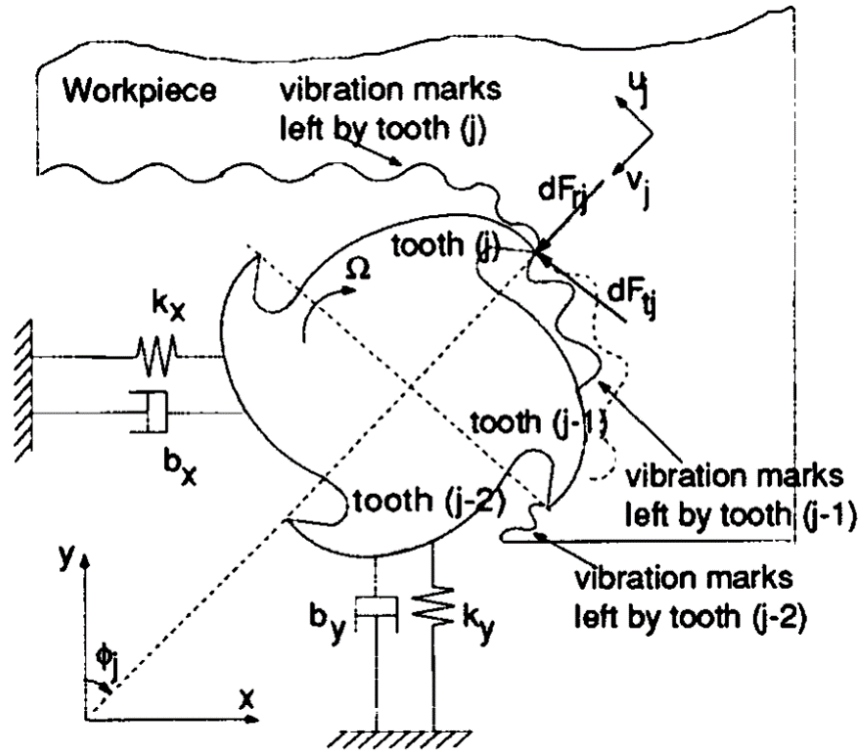
Figure 2.8: Regenerative chatter mechanism in milling operation [43]

inaccuracies in the geometric shape of the workpiece resulting from the tool's dynamic displacements during stable milling. In fact, every stable milling operation experiences forced vibration in varying degrees. The synchronous vibration of the cutter results in surface location error (SLE) as shown in Figure 2.9 [50]. As opposed to chatter, in synchronous forced vibration, the tool is in the same position each time it creates a new surface, resulting in a smooth but overcut or undercut part. As the frequency of the forcing function approaches a vibration mode of the system, the magnitude of SLE increases. The negative effect of forced vibration during stable milling can be alleviated by modifying the tooth passing frequency which can be accomplished by changing the spindle speed.

19
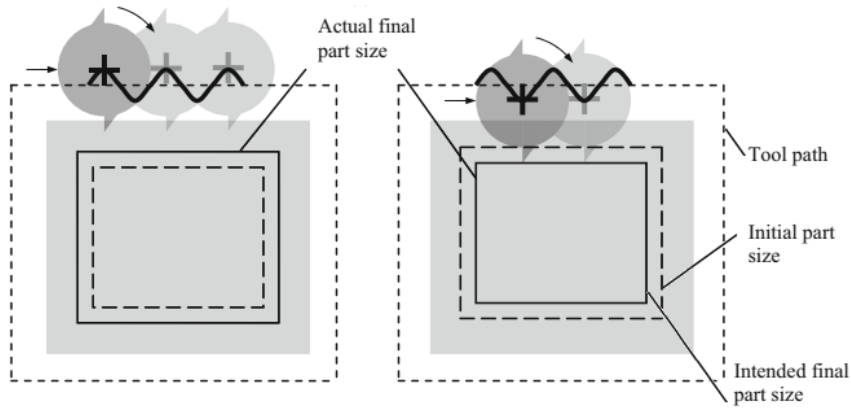
Figure 2.9: Surface location error in milling [50]

2.1.2 Gear cutting process

In this section, the available literature for common gear manufacturing processes namely: gear hobbing, power skiving, and gear shaping is presented. The main objective of this part is to cover the processes of uncut chip extraction and cutting force prediction. It is worth mentioning that there have been numerous studies on the tool wear and tool design, as well as coating condition, in gear-cutting operations that are included briefly in this study. A summary of this research is presented in a review paper [51] by Bouzakis.

2.1.2.1 Gear hobbing

The gear hobbing operation is a long-established gear manufacturing method, for which its invention dates back to the late 19th century. Due to its high productivity and versatility, the process has remained as one of the most prominent gear manufacturing methods. Chip geometry and cutting forces in hobbing have been extensively investigated. Abood [52][53] presented an analytical three-dimensional model to compute the cutting forces in gear hobbing. Using homogeneous matrix transformations, the position of each point located on the hob is represented in a fixed coordinate system on the gear blank. Later, the surface generated by the hob motion in each instant is projected onto the xy plane of the gear

20

and compared with the projected surface generated by the previous cutting tooth. Then, the local chip area for each engaged point on the cutting edge is extracted and, ultimately used to evaluate the cutting forces. The simulation results in [52] demonstrated a close qualitative correlation with measured cutting forces. Due to the complicated kinematics and CWE in hobbing, several researchers have employed exact geometrical modelers to fully capture the uncut chip and machined gear geometry. Dimitriou [54][55] extracted the uncut chip geometry for hobbing in a commercial CAD environment (BREP-based modeler). In this method, the hob and gear geometries are fed into the CAD environment wherein the hob trajectory follows the governing kinematics of the process. Then, by sweeping the hob tooth profile along the trajectory, a 3D surface is generated for each generating position. The uncut chip volume is extracted by removing parts of the workpiece that are located outside of the generated surface. Next, the gear workpiece is updated by performing a Boolean operation between the uncut chip volume and the previously-cut workpiece geometry. Finally, the uncut chip volume is intersected with the cutting plane (i.e., rake plane of the hob) to obtain 2D uncut chip geometry in each revolving position of the hob.

Tapoglou [56] extended the works of Dimitriou to predict the cutting forces from 2D uncut chip geometry in hobbing, and embedded the simulation code in a graphical user interface software called HOB3D [57]. The 2D uncut chip geometry at each revolving position is discretized into smaller elements and discretized cutting forces are calculated using the Kienzle-Victor equation (see Figure 2.10). The predicted cutting forces are compared with measured cutting forces obtained from hobbing of a one-gap gear blank. Although this technique offers high accuracy, the calculations required to keep track of every cut surface become time-consuming as the number of 3D analytical geometry entities increases.

A more efficient approach was proposed by Klocke, who represented the workpiece geometry with a series of parallel planes that intersect with the tool rake face, in order to compute the CWE and process forces in hobbing to investigate tool wear [58], process planning [59], gear quality prediction [60] and online process monitoring [61]. In these works, the uncut chip geometry is calculated in a simulation tool (called SPARTApro [59]). In

21

Revolving Positions

Cutting Direction

Cutting Plane

chip

Chip Cross-section

detail A

A

b

h

equivalent rectangle

Trailing Flank

Y

X

Tooth Coordinate System (1)

Leading Flank

F_{si}
F_{ri}
F_{vi}
F_{si+1}
F_{ri+1}
F_{vi+1}

Elementary Force Components

Kienzle-Victor's eq.

$$F_i = K_i\, b\, h^{(1-z)}$$

m=3.79 mm, d_h=150 mm, a_n=20°, n_i=9, h_a=0°, z_1/z_2=1/56, f_a=4mm/wrev, 16MnCr5BG, v=120m/min Material coefficients: K_s, K_v, K_f

Force Components on Cutting edge system - Generating Position 0

Forces on X axis

80

[daN]

0

0   8   16

Revolving Position

Forces on Y axis

0

[daN]

-160

0   8   16

Revolving Position

Forces on Z axis

160

[daN]

0

0   8   16

Revolving Position

Figure 2.10: CAD-based extraction of uncut chip geometry and discretized force prediction [56]

SPARTApro, the workpiece is represented by a series of equally-distant transverse sections, whereas the tool is described by a spline curve. Then, the uncut chip volume is obtained by calculating the geometrical penetration of the cutter inside the gear. Afterward, for each hob rotation angle, chip thickness is discretized into smaller elements over the un-rolled cutting edge of the hob to determine the discretized cutting forces and the required spindle cutting torque. The simulated and measured spindle torques are compared, and it is observed that there is a good agreement between the mean values while the amplitudes differ.

2.1.2.2 Gear power skiving

Power skiving is a productive and accurate gear-cutting method that has recently received considerable attention in the industry, although it was originally developed in 1910 [62]. Several works have been done on the kinematics and modeling of power skiving. Stadtfeld [63] presented the basic kinematics and chip formation in power skiving. Some other studies extract analytical equations to define a cutting edge at a given tool position to analyze the effect of tool geometry on the rake angle, clearance angle, and depth of cut, which is used in the oblique cutting model [64].

Exact and discrete modelers are also employed for the extraction of CWE in power skiving. Tapoglou [65] calculated the uncut chip geometry in a CAD-based simulation engine called Skiv3D, in a simulation scheme similar to that of [54][55][56] developed for hobbing. Klocke [66] used SPARTApro, which is a CWE simulation engine, to simulate the kinematics of power skiving and extract uncut chip geometry. In [66], the effects of the number of teeth on the cutter, cross-axis, and tilt angle on the maximum chip thickness are demonstrated, and it is observed that there is a correlation between the maximum chip thickness and the maximum tool wear. A few researchers have calculated the cutting forces in the power skiving operation. Spath [67] presented an analytical method for determining the depth of cut, cutting angle, and cutting speed at each workpiece rotation angle over the course of the cutting process. The total cutting force measurements were compared with calculated cutting forces, and the accuracy of the calculations was qualitatively confirmed. Tachikawa [68] derived an analytical equation for predicting cutting forces in power skiving. In Tachikawa's paper, the frequency content of the simulated cutting forces is compared with the power spectrum of the rotating workpiece measured at different speeds to select a free-vibration spindle speed. McCloskey [69][70] extracted the uncut chip geometry from cutter-workpiece engagement calculations using a tri-dexel geometric modeling engine (see Figure 2.11) to be fed into the oblique cutting model to predict the cutting forces.
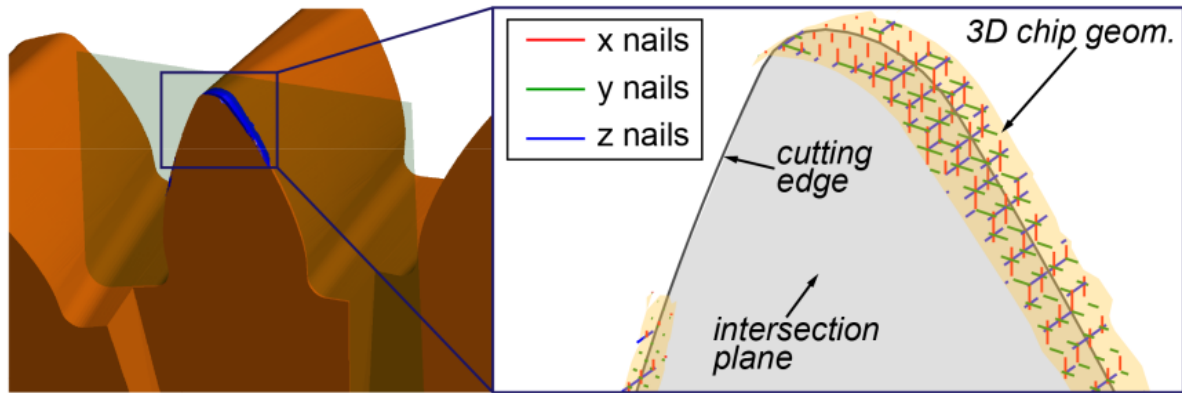
Figure 2.11: Uncut chip representation using 3D dexels in power skiving [69]

2.1.2.3 Gear shaping

Gear shaping is mostly utilized in the manufacturing of internal gears. It can also be applied for the finishing of hardened gears. There have been several studies on cutting tool design in gear shaping. Bouzakis [71] investigated the influence of chip formation and chip flow on the wear mechanism of the gear-shaping process. They realized that the chip thickness distribution varies over the cutting edge of various shapers, resulting in different thermal distributions and wear behavior. They concluded that the width of the shaper's teeth influence the wear mechanisms and need to be considered during tooling design. Datta [72] developed a finite element model to calculate the stress values on the cutting edge of the shaper. By applying different loading conditions, stress distribution on the cutting edge over the width of the gear is determined. They concluded that the tips of the shaper's teeth experience the maximum stress and thus it is crucial to account for its effect in designing the cutter. Tsay [73] presented a two-dimensional mathematical model for a shaper which included protuberance, semi-topping, and the involute curve. Using the meshing equation, the effects of protuberance and semi-topping on the machined gear are illustrated. Until recently, there were few available studies on the cutting force predictions in gear shaping process. Katz [74] used a tri-dexel discrete modeler to extract the uncut chip geometry and cutting forces in gear shaping. The geometries of the cutter and the gear

24

blank are created in a discrete modeler and then imported into the simulation engine. By applying the governing kinematics, the tool is swept between two subsequent time steps and then CWE is calculated. Later, the workpiece is updated accordingly. To obtain the 2D uncut chip geometry, the rake plane of the cutter, halfway from its initial and final position at a time step, is intersected with the CWE data. By applying Delaunay triangulation on the points obtained from intersection calculations and eliminating the irrelevant triangles (using alpha shape reconstruction), the attributed area to each node on the cutting edge is calculated (see Figure 2.12.a). Finally, the corresponding area with each engaged node is fed into the oblique cutting model to calculate the local cutting forces and integrated over the cutting edge to achieve total cutting forces (see Figure 2.12.b). The simulated cutting forces are validated with measured cutting forces obtained from the shaping of an internal spur gear.

Katz [76] extended the model in [74] to include helical gears as well as external gears in the cutting force model and, validated the simulation results with experiments. In [77], Katz added the effect of elastic deformation of the shaper on the final machined gear quality. By measuring the static stiffness of the shaper, in each time step, the shaper's deflection and its effect on the machined gear is determined. Subsequently, the width of the gear is partitioned into cross-sections and deviation of each section with the nominal geometry is calculated. Simulation results are presented based on common error terminologies in standard gear metrology (i.e., profile and lead deviations, and pitch error) and compared with CMM-measured gears. The algorithms and simulations developed by Katz are embedded in a program called ShapePro[78] (see Figure 2.12.c) which is also used in Chapter 6 to virtually measure the hobbed gears.
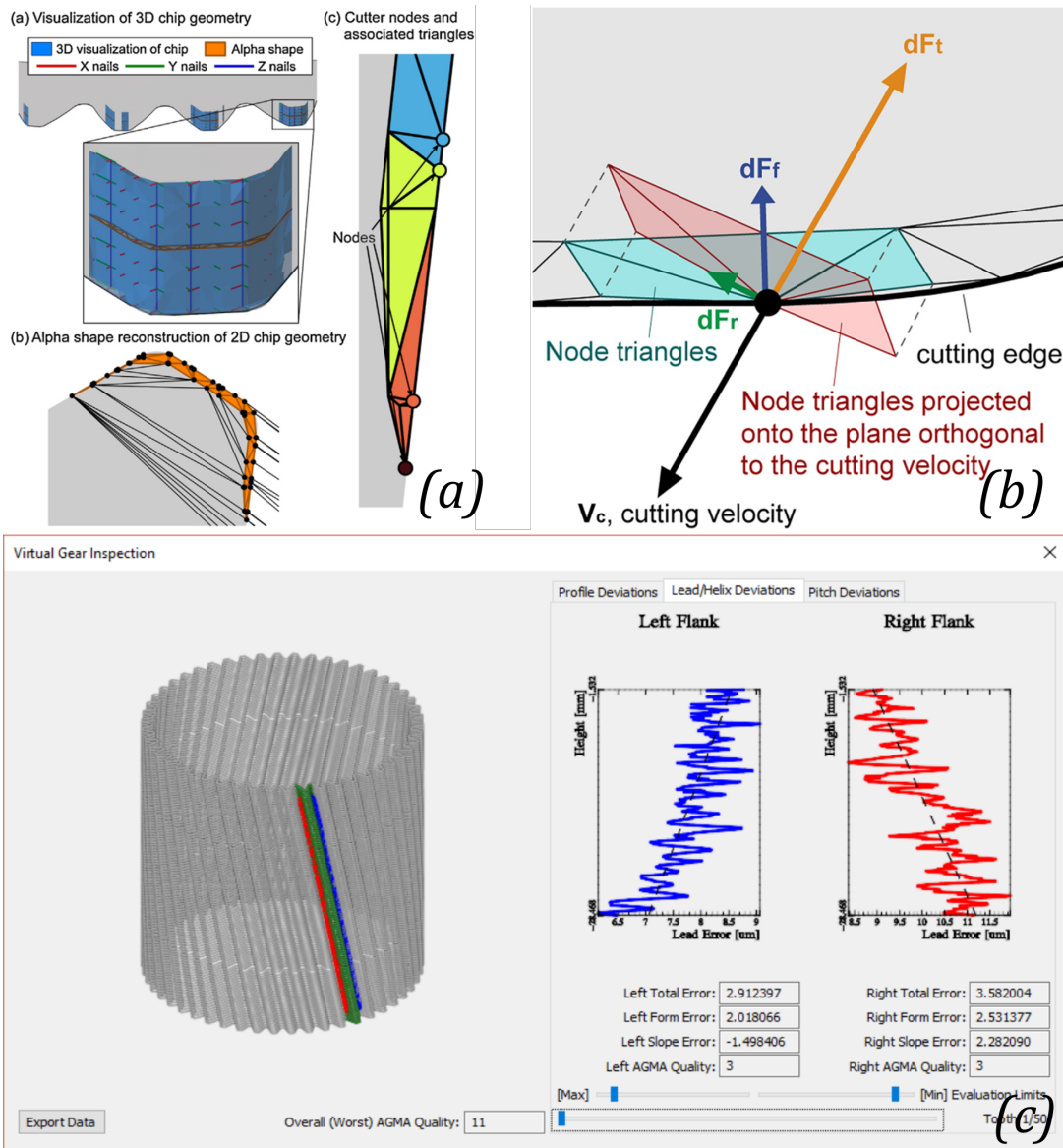
Figure 2.12: (a) Extraction of 2D uncut chip geometry using tri-dexel based modeler [74], (b) local cutting forces [75], (c) virtual metrology module for gear shaping [75]

2.2 Conclusion

As evident from the reviewed literature, the uncut chip geometry, and the cutting forces in gear hobbing have been previously investigated. However, the majority of studies are based on CAD-based exact geometry modeling engines wherein the CWE is extracted accurately by compromising the computational time.

- Previous research has shown that tri-dexel discrete geometric kernel engines strike a balance between computational speed and prediction accuracy in simulating other gear machining operations like shaping [74] and power skiving [70]. Hence, the primary and novel objective of this study is to develop a tri-dexel geometric engine integrated simulation model for the gear hobbing operation. Furthermore, rather than computing only the CWE as in [59], tracking the full progression of the workpiece geometry enables part errors, due to process-induced forces and elastic deformations, to also be simulated and measured in a virtual process planning environment.

Furthermore, to the author's best knowledge, there is no available study on the modeling of elastic deformations, vibrations and their effect on machined gear quality in gear hobbing.

- This thesis introduces an elastic deformation model for hobbing and investigates its effect on machined gears, providing insights into static deformations as a prerequisite for modeling vibrations in hobbing.

Chapter 3

Kinematics of gear hobbing

3.1 Introduction

This chapter presents a general kinematic model for the gear hobbing operation. The kinematics of the process is uniquely complex due to the simultaneous rotation of the cutter and gear, and the multi-axis motion of the components (i.e., axial, radial and in some cases tangential feed motions). Accurate resolution of the kinematic model is achieved by correct description of each axis motion and the relative velocity between the hob and gear. Once the kinematic model is established, it is possible to determine the cutter-workpiece engagement (CWE) data, which can be used to calculate the resulting cutting forces.

In the remainder of this chapter, Sections 3.2-3.3 use common gear terminology to describe the geometry of the gear and the detailed geometry of the hob. Section 3.4 provides a complete description of the kinematic model (e.g., process parameters, coordinate systems, and cutting velocity) followed by the kinematic model validation in Section 3.5.

3.2 Gear geometry

In order to understand the kinematics of hobbing, it is convenient to define some basic terms related to the geometry of gears. These terms are used to describe the gear (workpiece) and hob (cutter) using different notations. The geometry parameters denoted by a subscript 'g' in this thesis refer to the gear, while those with a subscript 'c' refer to the hob.

While there are several non-standard gear geometry which can be machined using a gear hobbing machine, two types of cylindrical gears are considered in this thesis: (1) external spur gears with teeth parallel to the rotation axis and (2) external helical gears with teeth that are oriented along the helical path around the axial axis of the gear. As displayed in Figure 3.1, the normal plane and transverse plane are defined for the gear teeth. The plane that is perpendicular to the helix of the tooth is referred to as the normal plane, whereas the transverse plane is perpendicular to the axial axis of the gear.
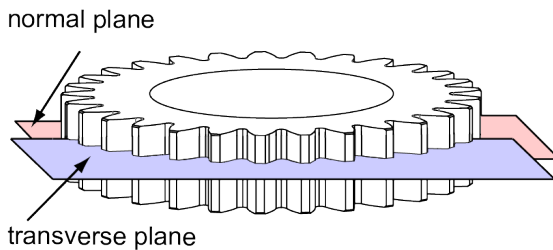
a) spur gear   b) helical gear
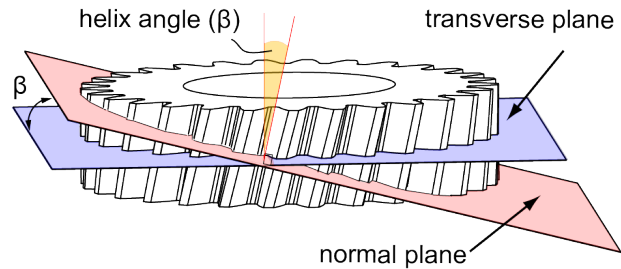
Figure 3.1: Normal and transverse planes in spur (a) and helical (b) gears

In the case of a spur gear, the normal and transverse planes align with each other; however, in a helical gear, the two planes form an angle β with each other. In gear design, it is common to define the geometry of the gear in the normal plane, but it can be helpful to have them defined in the transverse plane when creating the profile of the gear teeth. Figure 3.2 shows the basic geometry of external gears on the transverse plane.

The transverse module is an indication of the size of the gear teeth (measured in the units of length) and is calculated from the normal module (m_{ng}) and helix angle (β) as

[79]:

$$m_{tg} = \frac{m_{ng}}{\cos(\beta)} \tag{3.1}$$

Profile of the gear teeth consists of an involute portion that is usually connected to the tip and root of the gear with fillets. Establishing the pitch and base circles followed by addendum and dedendum circles are the first steps in constructing the tooth profile. The rolling action between the two mating gears (the cutter and gear) occurs on the pitch circle, and its radius is given by [79]:

$$r_{pg} = \frac{N_g m_{tg}}{2} \tag{3.2}$$

The involute section of the tooth begins at the base circle, and its radius is given by [79]:

$$r_{bg} = r_{pg}\cos(\alpha_{tg}) \tag{3.3}$$

The transverse pressure angle of the gear is denoted by α_{tg}, which is determined as the angle that is tangent to the gear teeth's profile at the pitch radius. The transverse pressure angle is calculated by using the normal pressure angle according to the following equation:

$$\alpha_{tg} = \tan^{-1}\left(\frac{\tan(\alpha_{ng})}{\cos(\beta)}\right) \tag{3.4}$$

The tooth profile begins at the dedendum circle (the root of the gear), and its radius is:

$$r_{dg} = r_{pg} - h_{dg} \tag{3.5}$$

The involute section of the tooth ends at the addendum circle and its radius is given by:

$$r_{ag} = r_{pg} + h_{ag} \tag{3.6}$$

Above, the addendum of a gear (h_{ag}) is the difference between the addendum radius of the gear and the pitch circle radius which for a standard tooth profile is defined as: $h_{ag} = m_{tg}$ [80]. The dedendum of the gear (h_{dg}) is the difference between the pitch circle

30
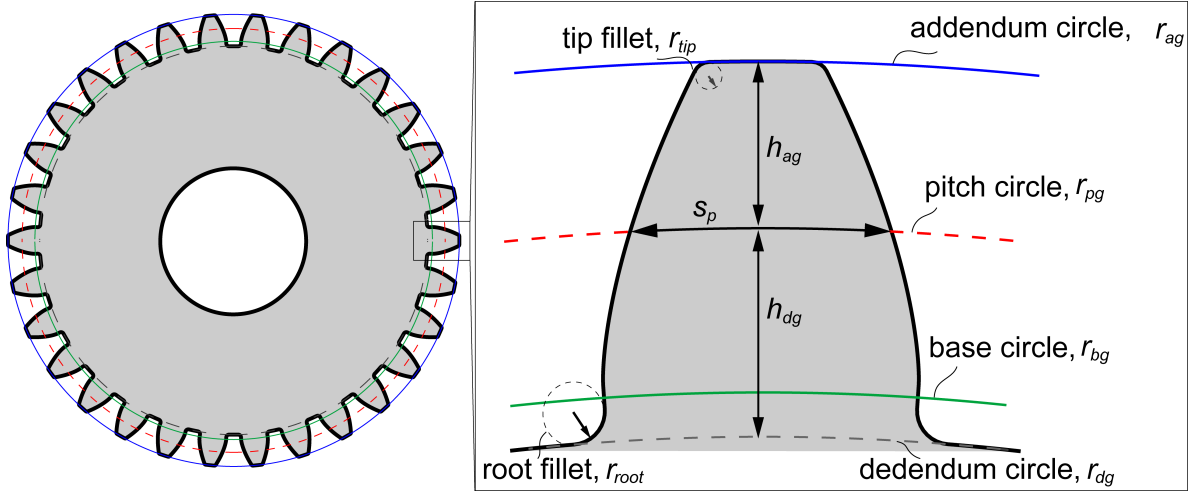
Figure 3.2: Basic gear tooth geometry definitions

radius and the dedendum circle radius of the gear. For a standard gear $h_{dg} = 1.25 m_{tg}$ [80]. In practice, however, these standard values can be modified as required by manufacturers to create non-standard gear geometries. As the necessary circles and parameters are defined, the involute section of the tooth is constructed by calculating tooth thickness (s_r) at every arbitrary radius $r_{bg} < r < r_{ag}$ [79]:

$$s_r = r \left[\frac{s_p}{r_{pg}} + 2 \left(\text{inv}(\alpha_{tg}) - \text{inv}(\cos^{-1}\left(\frac{r_{bg}}{r}\right)) \right) \right] \tag{3.7}$$

Tooth thickness (s_r) for a standard involute gear measures the length of an arc that connects the two involute profiles that form one gear tooth. Above, the involute function, inv(.), is the basis for the involute profile of the gear and is defined as [79]:

$$\text{inv}(\alpha_{tg}) = \tan(\alpha_{tg}) - \alpha_{tg} \tag{3.8}$$

Additionally, s_p is the transverse circular tooth thickness at the pitch circle and is expressed as:

$$s_p = m_{tg} \frac{\pi}{2} + 2 x m_{tg} \tan(\alpha_{tg}) \tag{3.9}$$

31

above x is the transverse profile modification factor which is zero for standard gear geometries. However, in practice, cutters undergo several regrinding and resharpening which results in producing gears that are profile-shifted [81]. Finally, the root and the tip of the gear are usually connected to the flanks using fillets given by r_{root} and r_{tip}, respectively.

3.3   Hob and workpiece geometry

A hob is a cylindrical-shaped cutter having its cutting teeth following the helical path of a worm gear. Over the length of the hob, several gashes are made for easier chip evacuation. Alternatively, a hob can be perceived as a series of equally-spaced racks mounted on the outer diameter of a cylinder where each rack is axially shifted from the previous rack by axial lead (l_c) over the number of flutes (gashes). The axial lead of the hob is given by:

$$l_c = \frac{\pi m_{nc} N_c}{\cos(\eta)} \tag{3.10}$$

where η, the lead angle of the hob, is defined as the angle between the helix thread and a line perpendicular to the hob's axial axis, and is expressed as follows:

$$\eta = \sin^{-1}\left(\frac{m_{nc} N_c}{2 r_{pc}}\right) \tag{3.11}$$

In equations 3.10 and 3.11, m_{nc} and N_c are the normal module and the number of starts on the hob, respectively. The number of starts is the simultaneous helical threads around the hob. For each revolution of a single-start hob, the workpiece advances by one gear gap. If a hob has two starts, then the workpiece must advance by two gear gaps for each revolution of the cutter. Even though multi-start hobs offer higher productivity, single-start hobs are widely used in industry due to their accuracy [82]. Additionally, the axial pitch of the hob (p_c) is the axial distance between the tips (or any two similar points on the teeth profiles) of two adjacent teeth on the rack. The main geometrical parameters of the hob are shown in Figure 3.3.
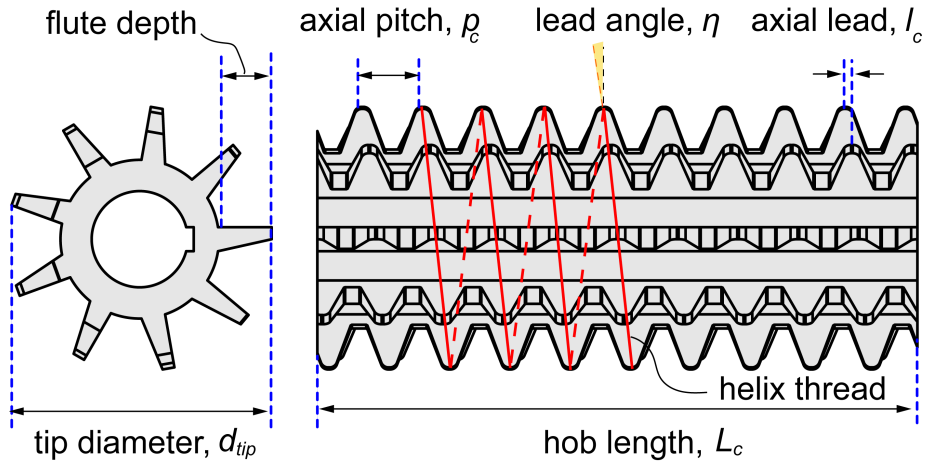
Figure 3.3: Basic hob geometry

To manufacture an exact involute profile on the gear, the standard profile geometry of the hob must be used. When the hob has axial gashes (which is typical of single and two-start hobs), its actual profile will resemble the axial section of an involute helicoid worm, as described [83]. However, since the profile of most gear hobs is very similar to that of a standard basic rack, a simplified straight-sided profile will be used instead. Additionally, few modifications such as protuberance and semi-topping are required on the rack profile when a special gear profile is targeted [84]. The basic profile of a rack is demonstrated in Figure 3.4. Half of the profile is generated and then mirrored about the $Z_{c,\text{tooth}}$ axis to form the complete rack profile. The rack profile is divided into 5 regions (from AB to EF) and in every region, the coordinate of each point on the hob is calculated. AB is a line parallel to the axial axis of the hob which cuts the root of the produced gear. The fillet section BC with radius $\rho = 0.38m_{nc}$ [80] is tangent to sections AB and CD. Region CD is a straight line that is involved in forming the flank of the gear during the generating process. The root chamfer (region DE) is angled by α_c (usually 45°) and its height (c_h) and width (c_w) are less than 10% of the gear module [52]. EF region is parallel to the axial axis of the hob and does not contribute to the cutting process. Prior to determining the coordinates of each point on the rack profile, it is necessary to introduce several parameters. For a basic rack profile [80], the addendum ($h_{ac} = 1.25m_{nc}$) and dedendum ($h_{dc} = m_{nc}$) are used

33
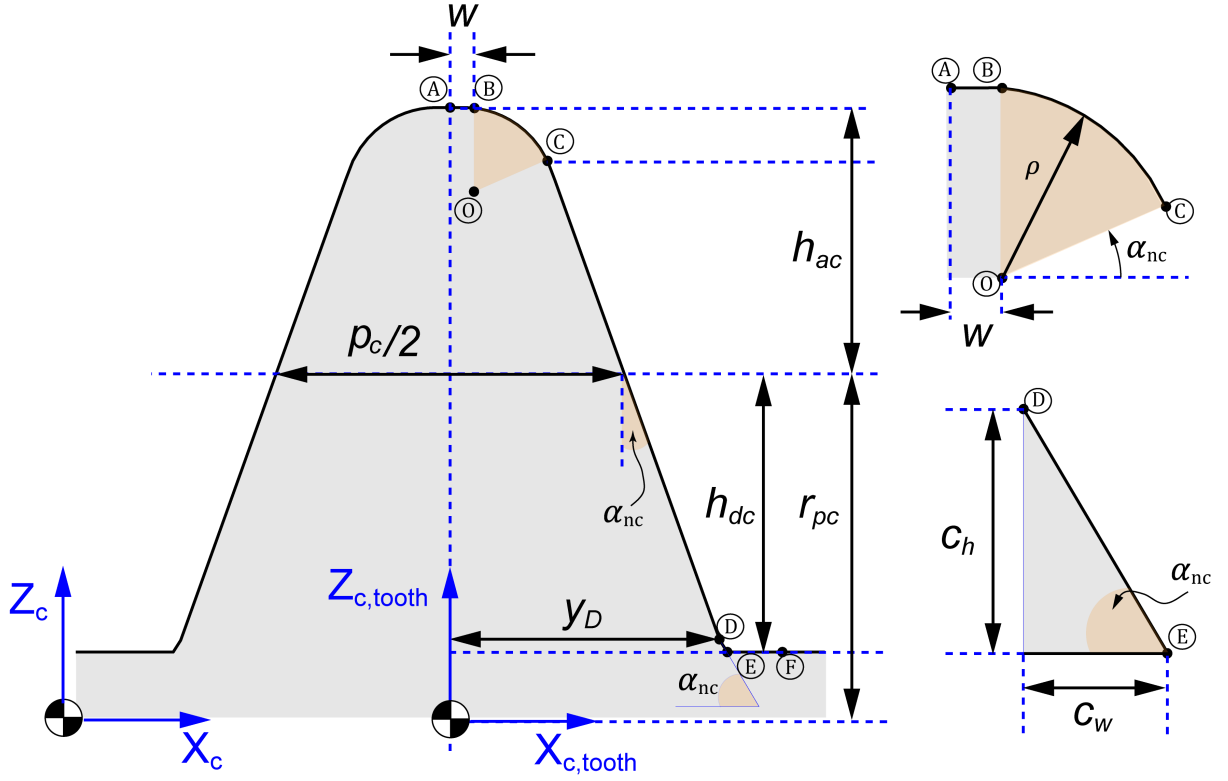
Figure 3.4: Basic rack profile used in generating the hob geometry

to define the pitch radius of the hob ($r_{pc} = r_{ac} - h_{ac}$), wherein r_{ac} is the addendum circle radius (also the radius of the tip of the hob) which is usually provided along with the module of the hob in the cutter's geometrical specification. In addition, the thickness of each tooth at the pitch radius is half of the axial pitch ($p_c = \pi m_{nt}$). In the following table, an equation for each region on the hob profile is presented.

In the equations above, w and x_D are defined as follows:

$$w = \frac{\pi m_n}{4} - \left(h_{ac} - \rho\big(1 - \sin(\alpha_{nc})\big)\right)\tan(\alpha_{nc}) - \rho\cos(\alpha_{nc}) \tag{3.12}$$

$$x_D = \frac{\pi m_n}{4} - (h_{dc} - c_h)\tan(\alpha_{nc}) \tag{3.13}$$

In selecting a hob, it should be noted that the hob must have a similar normal module

Table 3.1: Coordinates of points on the basic rack profile (adopted from [52])

Region	X Coordinate	Z Coordinate
AB	$0 \le x \le w$	$z = r_{pc} + h_{ac}$
BC	$w \le x \le w + \rho\cos(\alpha_{nc})$	$z = r_{pc} + h_{ac} - \rho + \sqrt{\rho^2 - (x-w)^2}$
CD	$w + \rho\cos(\alpha_{nc}) \le x \le x_D$	$z = r_{pc} - \dfrac{4x - \pi m_n}{4\tan(\alpha_{nc})}$
DE	$x_D \le x \le x_D + c_w$	$z = r_{pc} - \dfrac{h_{dc} - c_h}{\tan(\alpha_{nc})} - (x-_D)\tan(\alpha_{nc})$
EF	$x_D + c_w \le x \le \dfrac{\pi m_n}{2}$	$z = r_{pc} + h_{dc}$

(m_{nc}) and normal pressure angle (α_{nc}) with those of the manufactured gear. Usually, in hobbing, the workpiece geometry is a cylinder with a bore, and its outer diameter must have the tip diameter (addendum diameter) of the desired manufactured gear. The bore diameter is decided based on the clamping setup and/or customer requirements.

3.4 Kinematics of hobbing

Three main coordinate systems, namely, the Tool Coordinate System (TCS), Workpiece Coordinate System (WCS), and Machine Coordinate System (MCS), in addition to an Auxillary Coordinate System (ACS) are introduced to determine the gear hobbing kinematics (see Figure 3.5). TCS is fixed on the hob head and its origin is located on the hob's axial axis. Similar to TCS, WCS is fixed to the center of the top face of the gear blank and rotates with the worktable. MCS is stationary and shares a common origin and z axis with the WCS. ACS coincident with the yz-plane of the MCS and is located at the midpoint of the hob.
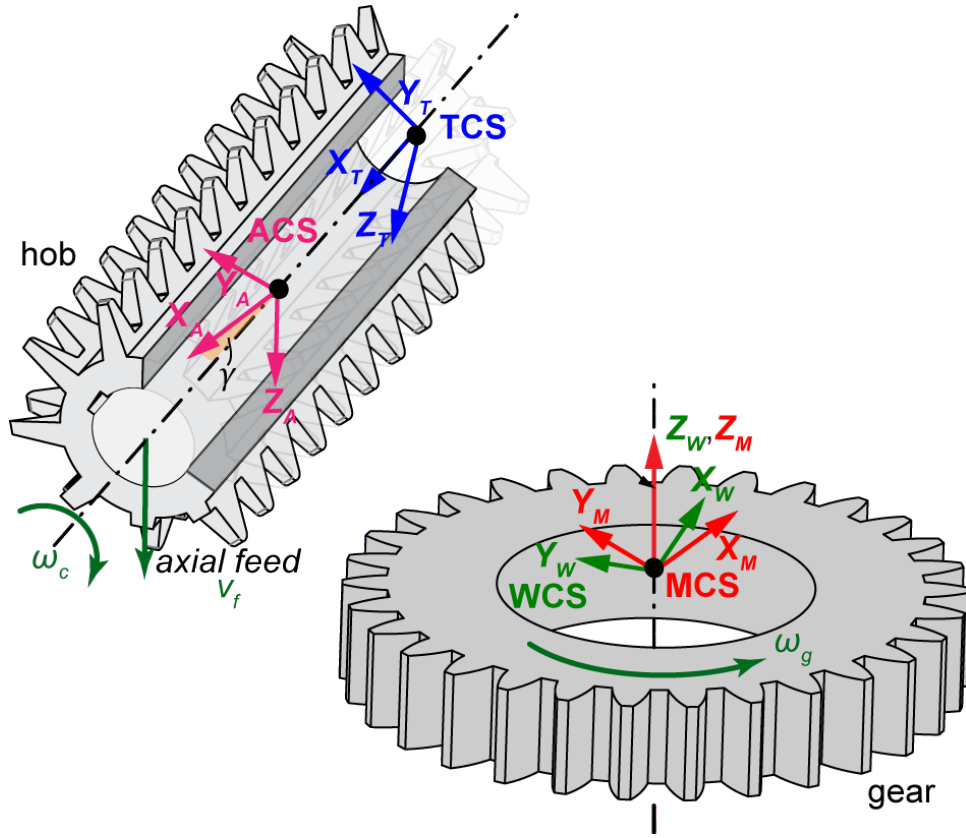
Figure 3.5: Coordinate systems in the kinematics model

3.4.1 Process parameters

The hob and gear rotate synchronously about their axes with angular velocities ω_c and ω_g, respectively. The hob is fed along the gear width with axial feed velocity (v_f).

The hob is positioned to cut a specific radial depth into the workpiece (d_c), which is referred to as the depth of cut. Usually, the cutting takes place in a one-pass process and, the hob depth of cut is set to $d_c = 2.25 m_{nc}$ such that the final nominal center-to-center distance is achieved. In practical applications, however, d_c is often modified to rectify tooth thickness errors or apply profile modifications in the finished gear. For gears that will not undergo any additional finishing operations (such as grinding), multiple roughing

and finishing passes are often utilized to enhance the surface and finish quality wherein each pass has a specific depth of cut. Thus, it is convenient to introduce a reference position for the hob (i.e., scrape distance) and calculate the radial position for each pass (i) as follows:

$$r_{\text{end},i} = r_{\text{scrape}} - \sum_{n=1}^{i} d_{c,i} \tag{3.14}$$

where the scrape distance (r_{scrape}) is the radial distance at which the outer diameter of the hob touches the outer diameter of the gear such that no cutting action occurs, and is defined as:

$$r_{\text{scrape}} = r_{ag} + r_{ac} \tag{3.15}$$

Conventional (i.e., $v_f < 0$) and climb (i.e., $v_f > 0$) are the two strategies to axially feed the hob [54] through the workpiece. Although less common, the simultaneous axial and tangential feeding approach can be applied especially in manufacturing large and wide gears having coarse pitches [82]. In this thesis, however, the simultaneous feeding strategies were not considered.

In a single-pass process, the hob starts at a clearance distance from the top of the gear (i.e., approach length) and axially moves along the gear width (w_g) at the axial feed rate in the z axis of the WCS until it exceeds the bottom of the gear by a specific clearance distance (i.e., overrun length) as shown in Figure 3.6. The approach length is the distance from the initial contact of the hob with the gear to the point where the hob reaches the full depth of cut and is given by [84]:

$$A = \sqrt{d_c \left(\frac{2(r_{ac} + r_{ag}) - d_c}{\cos^2(\beta)} - 2r_{ag} \right)} \tag{3.16}$$

The axial distance from the bottom of the gear to the point where the profiles of the gear teeth are completely cut is the overrun length and is expressed as follows [84]:

$$O = \frac{h_{ag} \cos(\beta) \tan(\gamma)}{\tan(\alpha_{ng})} \tag{3.17}$$

37

The total axial travel length is calculated as:

$$S = A + w_g + O \tag{3.18}$$
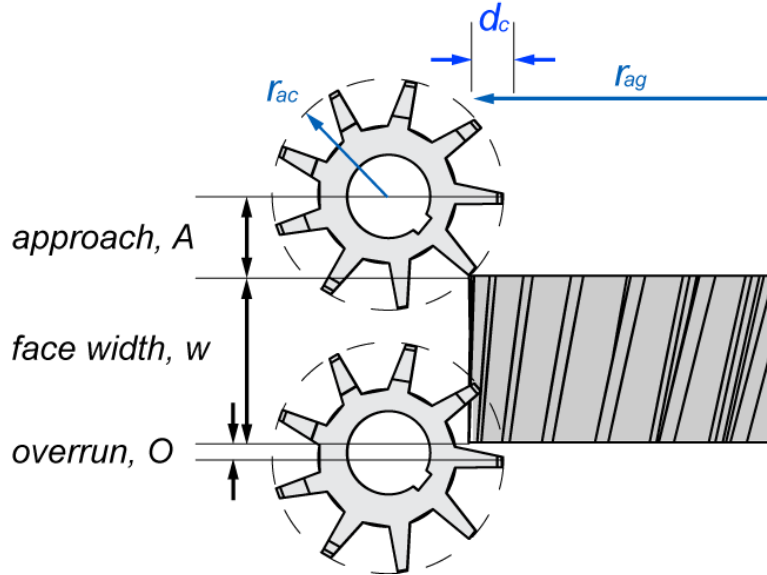
Figure 3.6: Approach and overrun lengths (adopted from [84])

A radial infeed followed by an axial feed motion is also common in multi-pass processes. The first pass is similar to a single-pass process (i.e., $S = A + w_g + O$). However, in the subsequent passes, instead of axially approaching the gear blank, the hob is radially fed (usually at a constant rate) into the gear blank until it approaches its desired radial position, and then axially travels along the gear width followed by the overrun length (i.e., $S = w_g + O$).

The hob swivel angle (γ) is another process parameter that is typically adjustable on gear cutting machines, which is defined as an angle by which the hob axis is tilted to mesh the hob teeth with those of the gear being machined (see Figure 3.5). The hob swivel angle is calculated based on the handedness of the hob and gear, as well as the gear helix angle:

$$\gamma = \beta \pm \eta \tag{3.19}$$

In the equation above, $(-)$ is used for a hob and gear of the same handedness while $(+)$ is used otherwise.

In planning a hobbing process, the angular speed of the hob (ω_c) is calculated based on the nominal cutting velocity (V_c) in (m/min) as follows:

$$\omega_c = \frac{V_c}{2\pi r_{ac}} \times \frac{2\pi}{60} \tag{3.20}$$

The workpiece rotational speed (ω_g), however, is calculated based on the hob rotational speed. In spur gears, it is based on the ratio of the number of the gear teeth (N_g) to the number of hob's starts (N_c). The following equation satisfies the meshing condition by equating the linear velocities at the contact point on the pitch circle.

$$\omega_g = \left(\frac{N_c}{N_g}\right) \cdot \omega_c \tag{3.21}$$

In helical gears, an additional rotational term $d\theta_g$ is added to compensate for the axial motion of the hob relative to the helix of the gear (see Figure 3.7). The helix must make $d\theta_g$ within a distance equivalent to dz. If the axial feed rate in (mm/WR) is denoted as v_f, an additional rotational speed of $d\theta_g/dt$ is required:

$$\frac{d\theta_g}{dt} = \frac{\sin(\beta)v_f}{\pi N_g m_n} \cdot \omega_g \tag{3.22}$$

This will satisfy the necessary meshing condition.

$$\omega_g = \left(\frac{N_c}{N_g}\right) \cdot \left(1 - \sigma \frac{|v_f \sin(\beta)|}{\pi N_g m_n}\right)^{-1} \omega_c \tag{3.23}$$

where $\sigma = \mathrm{sgn}(\beta) \cdot \mathrm{sgn}(\eta) \cdot \mathrm{sgn}(\nu_f)$ provides sign correction.

3.4.2 Coordinate system transformation

It is practical to describe the geometric and kinematic parameters, such as velocities, axis motion, and chip geometry, along with the resulting process parameters, such as
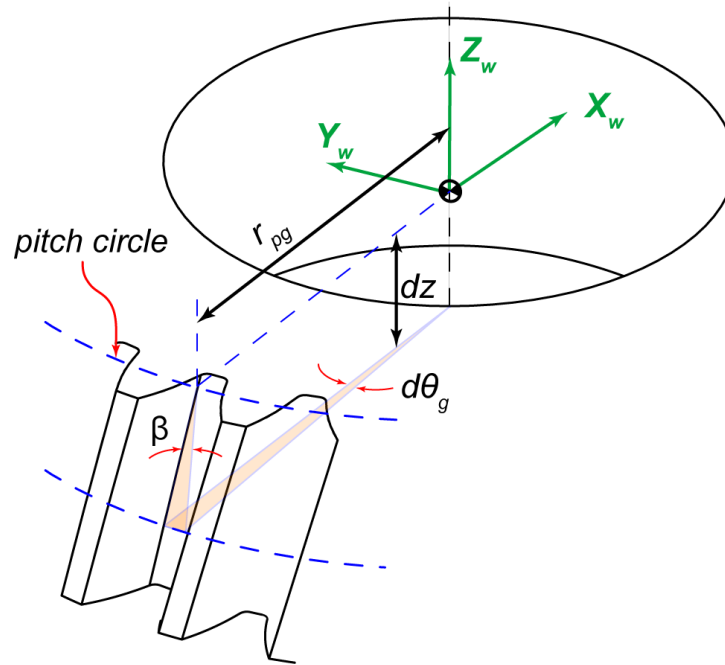
Figure 3.7: Additional rotation of the helical gear to ensure a proper meshing condition

cutting forces, cutting torques, and deflections, using any of the defined coordinate systems. For instance, the multi-dexel geometric engine (ModuleWorks) requires the cutter and workpiece geometries to be represented in the WCS. Additionally, the experimental forces are typically measured according to the rotating WCS.

Figure 3.8 displays the hob and the gear at a specific time step with the defined coordinate systems. With the knowledge of the homogeneous transformation matrix between two coordinate systems, it is feasible to determine the coordinates of a given point in one system by computing its coordinates in the other system. For example, a point along a cutting edge of the hob can be expressed in the TCS with vector $\boldsymbol{r}_c(t)$. The same point can also be represented in the WCS as $\boldsymbol{r}_w(t)$. The homogeneous transformations linking $\boldsymbol{r}_c(t)$ and $\boldsymbol{r}_w(t)$ is expressed as:

$$\boldsymbol{r}_w(t) = [\boldsymbol{H}_{TCS}^{WCS}]\boldsymbol{r}_c(t) = [\boldsymbol{H}_{TCS}^{WCS}]_{4\times 4} \begin{bmatrix} x_c(t) \\ y_c(t) \\ z_c(t) \\ 1 \end{bmatrix}_{4\times 1} = \begin{bmatrix} x_w(t) \\ y_w(t) \\ z_w(t) \\ 1 \end{bmatrix}_{4\times 1} \tag{3.24}$$
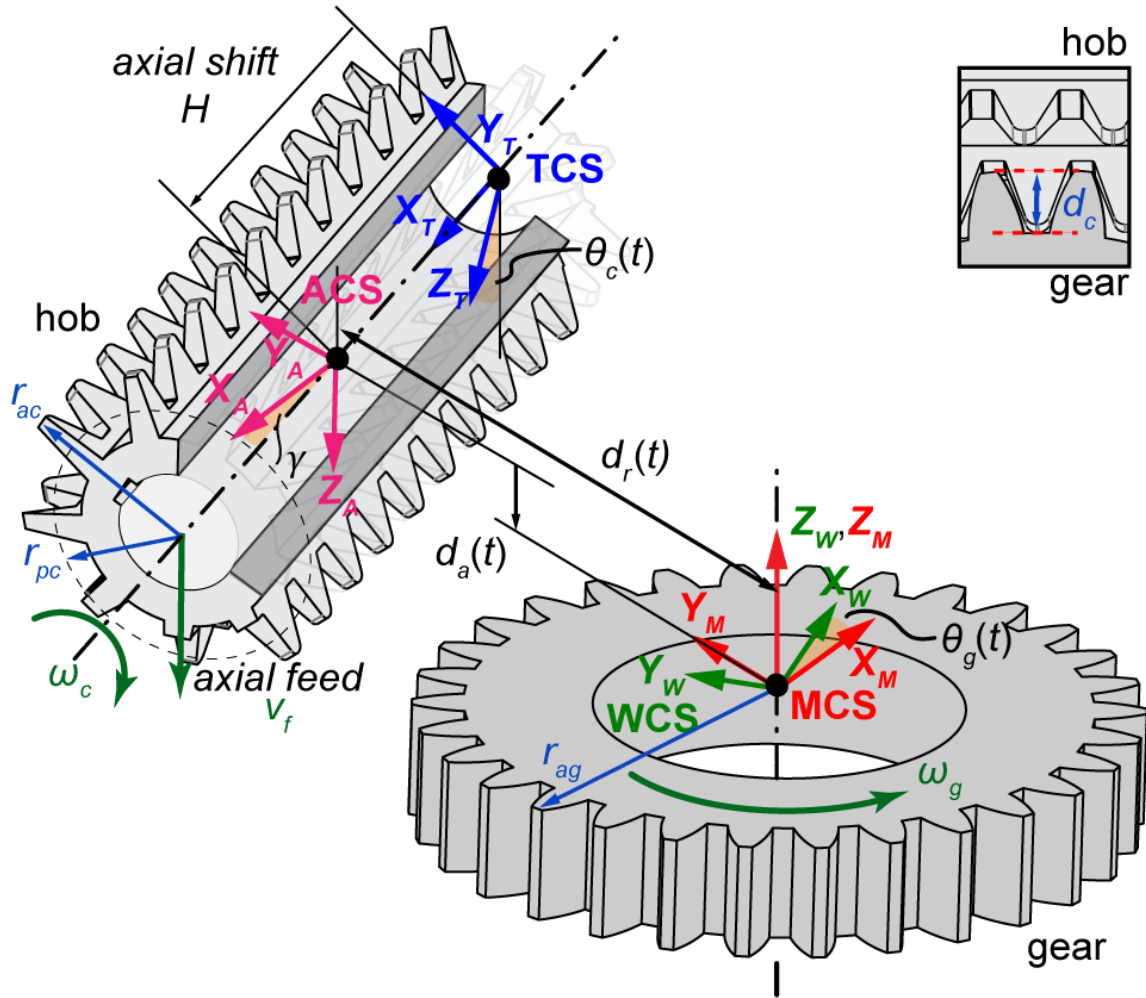
Figure 3.8: Principal kinematics and coordinate systems in hobbing

To determine $[\boldsymbol{H}_{TCS}^{WCS}]$, first, the transformation from the WCS to MCS is established. $\boldsymbol{R}_{z,\theta_g(t)}$ considers the rotation of the gear (and WCS) about the stationary z axis of MCS

41

by $\theta_g(t)$:

$$\boldsymbol{R}_{z,\theta_g(t)} = \begin{bmatrix} \cos\left(\theta_g(t)\right) & -\sin\left(\theta_g(t)\right) & 0 & 0 \\ \sin\left(\theta_g(t)\right) & \cos\left(\theta_g(t)\right) & 0 & 0 \\ 0 & 0 & 1 & 0 \\ 0 & 0 & 0 & 1 \end{bmatrix} \tag{3.25}$$

The angular position of the gear is expressed with $\theta_g(t)$ as a function of time which linearly increases at the rotational velocity of the gear (ω_g):

$$\theta_g(t) = \omega_g t \tag{3.26}$$

As MCS and WCS share a common origin, $\boldsymbol{R}_{z,\theta_g(t)}$ encompasses the total transformation matrix between the WCS and MCS, thus:

$$[\boldsymbol{H}_{WCS}^{MCS}] = \boldsymbol{R}_{z,\theta_g(t)} \tag{3.27}$$

Establishing $[\boldsymbol{H}_{TCS}^{MCS}]$, however, is more complex and requires multiple translations and rotation matrices. The center-to-center radial distance between the hob and gear (i.e., r_{end}) is established with the translation $\boldsymbol{T}_{y,d_r(t)}$ along the y axis of the ACS by $d_r(t)$:

$$\boldsymbol{T}_{y,d_r(t)} = \begin{bmatrix} 1 & 0 & 0 & 0 \\ 0 & 1 & 0 & d_r(t) \\ 0 & 0 & 1 & 0 \\ 0 & 0 & 0 & 1 \end{bmatrix} \tag{3.28}$$

When no radial infeed is planned, $d_r(t) = d_r = r_{scrape} - \sum_{n=1}^{i} d_{c,i}$. However, when i^{th} pass undergoes a radial infeed motion, $d_r(t)$ is calculated as:

$$d_r(t) = r_{\text{scrape}} - \sum_{n=1}^{i-1} d_{c,i} - \int_{t_i}^{t_i+t_f} v_r \, dt \tag{3.29}$$

Above, t_f is the time required for the tool to accomplish the desired radial end position (r_{end}) at the constant infeed rate (v_r) and is given:

$$t_f = \frac{r_{\text{scrape}} - \sum_{n=1}^{i} d_{c,i}}{v_r} \tag{3.30}$$

42

The total process time until i^{th} pass is given by t_i. When the radial infeed motion completes, the cutter is radially positioned at $r_{\text{end}} = r_{\text{scrape}} - \sum_{n=1}^{i} d_{c,i}$.

The hob's axial feed motion $d_a(t)$ along the z axis of the ACS is captured with the translation $\boldsymbol{T}_{z,-d_a(t)}$:

$$
\boldsymbol{T}_{z,-d_a(t)} = \begin{bmatrix} 1 & 0 & 0 & 0 \\ 0 & 1 & 0 & 0 \\ 0 & 0 & 1 & -d_a(t) \\ 0 & 0 & 0 & 1 \end{bmatrix} \tag{3.31}
$$

$d_a(t)$ for pass i is calculated based on the axial feed rate, total axial travel distance, and CNC machine's offset value (D_o) as follows:

$$
d_a(t) = D_o - \int_{t_i}^{t_i+t_a} v_f \, dt \tag{3.32}
$$

In the equation above, t_a is the required time to travel the total axial travel length (S) and is given:

$$
t_a = \frac{S}{v_f} \tag{3.33}
$$

$\boldsymbol{R}_{y,\gamma}$ captures the swivel angle for the hob by γ about the y axis of the ACS.

$$
\boldsymbol{R}_{y,\gamma} = \begin{bmatrix} \cos(\gamma) & 0 & -\sin(\gamma) & 0 \\ 0 & 1 & 0 & 0 \\ \sin(\gamma) & 0 & \cos(\gamma) & 0 \\ 0 & 0 & 0 & 1 \end{bmatrix} \tag{3.34}
$$

$\boldsymbol{T}_{x,-H}$ represents the hob's translation along its x axis by the axial shift H. Axial shifting is a common way to distribute wear on the hob uniformly [51].

$$
\boldsymbol{T}_{x,-H} = \begin{bmatrix} 1 & 0 & 0 & -H \\ 0 & 1 & 0 & 0 \\ 0 & 0 & 1 & 0 \\ 0 & 0 & 0 & 1 \end{bmatrix} \tag{3.35}
$$

Finally, the rotation of the tool about its x axis is described by $\boldsymbol{R}_{x,\theta_c(t)}$:

$$\boldsymbol{R}_{x,\theta_c(t)} = \begin{bmatrix} 1 & 0 & 0 & 0 \\ 0 & \cos\left(\theta_c(t)\right) & \sin\left(\theta_c(t)\right) & 0 \\ 0 & -\sin\left(\theta_c(t)\right) & \cos\left(\theta_c(t)\right) & 0 \\ 0 & 0 & 0 & 1 \end{bmatrix} \tag{3.36}$$

The angular position of the hob is a function of time and linearly increases at the hob's angular velocity (ω_c):

$$\theta_c(t) = \omega_c t \tag{3.37}$$

Thus, the transformation matrix from the TCS to the MCS is determined as:

$$[\boldsymbol{H}_{TCS}^{MCS}] = \boldsymbol{T}_{y,d_r(t)}\boldsymbol{T}_{z,-d_a(t)}\boldsymbol{R}_{y,\gamma}\boldsymbol{T}_{x,-H}\boldsymbol{R}_{x,\theta_c(t)} \tag{3.38}$$

The final transformation from the TCS to the WCS can be derived by:

$$[\boldsymbol{H}_{TCS}^{WCS}] = [\boldsymbol{H}_{MCS}^{WCS}][\boldsymbol{H}_{TCS}^{MCS}] = [\boldsymbol{H}_{WCS}^{MCS}]^{-1}[\boldsymbol{H}_{TCS}^{MCS}] =$$
$$\boldsymbol{R}_{z,-\theta_g(t)}\boldsymbol{T}_{y,d_r(t)}\boldsymbol{T}_{z,-d_a(t)}\boldsymbol{R}_{y,\gamma}\boldsymbol{T}_{x,-H}\boldsymbol{R}_{x,\theta_c(t)} \tag{3.39}$$

3.4.3   Relative cutting velocity

The cutting velocity in hobbing refers to the speed at which the hobbing tool moves along the gear teeth. This velocity is typically expressed in units of meters per minute (m/min). In hobbing, an estimated cutting velocity (i.e., nominal cutting velocity) is selected based on several factors, including the type of workpiece material being machined, cooling conditions, and cutting tool coating. The nominal cutting velocity is assumed to be purely due to the hob's rotation and is constant throughout the process. However, the actual cutting velocity (i.e., the relative velocity between the cutter and workpiece) is changing along the cutting edge and over time due to the continuous rotation of the hob and gear. The calculation of the relative velocity is required for determining the cutting forces and their directions. Thus, a precise calculation is necessary.

In the WCS, the tool appears to move in a circular path around the workpiece, with the axis of the path being the center axis of the workpiece. This revolving motion along with the rotation and the axial motions of the hob are the components of the cutting velocity (see Figure 3.9) calculated as:

$$\boldsymbol{V_c} = \boldsymbol{\omega_c} \times \boldsymbol{r_{p_i,c}} - \boldsymbol{\omega_g} \times \boldsymbol{r_{p_i,g}} + \boldsymbol{v_f} \tag{3.40}$$

Above, $\boldsymbol{V_c}$ is the cutting velocity at point p_i, which also represents the orientation of the workpiece material flow on the cutting edge. $\boldsymbol{\omega_c}$ and $\boldsymbol{\omega_g}$ are the rotational velocity vectors for the cutter and gear, respectively. $\boldsymbol{r_{p_i,c}}$ and $\boldsymbol{r_{p_i,g}}$ define vectors of the point p_i from the hob and gear axes of rotation, respectively. $\boldsymbol{v_f}$ is the vector representation of the axial feed velocity and '$\times$' designates the vector product.
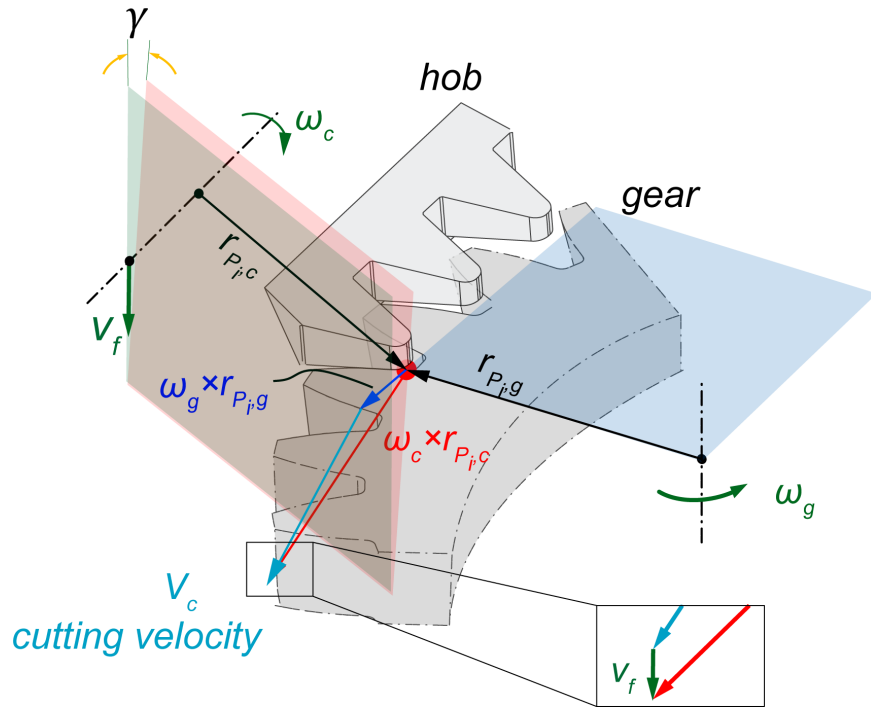
Figure 3.9: Cutting velocity calculation

45

3.5 Validation of the kinematic model

The feed axes for a Liebherr LC 500 hobbing machine [85], used in this study, are shown in Figure 3.10. The kinematic model was validated by collecting position trajectories using the machine's CNC (Siemens 840D) during one-pass and two-pass hobbing trials. The process parameters for the trials are listed in Tables 3.4 and 3.5, respectively.
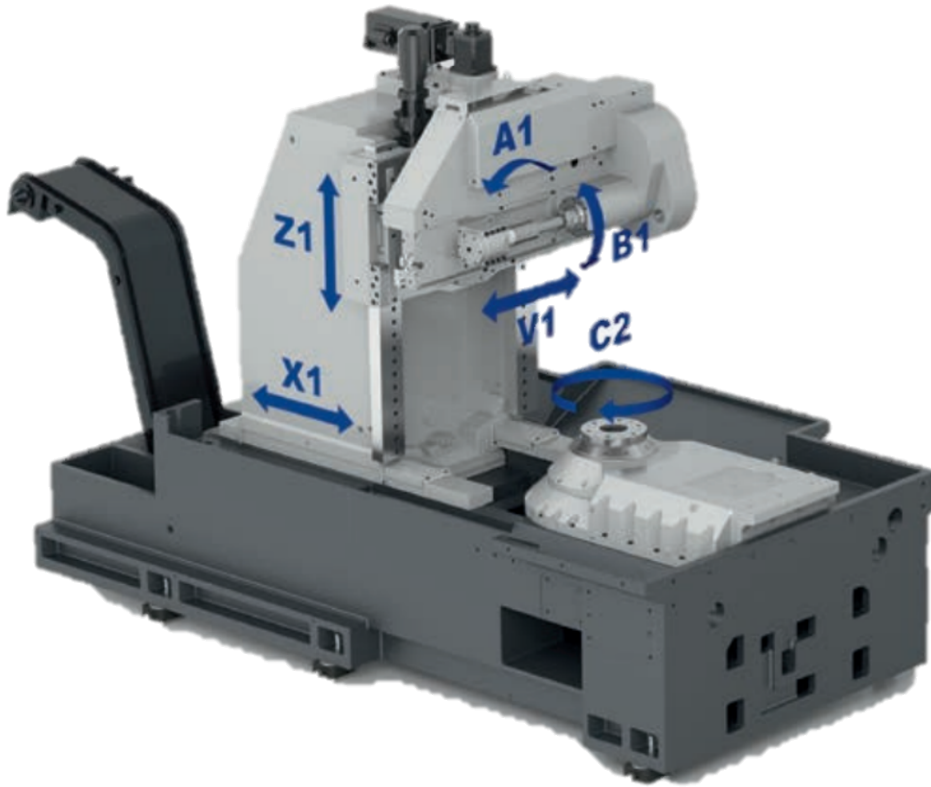
Figure 3.10: Liebherr LC 500 servo axis representation (from [85])

For the exemplary process parameters in Table 3.2, 3.3 and 3.4, the measured and model-predicted movements for the $B1$, $C2$, $X1$, and $Z1$ axes (which accomplish θ_c, θ_g, d_r, and d_a) are shown in Figures 3.11 and 3.12. Although $B1$ and $C2$ undergo monotonously increasing (or decreasing) angular motion, the CNC registers their position into $0°$ ... $360°$ and $-180°$ ... $+180°$ intervals. The simulated profiles are shifted in time as well as

46

Table 3.2: Workpiece geometry data

Parameters	Value
Normal module m_{ng} [mm]	3.175
Number of teeth	30
Addendum diameter d_{ag} [mm]	102.25
Helix angle β [^{o}]	0.0
Pressure angle α_{ng} [^{o}]	20.0
Gear width w_g [mm]	56.6
Material	AISI 4320

Table 3.3: Tool geometry data

Parameters	Value
Normal module m_{nc} [mm]	3.175
Number of starts N_c	1
Number of flutes (gashes)	14
Addendum diameter d_{ac} [mm]	38.1
Pressure angle α_{nc} [^{o}]	20.0
Length L_c [mm]	102.0
Material	ASP 2052

Table 3.4: Cutting process data (one-pass process)

Parameters	Value
Axial feed rate v_f [mm/WR]	3.0
Depth of cut d_c [mm]	7.143
Cutting speed V_c [m/min]	55.0
Axial feed strategy	Conventional
Radial infeed strategy	None

Table 3.5: Cutting process data (two-pass process)

Parameters	Pass one value	Pass two value
Axial feed rate v_f [mm/WR]	3.0	0.75
Depth of cut d_c [mm]	6.743	0.4
Cutting speed V_c [m/min]	55.0	55.0
Axial feed strategy	Conventional	Conventional
Radial feed rate v_r [mm/WR]	0	0.4

in the vertical axes in order to match the initial positions of the collected CNC signals (which depends on the CNC machine's offset values). Figure 3.12 displays the measured and simulated feed axes motion for a two-pass hobbing process involving roughing and finishing passes. Once the roughing pass finishes, the tool radially retracts back and then axially moves upward until it reaches the top of the gear. While keeping the same axial position, the tool is radially fed into the gear at a constant rate until it reaches the desired depth (i.e., 0.4 [mm]). Overall, as can be seen in Figures 3.11 and 3.12, the feed drive motions are accurately modeled and predicted, which is essential for the correct resolution of the kinematics and CWE conditions.
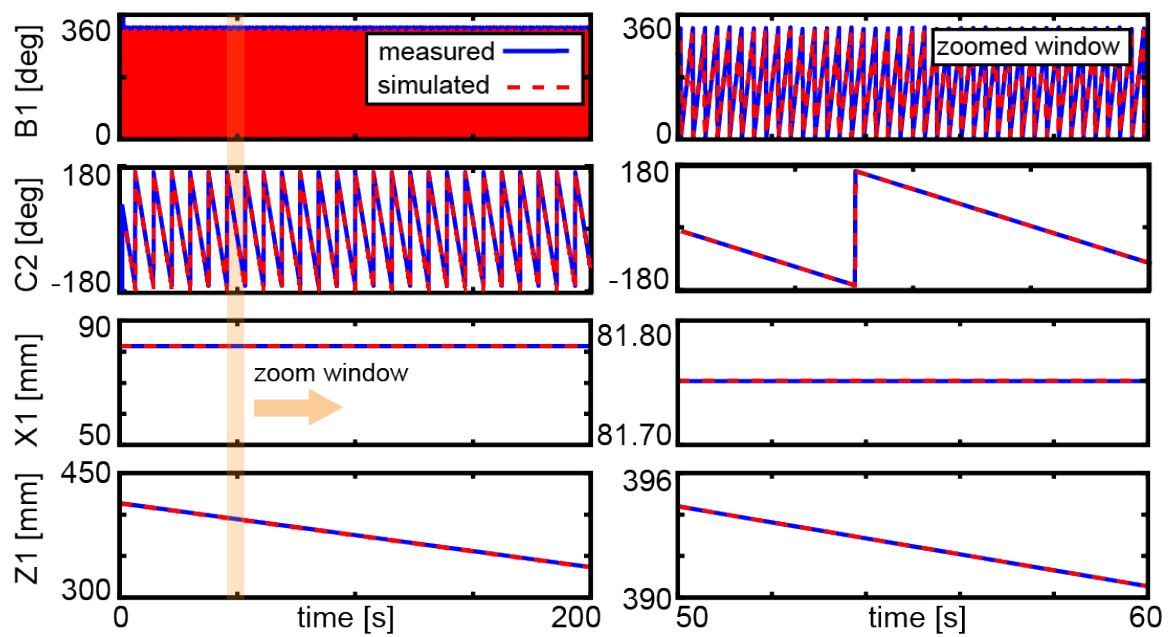
Figure 3.11: Axis trajectories: modeled and captured from the hobbing machine (one-pass process)

49
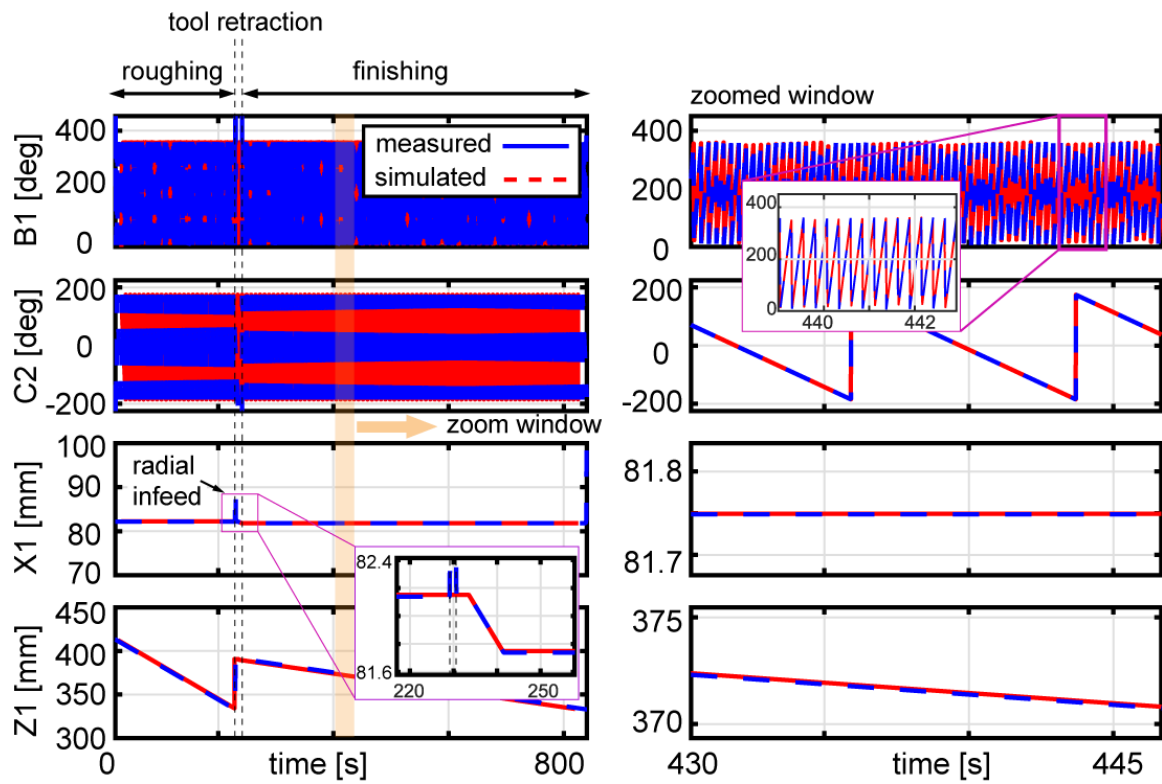
Figure 3.12: Axis trajectories: modeled and captured from the hobbing machine (two-pass process)

3.6　Conclusion

The presented mathematical model described the kinematics of hobbing process. The model is based on the geometry of the desired gear and the hob, as well as the synchronized rotation, and linear movements of the hob and gear axes. In one-pass processes, the hob is positioned at the full depth of cut and cutting occurs during an axial feeding process. In multi-pass processes, the hob is first fed radially towards the gear until it reaches the desired depth of cut, and then cutting occurs during an axial feeding process. The model uses the process parameters to predict the motion of the feed axes at any point during the cutting cycle. The active feed drive axis movements in the model have been validated experimentally using data from a Liebherr LC 500 CNC gear hobbing machine. In the proceeding chapter, the cutting velocity vectors (obtained through the developed kinematic model) will be used to resolve and predict the cutting force directions and magnitudes at discretized elements along the cutting edge of the hob.

Chapter 4

Cutter-workpiece engagement and cutting force prediction

4.1   Introduction

This chapter describes the extraction of uncut chip geometry and cutting force prediction in gear hobbing using a tri-dexel geometric engine integrated simulation model. The kinematic model developed in previous chapter moves the hob in discrete time intervals with respect to the gear. This motion is used to calculate the uncut chip geometry. The proposed simulation uses the uncut chip geometry information together with an oblique cutting force model, where the local inclination and normal rake angles vary along the discretized length of the cutting edge. The chip geometry is computed at each time step in three-dimensional space, and the force contributions from each discretization node are summed to calculate the total force vector.

The remainder of this chapter are as follows: Section 4.2 introduces the cutting force models used in this thesis. Section 4.3 through 4.6 deal with the cutter workpiece engagement calculation and extraction of uncut chip geometry. Section 4.7 explains the extraction of local cutting conditions and kinematics to predict the cutting forces in hobbing. Section

introduces the integrated cutting and metrology simulation engine, within which the hobbing process simulation was also implemented. Finally, the effects of time step and dexel resolution on the cutting force prediction are studied in Section .

4.2 Cutting force models

4.2.1 Orthogonal cutting model

The majority of cutting operations are three-dimensional and have complex geometry. However, to understand the fundamental mechanics of metal removal, a simpler but practical case of orthogonal (i.e., two-dimensional) cutting is often used. The mechanics of more complex oblique cutting (i.e., three-dimensional) operations can be analyzed by applying proper geometric and kinematic transformations to the orthogonal cutting process [3].

As shown in Figure 4.1, in orthogonal cutting, the material with a width of (b) and thickness of (h) is removed by a cutting edge that is normal to the velocity of the workpiece relative to the tool (V_c). The cut chip is then deformed and travels along the rake face of the tool with a different thickness h_c. The cutting forces in orthogonal cutting only act in the direction of the velocity and uncut chip thickness and are known as tangential force (F_t) and feed force (F_f). The cutting forces comprise both the forces generated by shearing (F_{tc} and F_{fc}) and the forces generated by "ploughing" or "rubbing" (F_{te} and F_{fe}) at the flank of the cutting edge (sometimes referred to as edge forces). Therefore, the total force components are the combination of the shearing and edge forces. The cutting forces are linearly described as follows:

$$
\begin{aligned}
F_t &= F_{tc} + F_{te} = K_{tc}bh + K_{te}b \\
F_f &= F_{fc} + F_{fe} = K_{fc}bh + K_{fe}b
\end{aligned}
\tag{4.1}
$$

Above, K_{tc} and K_{fc} are the cutting force coefficients, and K_{te} and K_{fe} are edge force coefficients. Cutting coefficients are influenced by various factors, including the workpiece

53
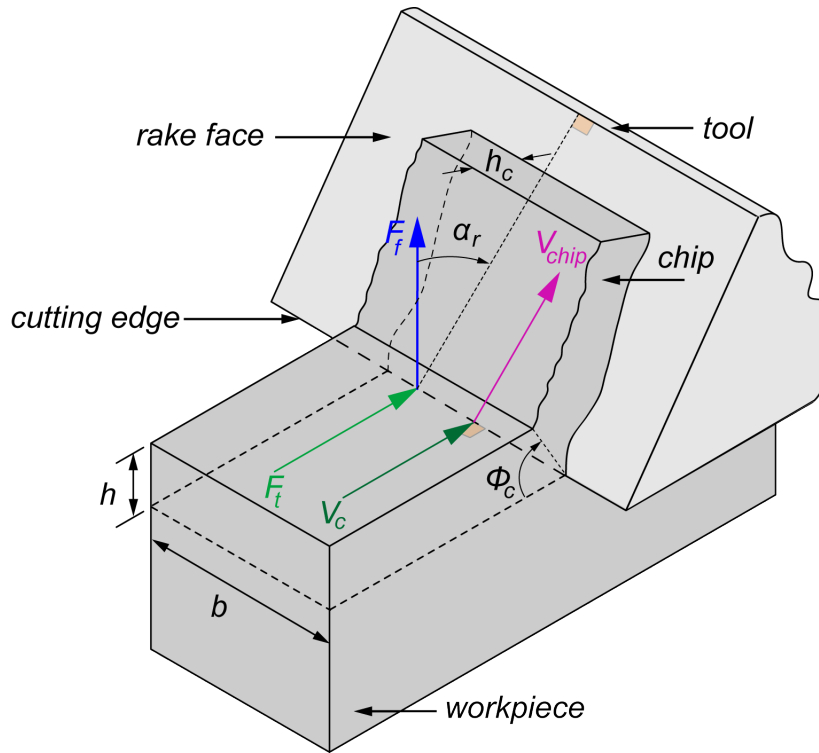
Figure 4.1: Orthogonal cutting geometry (adopted from [3])

material, cutting tool geometry, the use of coolant, lubrication, the coating of the tool, and the cutting speed. Therefore, they are usually determined mechanistically through cutting tests with known conditions.

Other parameters in the model are the tool's rake face angle (known as the tool rake angle, α_r), and the angle between the plane at which the material is being sheared and the velocity of the cutting motion (known as the shear angle, ϕ_c). These parameters are directly used in the orthogonal-to-oblique transformations which will be discussed in Section 4.2.3

4.2.2 Oblique cutting model

In the oblique cutting model, the cutting edge is no longer normal to the cutting velocity and is positioned at an angle i, called inclination angle (see Figure 4.2).
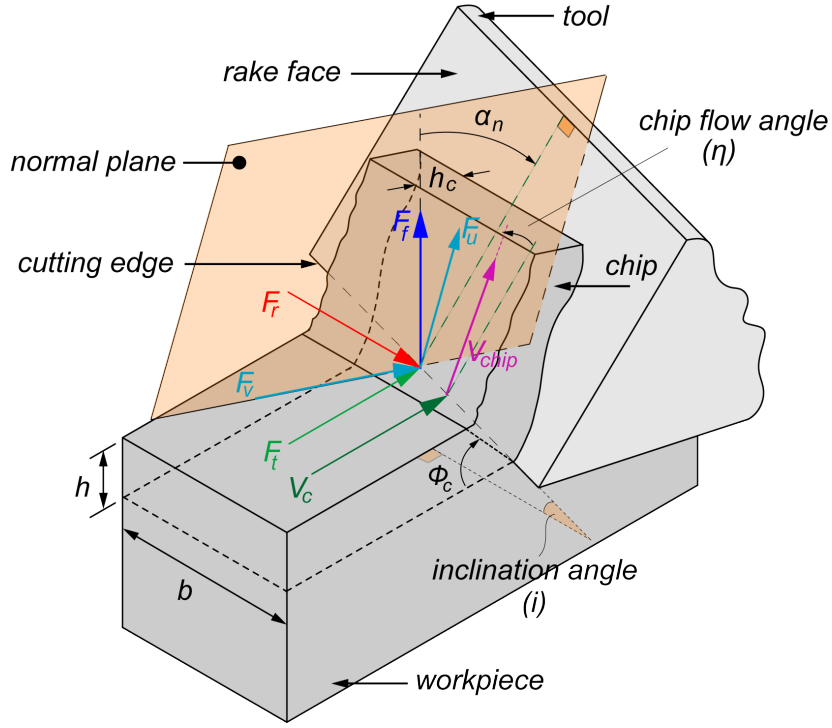
Figure 4.2: Oblique cutting geometry (adopted from [3])

There is also an additional force component in the radial direction (F_r) which is perpendicular to F_t and F_f. Like the orthogonal model, the radial force in this model linearly depends on the uncut chip thickness, the width of the chip, and the cutting coefficients:

$$
\begin{aligned}
F_t &= F_{tc} + F_{te} = K_{tc}bh + K_{te}b \\
F_f &= F_{fc} + F_{fe} = K_{fc}bh + K_{fe}b \\
F_r &= F_{rc} + F_{re} = K_{rc}bh + K_{re}b
\end{aligned}
\tag{4.2}
$$

Also, the cut chip flows at an angle (η_c) along the rake face (also called chip flow angle), which is typically approximated as the inclination angle (i) [86]. The chip flow angle denotes the angle between the cut chip velocity vector (V_{chip}) and the vector perpendicular to the rake face. [3].

The normal rake angle of the tool (α_n) is the angle between the feed direction and the

rake face, as measured in the plane that is perpendicular to the cutting edge (referred to as the normal plane).

4.2.3 Orthogonal to oblique cutting force coefficients

The cutting forces discussed in Section 4.2.1 and 4.2.2 are based on coefficients obtained from cutting tests for each workpiece material and tool geometry. The orthogonal to oblique transformation, however, uses experimentally-determined data from orthogonal cutting tests to create a generic oblique cutting force analysis [33]. This approach eliminates the need for separate calibration test for each cutter geometry and can be applied to more complex tool geometries. The orthogonal cutting model equations, developed by Merchant [32], are used to determine the shear angle (ϕ_c), shear stress (τ_s), and average friction angle at the rake face (β_a) by analyzing the measured cutting forces and chip length or thickness ratios that are collected for each test. The shear angle is calculated as:

$$\phi_c = \tan^{-1}(\frac{r_c \cos(\alpha_r)}{1 - r_c \sin(\alpha_r)}) \tag{4.3}$$

where $r_c = h/h_c$. The cutting analysis outlined here assumes that the chip is moving along the tool's surface with a consistent, average friction coefficient. However, in practice, the chip sticks to the rake face for a brief moment before sliding with a steady friction coefficient [87]. The friction coefficient is thus approximated as average value, and can be calculated as follows:

$$\beta_a = \alpha_r + \tan^{-1}(\frac{K_{fc}}{K_{tc}}) \tag{4.4}$$

The shear stress on the shearing plane is calculated as:

$$\tau_s = \frac{F_s}{A_s} = \frac{F_{tc}\cos(\phi_c) - F_{fc}\sin(\phi_c)}{\dfrac{bh}{\sin(\phi_c)}} = \sin(\phi_c)(K_{tc}\cos(\phi_c) - K_{fc}\sin(\phi_c)) \tag{4.5}$$

Above, F_s is the shearing force and A_s is the cross-sectional area of the chip on the shear plane. The oblique cutting coefficients are obtained by applying the orthogonal-to-oblique

56

transformation [33]. The cutting force coefficients (K_{tc}, K_{fc} and K_{rc}) are determined using the following equations.

$$K_{tc} = \frac{\tau_s}{\sin(\phi_n)} \frac{\cos(\beta_n - \alpha_n) + \tan(i)\tan(\eta)\sin(\beta_n)}{\sqrt{\cos^2(\phi_n + \beta_n - \alpha_n) + \tan^2(\eta)\sin^2(\beta_n)}} \tag{4.6}$$

$$K_{fc} = \frac{\tau_s}{\sin(\phi_n)\cos(i)} \frac{\sin(\beta_n - \alpha_n)}{\sqrt{\cos^2(\phi_n + \beta_n - \alpha_n) + \tan^2(\eta)\sin^2(\beta_n)}} \tag{4.7}$$

$$K_{rc} = \frac{\tau_s}{\sin(\phi_n)} \frac{\cos(\beta_n - \alpha_n)\tan(i) + \tan(\eta)\sin(\beta_n)}{\sqrt{\cos^2(\phi_n + \beta_n - \alpha_n) + \tan^2(\eta)\sin^2(\beta_n)}} \tag{4.8}$$

In the context of orthogonal-to-oblique transformations, it is assumed that the normal shear angle (ϕ_n), is equivalent to the identified shear angle (ϕ_c) in the orthogonal model, and the normal friction angle (β_n) is equivalent to the determined average friction angle (β_a) in the orthogonal model. It is also assumed that the normal rake angle (α_n) which is the projection of the oblique tool's rake angle onto the normal plane, is equivalent to the rake angle (α_r) observed in orthogonal cutting conditions.

The tangential and feed edge force coefficients (K_{te} and K_{fe}) are taken to be the same as the coefficients determined in the orthogonal cutting tests, and the radial edge coefficient (K_{rc}) is commonly assumed to be zero.

4.2.4 Kienzle cutting force coefficients

The previously-discussed cutting force models assumed a linear behavior between the uncut chip area and cutting forces. Nevertheless, research has demonstrated that cutting forces can behave non-linearly with respect to thin and small chip thickness [3]. As demonstrated experimentally, when the chip thickness reaches zero, the cutting forces converge to a non-zero value. As a result, researchers have used exponential force models wherein the cutting force coefficients increase as chip thickness approaches zero [39]. This phenomenon arises from the limited sharpness of the cutting edge, which causes the tool corner and flank contact to plow some material. The nonlinear Kienzle cutting force model [88] is

an established model in the machining literature that uses an exponential term to relate the cutting force coefficient to the uncut chip thickness. There is a friction force (F_u) and a normal force (F_v) in Kienzle's model, as shown in Figure 4.2. The normal force is perpendicular to the rake face while the friction force acts on the rake face opposite to the chip flow (and chip velocity vector) direction. The normal and friction forces are expressed as follows:

$$
\begin{aligned}
F_u &= K_u h^{-u} a = K_u b h^{1-u} \\
F_v &= K_v h^{-v} a = K_v b h^{1-v}
\end{aligned}
\tag{4.9}
$$

Kienzle's model parameters (i.e., K_u, K_v, u, and v) can be determined from cutting tests. Furthermore, similar to orthogonal-to-oblique transformations, the Kienzle model's coefficients can be converted into oblique cutting coefficients through the transformation presented in [18], as shown below:

$$
K_{tc} = K_u h^{-u} \Big(\sin(i) \sin(\eta) + \cos(i) \sin(\alpha_n) \cos(\eta) \Big) + K_v h^{-v} \Big(\cos(i) \cos(\alpha_n) \Big)
\tag{4.10}
$$

$$
K_{fc} = K_u h^{-u} \Big(\cos(\alpha_n) \cos(\eta) \Big) - K_v h^{-v} \Big(\sin(\alpha_n) \Big)
\tag{4.11}
$$

$$
K_{rc} = K_u h^{-u} \Big(-\cos(i) \sin(\eta) + \sin(i) \sin(\alpha_n) \cos(\eta) \Big) + K_v h^{-v} \Big(\sin(i) \cos(\alpha_n) \Big)
\tag{4.12}
$$

In the Kienzle model for cutting coefficients, it is generally assumed that the edge effects are captured by the cutting coefficients themselves. As such, it is assumed that the edge coefficients (K_{te}, K_{fe}, and K_{re}) are equal to zero. It is also assumed that Stabler's rule for chip flow angle approximation ($\eta = i$) is valid [86].

4.3 Cutter-workpiece engagement

In metal cutting operations, the magnitude of the cutting force is proportional to the geometry of the material removed by the cutter. Similarly, the models discussed in the previous section requires the thickness (h) and width (b) of the uncut chip geometry for cutting force calculations. As mentioned in Chapter 2, in conventional cutting operations,

58

the uncut chip geometry can be approximated analytically. However, in cutting processes such as gear hobbing wherein the CWE is complicated and the governing kinematics are complex, the analytical extraction of uncut chip geometry typically cannot be achieved readily. Instead, geometric modeling kernels are used to obtain the uncut chip geometry. Exact (e.g., BREP and CSG) and discrete (e.g., dexel and voxel-based) modelers are the two main types of geometric kernels used for CWE calculation. In computer graphics and simulations, both voxels and dexels are three-dimensional representations, but they have distinct characteristics and applications, particularly in physics-based simulation. Voxels typically require more memory compared to dexels, but are suitable for representing physical quantities or gradient with small control volumes. However, higher voxel resolutions or larger volumes result in a significant increase in memory consumption in this modeling format, which is not ideal for digital machining simulation of large workpieces. While exact modelers provide the highest accuracy, the computations become increasingly time-consuming with the large number of 3D analytical geometry entities that must be constructed and updated to keep track of each cut surface feature. In discrete modelers, the tool and workpiece are represented approximately; therefore, the CWE calculation can be performed efficiently by partially compromising the accuracy of the calculations.

In recent studies, a tri-dexel discrete geometric kernel was demonstrated to achieve a good trade-off between computational speed and prediction accuracy in the simulation of other generative gear machining operations, like shaping [74] and power skiving [70]. Thus, in this thesis, a similar efficient tri-dexel geometric kernel, ModuleWorks [89] that has been tailored to the CAD/CAM industry, is employed to extract the uncut chip geometry in hobbing.

4.4 Dexel representation

For the first time, Van Hook [28] represented a solid geometry using single-directional dexels. The intersections of dexels with a solid 3D geometry are used to create line segments called "nails" that describe the shape of the 3D geometry. Single-dexel modeling

59

is a popular method for NC machining simulation and virtual sculpting for its fast and efficient Boolean operations, little memory consumption, and simple data structures for real-time simulation [90]. However, this method can result in poor approximation in areas where the surface normals are near-perpendicular to the nail direction. To improve the representation of surfaces that are parallel to a dexel direction, multiple orthogonal dexel directions are used in literature [91]. Figure 4.3 demonstrates the improvement in geometry representation using two orthogonal dexel directions. The tri-dexel discrete volume representation used in this thesis, therefore, is expected to demonstrate better accuracy performance in predicting the 3-dimensional irregular and time-varying chip geometries encountered in hobbing, compared to its one- or two-dimensional counterparts.
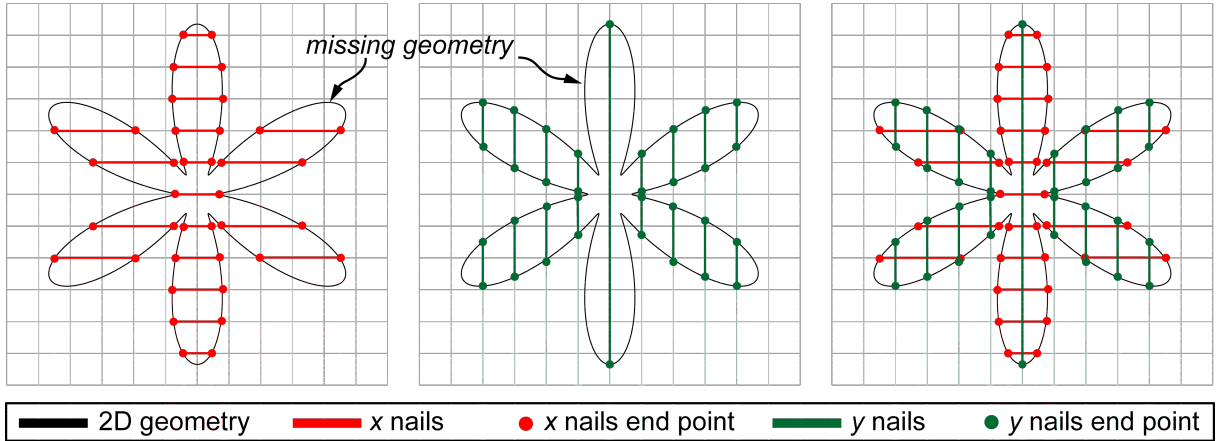
Figure 4.3: Dexel representation of a 2D geometry in one and two directions

4.5 Cutter workpiece engagement simulation

To set up the simulation, triangle mesh models of the hob and the gear blank are created based on their geometric parameters. The triangle mesh model of the workpiece is converted into dexel representation within the engine. In order to reduce the computational load, each rack profile on the hob is modeled as a thin layer extruded with infinitesimal thickness from its rake face. The gear blank is modeled as a cylinder. While the hobs in

this thesis are designed using standard rack definitions, it is possible to adjust the nominal geometric values in order to accurately represent a non-standard or modified hob provided by the manufacturer of the tool.
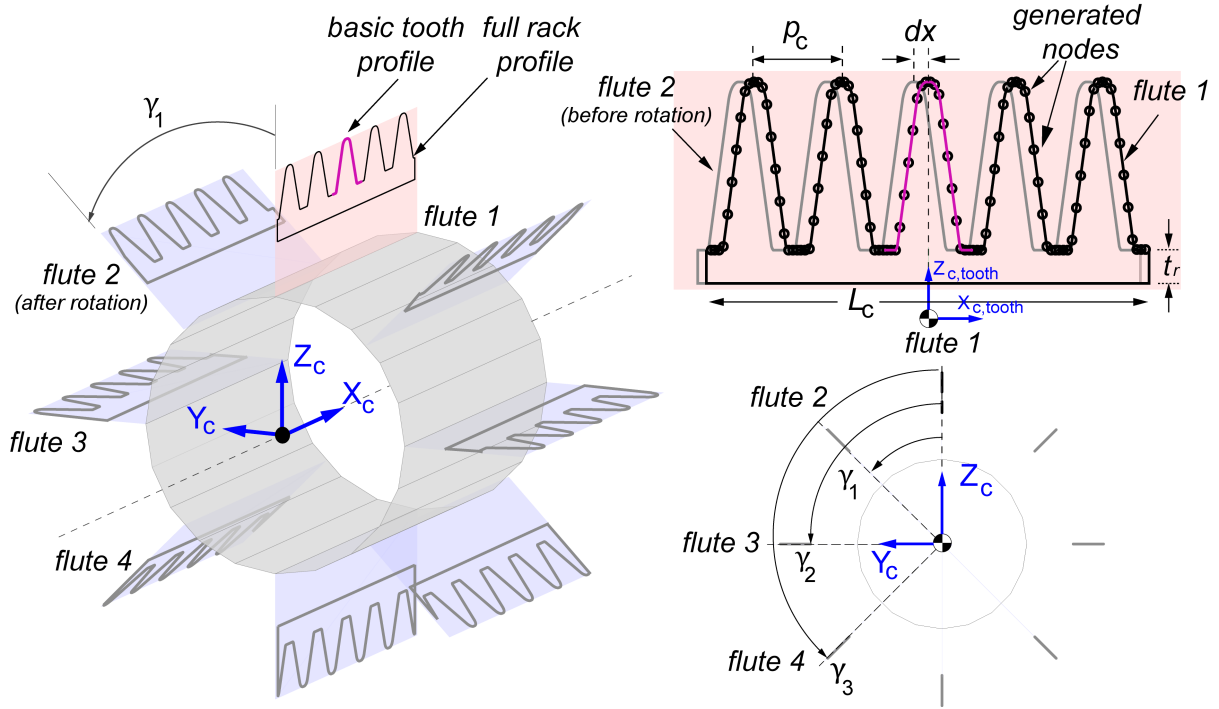
Figure 4.4: 3D hob geometry for a single start hob with 8 flutes

The racks are equally distributed around the hob's circumference. The angular distance between rack i and the first rack (γ_i) is as follows:

$$\gamma_i = (i-1)\frac{2\pi}{Z_c} \tag{4.13}$$

where Z_c is the number of flutes (or gashes) on the hob. To create the full 3D profile of a hob, the basic hob tooth profile is generated as shown in Section 3.3. This profile is assumed to be located on the first flute. Next, a full rack profile is created by repeating the basic tooth profile over the total length of the hob L_c. The start and end of the rack profile are then connected by a line that is offset from the root of the hob by a distance

61

of t_r. Each profile is shifted axially by dx to account for the effect of the axial lead (l_c as shown in equation 3.10) on the hob:

$$dx = \frac{l_c \gamma_i}{2\pi} \tag{4.14}$$

Once the rack profile is generated for each flute, points on the rack are rotated around the x axis of the hob in counterclockwise direction to generate the 3D hob:

$$\underbrace{\begin{bmatrix} x_{i,j} \\ y_{i,j} \\ z_{i,j} \end{bmatrix}}_{\substack{\text{coordinates of} \\ \text{point } j \text{ on flute } i \text{ after rotation}}} = \begin{bmatrix} 1 & 0 & 0 \\ 0 & \cos(\gamma_i) & -\sin(\gamma_i) \\ 0 & \sin(\gamma_i) & \cos(\gamma_i) \end{bmatrix} \underbrace{\begin{bmatrix} x_{0,i,j} \\ y_{0,i,j} \\ z_{0,i,j} \end{bmatrix}}_{\substack{\text{coordinates of} \\ \text{point } j \text{ on flute } i \text{ before rotation}}} \tag{4.15}$$

After establishing the points at each flute, triangular connections are formed to link all the defined points together. The triangulated cutter geometry is then utilized in the ModuleWorks engine for gear hobbing simulation. Figure 4.5 illustrates the triangulation employed to define the hobbing tool in the engine.
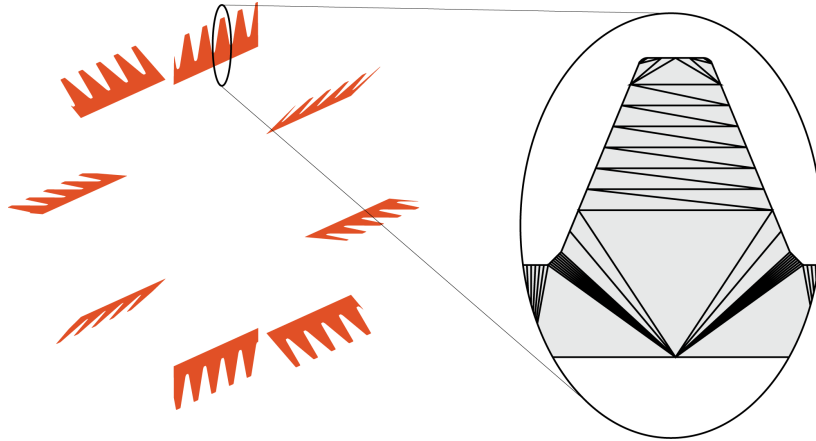
Figure 4.5: Triangular representation of hob teeth

After generating the hob and gear blank in the engine, the process parameters, (e.g., axial feed, infeed parameters, hob rotational speed, workpiece rotational speed, and feeding strategy) are used by the kinematic model to simulate the relative motion of the hob
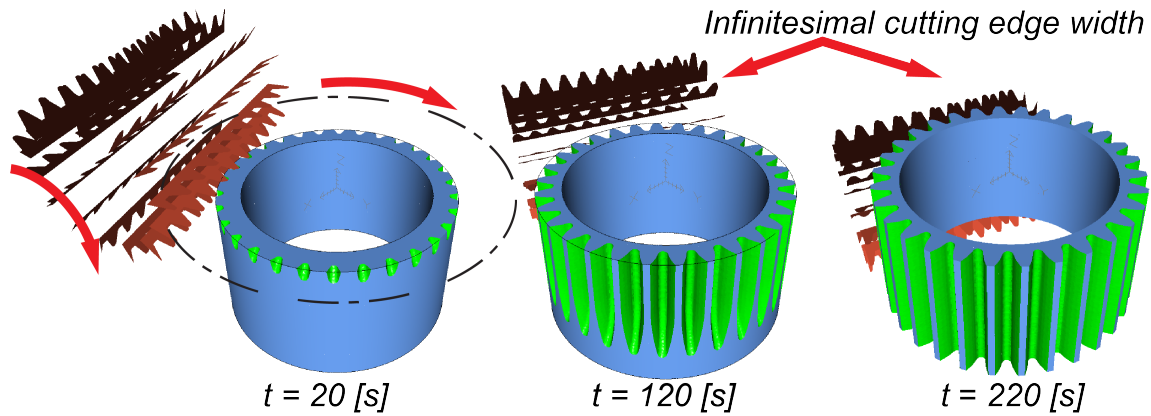
Figure 4.6: Visualization of multi-dexel based hobbing simulation in WCS

with respect to the gear blank. At each time step, a cut is performed by linearly interpolating the hob from its current position to the next one. Then, the CWE is determined based on the interference calculation. The dexels are shortened, removed, or split accordingly, resulting in the instantaneous gear blank geometry as shown in Figure 4.6. In this setup, the workpiece is stationary and hob kinematics are described in the WCS using the homogeneous transformations described in Equation 3.39.

The intersection of the cutter's swept volume and the workpiece results in an uncut chip geometry in 3D dexel format, as shown in Figure 4.7. This geometry, obtained from the ModuleWorks engine, requires further geometrical processing in order to be compatible with a cutting force model. The 3D dexel data must be intersected with the rake plane of the cutter interpolated half-way between the current and next position to obtain a cross-section of the uncut chip geometry.
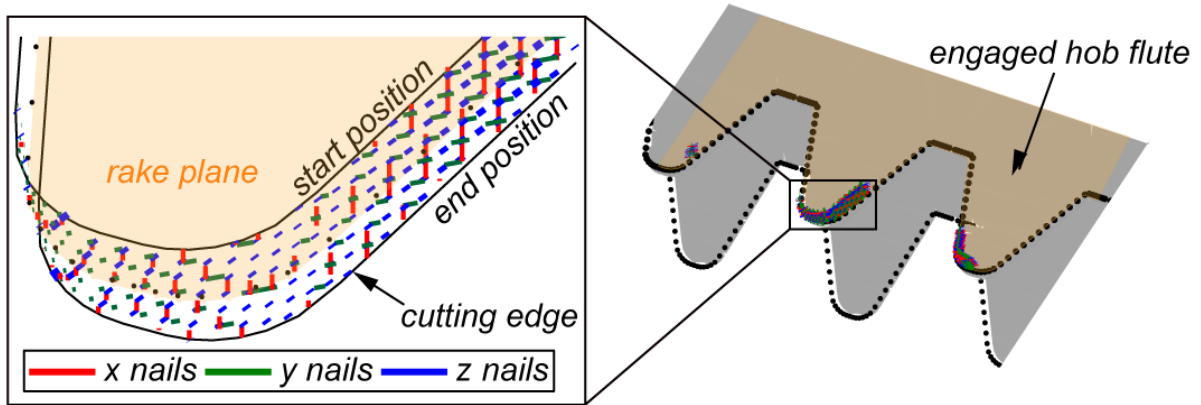
Figure 4.7: Dexel representation of 3D uncut chip geometry

4.6 2D cross-section of the chip

To construct the cross-section of the uncut chip from the 3D dexel format, a point cloud is populated on a rake face plane of the hob. The point cloud includes i) the intersection of the orthogonal x, y and z nails with the rake plane, ii) the intersection of the xy, xz and yz contours, which encapsulates the 3D geometry, with the rake face and iii) the engaged nodes along the rake face of the hob. This section will explain how each of these points are generated.

4.6.1 Dexel nail intersection

First, the point cloud is filled with intersection points of the dexel nails and the rake face plane. Each nail has two endpoints, denoted as $\boldsymbol{p_o}$ and $\boldsymbol{p_1}$, while the plane is established with a normal vector ($\boldsymbol{n}_{\mathrm{rake}}$) and a point ($\boldsymbol{p}_{\mathrm{rake}}$) lying on the rake face plane. The rake face plane is the xz plane in the TCS, with the normal of the plane oriented in the y-axis direction. As the CWE calculation is performed in the WCS the rake plane is also

represented in the WCS as follows:

$$
\boldsymbol{n}_{\text{rake}} = \underbrace{[\boldsymbol{R}_{TCS}^{WCS}]}_{\substack{\text{interpolated} \\ \text{rotation matrix}}}
\begin{bmatrix}
1 & 0 & 0 \\
0 & \cos(\gamma_i) & -\sin(\gamma_i) \\
0 & \sin(\gamma_i) & \cos(\gamma_i)
\end{bmatrix}
\begin{bmatrix}
0 \\
1 \\
0
\end{bmatrix}
\tag{4.16}
$$

$$
\boldsymbol{p}_{\text{rake}} = \underbrace{[\boldsymbol{H}_{TCS}^{WCS}]}_{\substack{\text{interpolated} \\ \text{transformation matrix}}}
\begin{bmatrix}
1 & 0 & 0 & 0 \\
0 & \cos(\gamma_i) & -\sin(\gamma_i) & 0 \\
0 & \sin(\gamma_i) & \cos(\gamma_i) & 0 \\
0 & 0 & 0 & 1
\end{bmatrix}
\begin{bmatrix}
0 \\
0 \\
r_{pc} \\
1
\end{bmatrix}
\tag{4.17}
$$

The intersection point is determined by first computing the projection distance of each nail endpoint onto the rake plane. This can be expressed as:

$$
\boldsymbol{d_o} = (\boldsymbol{p_o} - \boldsymbol{p}_{\text{rake}}) \cdot \boldsymbol{n}_{\text{rake}}
\tag{4.18}
$$

$$
\boldsymbol{d_1} = (\boldsymbol{p_1} - \boldsymbol{p}_{\text{rake}}) \cdot \boldsymbol{n}_{\text{rake}}
\tag{4.19}
$$

Assuming that the endpoints are positioned on opposite sides of the plane, the intersection point is obtained as follows:

$$
\boldsymbol{p_x} = \boldsymbol{p_o} + |\boldsymbol{d_o}| \frac{\boldsymbol{p_1} - \boldsymbol{p_o}}{|\boldsymbol{d_o}| + |\boldsymbol{d_1}|}
\tag{4.20}
$$

4.6.2   Contour intersection

It is possible to get an inaccurate estimate of the 2D cross-section, when the intersection of the dexel nails are only considered, especially when the chip geometry is thin and the resolution of the dexel nails are insufficient (see Figure 4.8.a).

In order to improve the representation of the 2D chip, a technique is used to generate sets of contours by approximating the outer surface of the 3D dexels. This method is based on a simplified version of a technique developed by Zhang [91] that reconstructs 3D surface from a tri-dexel data representation. The author applied this technique to determine uncut chip geometry in hobbing, while it was initially developed by Andrew
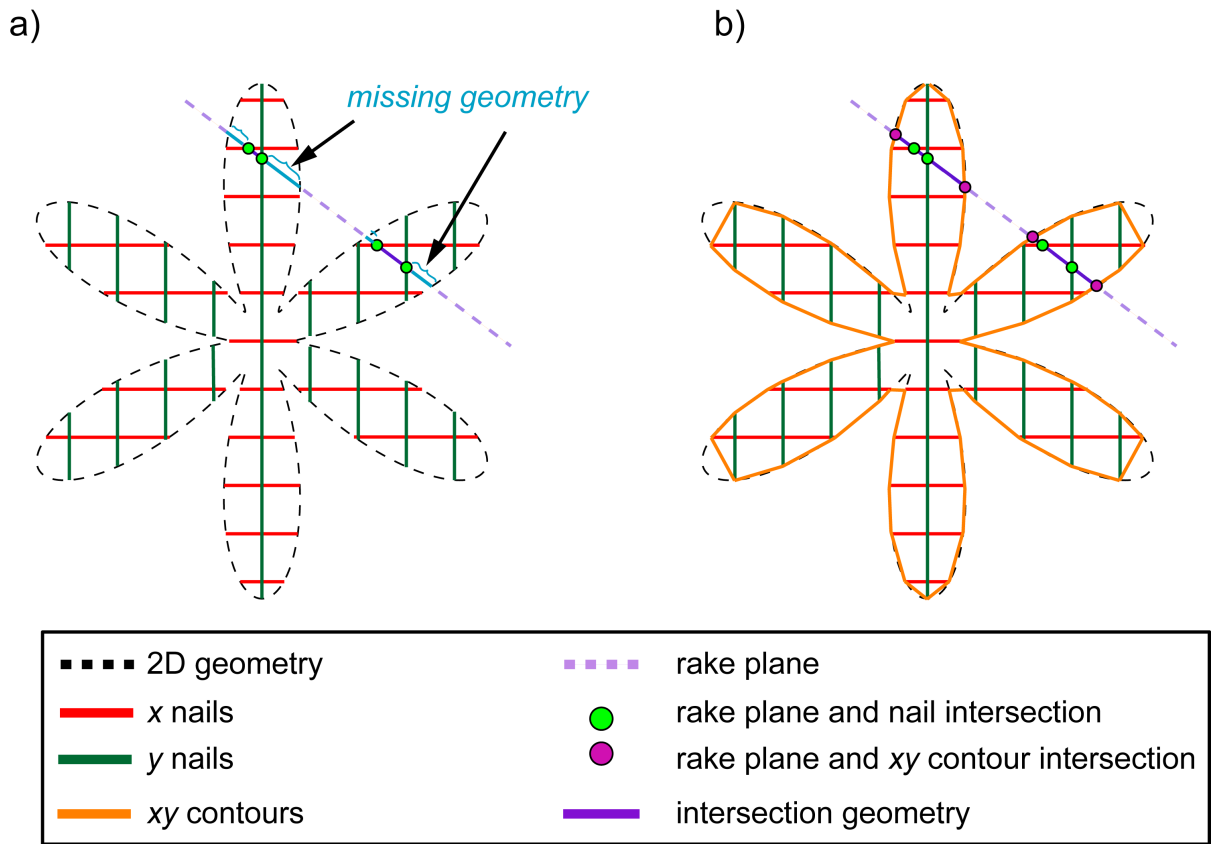
Figure 4.8: a) Poor approximation of intersection geometry only using dexel nail b) improved intersection geometry approximation using xy contours along with dexel nail intersections

Katz at the University of Waterloo. To create the xy contours, nails oriented in the x and y directions at the same z height are grouped together and sorted by ascending dexel index. Line segments are drawn between the endpoints of each nail and its neighboring nails, with the additional step of drawing a line to the closest endpoint of any orthogonal nail that intersects a neighboring nail before connecting to the neighboring nail's endpoint. This process is repeated until all subsequent nails are connected, resulting in a set of connections on an xy plane known as an xy contour.

The outer geometry of the 3D chip is described using a contour generation method

that is applied to every plane with dexel nails, including *xy*, *xz*, and *yz*. This results in a set of contours that can be used to improve the estimate of the chip's cross-section by intersecting them with the rake face plane, as demonstrated in Figure 4.8.b. However, there may still be discrepancies between the actual shape and the estimated shape defined by the outer contours due to the limitations of the dexel nail resolution in the simulation, which constrain the accuracy of the outer contours. For this reason, the dexel resolution study has been carried out, as reported in Section 4.9.

4.6.3 Engaged nodes

The edge of the hob is divided into points called nodes as shown in Figure 4.4. For each node, a 3D local force contribution, based on the oblique cutting force model, is to be computed. The nodes are created on the full rack profile of the hob using its geometric data (as discussed in section 4.5). In this study, no global rake angle is assumed on the hob and thus, the nodes on the rake plane represent the discretized cutting edge. However, for hobs with a global rake angle, the nodes on the rack plane must be transformed based on the rake face model to represent the discretized cutting edge, as was previously demonstrated for shaping [75] and power skiving [69] cutters. Nodes on the hob that fall within a particular distance of a point in the point cloud are referred to as engaged nodes. The distance is set to the dexel resolution (d_{dexel}), which is the distance between two neighboring nails, and is set when configuring the simulation. These engaged nodes are then combined with the intersection points computed, as discussed in Sections 4.6.1 and 4.6.2 to establish a 2D uncut chip geometry, which is explained in the following section.

4.6.4 Point cloud triangulation

The alpha shape method [92] is utilized to reconstruct the geometry of a chip from a point cloud by determining the shape of a set of points on a plane. Initially, the Delaunay triangulation is computed, which is a non-overlapping triangulation of the point set, wherein the circumcircle of each triangle does not enclose any other point. A circumcircle is defined

67
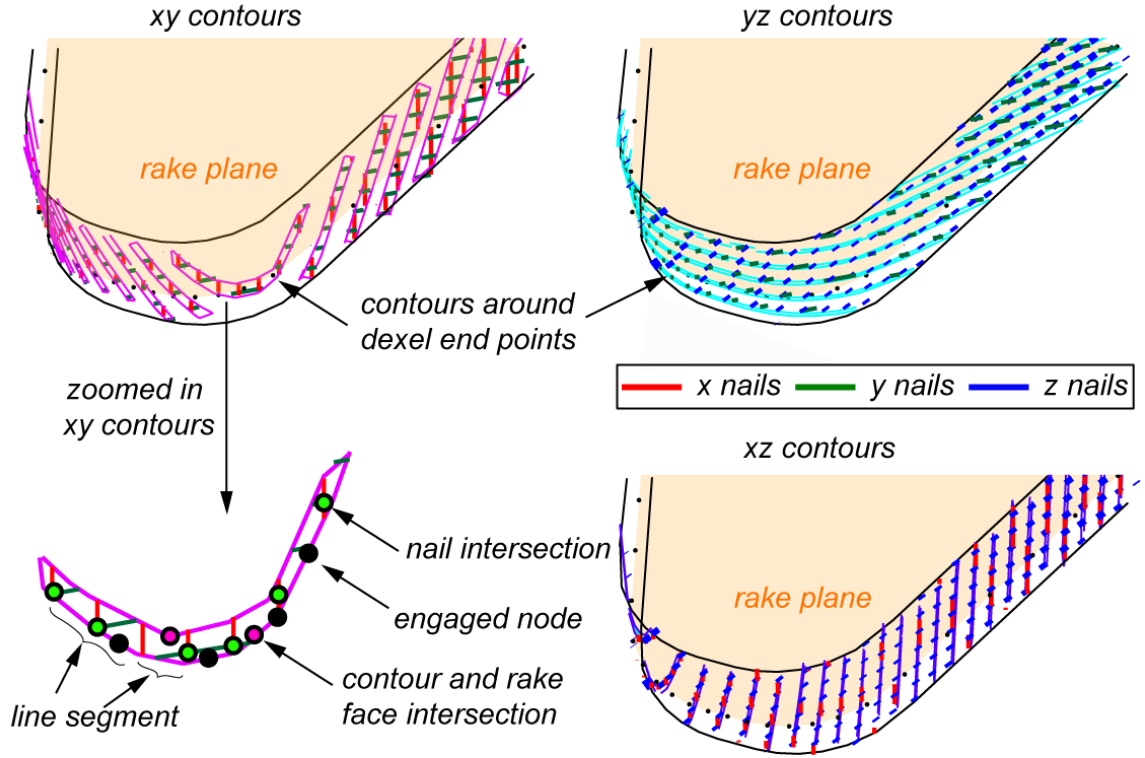
Figure 4.9: Encapsulation of 3D uncut chip geometry with contours

as the circle that passes through all three points defining a triangle, and its coordinates (x_c, y_c) can be determined as [93]:

$$
\begin{aligned}
x_c &= \frac{(x_0^2 + y_0^2)(y_2 - y_1) + (x_1^2 + y_1^2)(y_0 - y_2) + (x_2^2 + y_2^2)(y_1 - y_0)}{2(x_0(y_2 - y_1) + x_1(y_0 - y_2) + x_2(y_1 - y_0))} \\
y_c &= \frac{(x_0^2 + y_0^2)(x_1 - x_2) + (x_1^2 + y_1^2)(x_2 - x_0) + (x_2^2 + y_2^2)(x_0 - x_1)}{2(x_0(y_2 - y_1) + x_1(y_0 - y_2) + x_2(y_1 - y_0))}
\end{aligned}
\tag{4.21}
$$

The circle radius (r_c) is calculated below [93]:

$$
r_c = \sqrt{(x_c - x_0)^2 + (y_c - y_0)^2}
\tag{4.22}
$$

Several algorithms exist for computing the Delaunay triangulation, each with different levels of efficieny and complexity. In this thesis, the Bowyer-Watson algorithm [94] is

used for DT for its simplicity. The Delaunay triangulation is created by connecting all the points in the given set using non-overlapping triangles, with the condition that the circumscribed circles of each triangle do not contain any other points. To achieve this, a 'super triangle' is formed which enclose all of the points in the given set. Subsequently, the points are inserted one by one into the triangulation. Any triangle whose circumscribed circle encompasses the new point is eliminated, and new triangles are formed utilizing the vertices of the removed triangles and the new point. Once all of the points have been inserted, the vertices of the 'super triangle' that originally surrounded all of the points are removed, as well as any associated triangles. After performing the Delaunay triangulation, the next step in the alpha shape method is to set a size threshold (d_α) to the triangles. The Delaunay triangulation produces a convex hull that may not precisely reflect the chip's geometry. Thus, it is necessary to remove triangles whose longest edges exceed the established alpha shape threshold thereby representing the cross-section of the uncut chip accurately. Herein, the alpha shape threshold is chosen to be $\sqrt{2}d_{\mathrm{dexel}} \leq d_\alpha \leq \sqrt{3}d_{\mathrm{dexel}}$ based on the orientation of the 3D rake plane. In the final triangulation of the chip's uncut cross-section, every triangle is associated with the node that has the shortest distance from the center point of that triangle. The effective area of the chip associated with each node is calculated by summing the areas of each associated triangle. This geometry of the chip is used to predict the cutting forces. Heron's formula [95] is used to calculate the area of a triangle (Δ) in three dimensions, given the coordinates of its three vertices:

$$
\begin{aligned}
\Delta &= \sqrt{s(s - l_{01})(s - l_{02})(s - l_{12})} \\
l_{01} &= \sqrt{(x_0^2 - x_1^2) + (y_0^2 - y_1^2) + (z_0^2 - z_1^2)} \\
l_{02} &= \sqrt{(x_0^2 - x_2^2) + (y_0^2 - y_2^2) + (z_0^2 - z_2^2)} \\
l_{12} &= \sqrt{(x_1^2 - x_2^2) + (y_1^2 - y_2^2) + (z_1^2 - z_2^2)} \\
s &= \frac{l_{01} + l_{02} + l_{12}}{2}
\end{aligned}
\tag{4.23}
$$

By adding up the areas of all triangles associated with a node, the local uncut chip area is computed which is then utilized to determine the local tangential, feed, and radial forces.
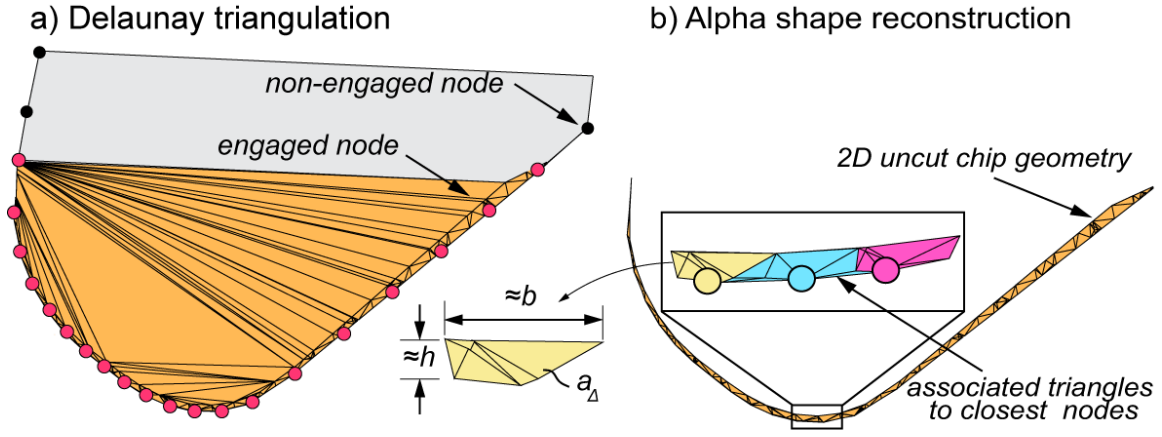
Figure 4.10: Delaunay triangulation and alpha shape reconstruction performed on the 2D point cloud

4.7 Cutting force calculation

4.7.1 Local cutting geometry and kinematics

The magnitude and orientation of local cutting forces vary along the cutting edge of the tool. The orientation of the force components is determined based on the relative velocity vector $\boldsymbol{V_c}$, representing the direction of the workpiece material flow, and cutting edge geometry. Furthermore, application of the orthogonal-to-oblique transformation requires estimation of the local rake (α_n) and inclination (i) angles, both of which influence the local cutting force coefficients. Figure 4.11 shows the major vectors, angles, and orientation required for the oblique cutting model as applied to an engaged node on the hobbing flute.

The tangential direction unit vector ($\boldsymbol{t}$) is defined in the opposite direction of the relative velocity unit vector of the cutting edge ($\boldsymbol{V_c}$):

$$\boldsymbol{t} = -\frac{\boldsymbol{V_c}}{|\boldsymbol{V_c}|} \tag{4.24}$$

The edge vector is defined to approximate the local cutting edge of the hob using the
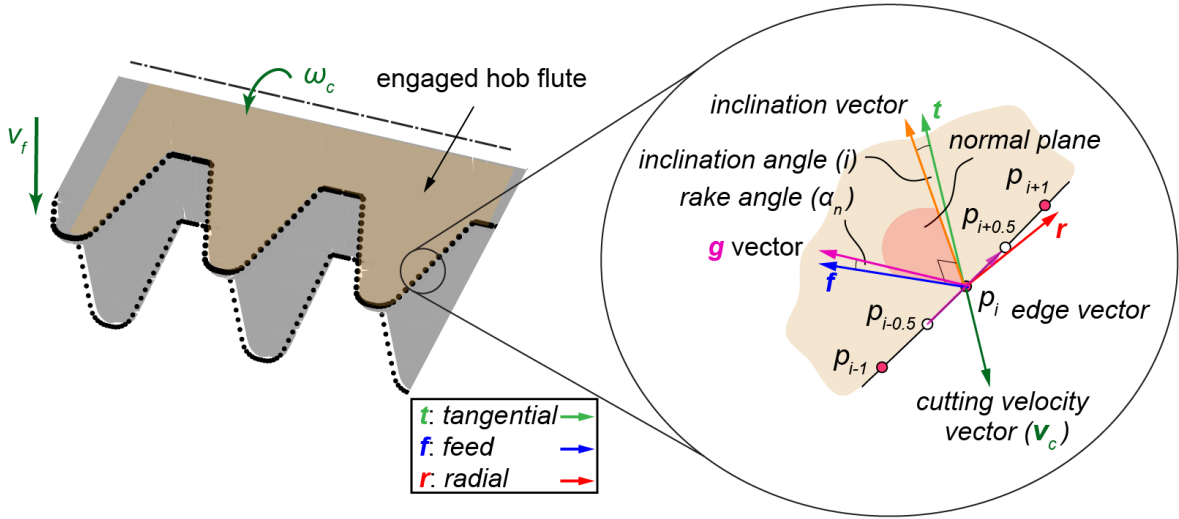
Figure 4.11: Principal cutting directions and local rake and inclination angles

engaged node ($\boldsymbol{p}_i$) and its neighboring nodes ($\boldsymbol{p}_{i-1}$ and $\boldsymbol{p}_{i+1}$) coordinates. A midpoint between the current and previous nodes ($\boldsymbol{p}_{i-0.5}$) and between the current and the subsequent nodes ($\boldsymbol{p}_{i+0.5}$) is defined to establish the edge vector as follows:

$$\boldsymbol{e_n} = \boldsymbol{p}_{i+0.5} - \boldsymbol{p}_{i-0.5} = \frac{\boldsymbol{p}_{i+1} + \boldsymbol{p}_i}{2} - \frac{\boldsymbol{p}_i + \boldsymbol{p}_{i-1}}{2} \tag{4.25}$$

The unit edge vector ($\boldsymbol{e}$) is then defined as:

$$\boldsymbol{e} = \frac{\boldsymbol{e_n}}{|\boldsymbol{e_n}|} \tag{4.26}$$

where $|\boldsymbol{e_n}|$ is the magnitude of the edge vector.

The uncorrected unit feed vector direction ($\boldsymbol{f_u}$) is then calculated as the cross-product of the edge and tangential unit vectors:

$$\boldsymbol{f_u} = \boldsymbol{e} \times \boldsymbol{t} \tag{4.27}$$

The direction seed vector ($\boldsymbol{d_s}$) is used to ensure that the feed vector is pointing in the right direction (i.e., angle between feed and seed vector is less than $180°$). Assuming the

nodes go around the hob in the clockwise direction, the direction seed vector is defined as a forward tangent vector connecting two neighboring nodes. Thus, the corrected unit feed vector $\boldsymbol{f}$ becomes:

$$\boldsymbol{f} = \begin{cases} \boldsymbol{f_u}, & \boldsymbol{f_u} \cdot \boldsymbol{d_s} > 0 \\ -\boldsymbol{f_u}, & \boldsymbol{f_u} \cdot \boldsymbol{d_s} < 0 \end{cases} \tag{4.28}$$

The local inclination vector ($\mathbf{i}$) is calculated as the cross-product of feed and edge unit vectors:

$$\boldsymbol{i} = \boldsymbol{f} \times \boldsymbol{e} \tag{4.29}$$

Then, the local inclination angle (i), defined between the inclination vector and tangent vectors, is calculated as follows:

$$i = \cos^{-1}(\boldsymbol{i} \cdot \boldsymbol{t}) \tag{4.30}$$

The (uncorrected) radial unit vector ($\boldsymbol{r_u}$) is perpendicular to the tangent and feed unit vectors, and is calculated as:

$$\boldsymbol{r_u} = \boldsymbol{t} \times \boldsymbol{f} \tag{4.31}$$

However, the direction of $\boldsymbol{r_u}$ must be corrected to ensure that the inclination unit vector creates an acute angle (less than 180°) with the radial unit vector ($\boldsymbol{r}$):

$$\boldsymbol{r} = \begin{cases} \boldsymbol{r_u}, & \boldsymbol{r_u} \cdot \boldsymbol{i} > 0 \\ -\boldsymbol{r_u}, & \boldsymbol{r_u} \cdot \boldsymbol{i} < 0 \end{cases} \tag{4.32}$$

The local chip width (b) is approximated by projecting the length of the edge vector onto the radial vector using the inclination angle:

$$b = |\boldsymbol{e}| \cos(i) \tag{4.33}$$

As shown in Figure 4.10, the local chip thickness (h) is approximated using the local chip area and the chip width:

$$h = \frac{a_\Delta}{b} \tag{4.34}$$

In the last step, the normal rake angle α_n is calculated. The rake face geometry of the hob influences the local rake angle. To capture this effect, a local rake unit vector ($\boldsymbol{g}$) is initially established by intersecting the normal plane (which is perpendicular to the cutting edge, see Figure 4.11) and the rake plane. While the rake face geometry of the hob can be a curved surface, in this thesis, only planar rake face geometry is considered. Thus, the rake vector is calculated as:

$$\boldsymbol{g} = \boldsymbol{n}_\text{rake} \times \boldsymbol{n}_\text{normal plane} \tag{4.35}$$

Finally, the normal rake angle is defined as the angle between the unit feed direction and the rake vector ($\boldsymbol{g}$) evaluated at the normal plane.

$$\alpha_n = \cos^{-1}(\boldsymbol{g} \cdot \boldsymbol{f}) \tag{4.36}$$

The negative normal rake angle case occurs when $\boldsymbol{g} \cdot \boldsymbol{i} < 0$, thus, the necessary sign change must be applied to equation 4.36.

Figure 4.12 demonstrates the rake and inclination angle profiles at different nodes along the cutting edge, for the process parameters defined in Tables 3.2, 3.3 and 3.4. Points A and C are examples of the engaged nodes when the hob axis is 6.42 mm below the top of the gear blank. Point B, however, represents a non-engaged node at the same axial position. As seen, the variation of these angles along the cutter teeth is limited to only a few degrees, whereas in certain other gear-cutting operations, like power skiving, their variation can be tens of degrees [70]. Furthermore, α_n and i remain nearly constant at individual nodes during the cut. This enables the application of a simple 2D uncut chip model. Similar to Figure 4.12, Figure 4.13 displays the variation of the local chip attributes (i.e., area, width, and thickness) along the cutting edge while the hob travels downward axially.

4.7.2 Local cutting forces

The unit vectors $\boldsymbol{t}$, $\boldsymbol{f}$, and $\boldsymbol{r}$ help orient the scalar cutting forces contributed by each engaged node, to their respective directions. This allows for the force contributions across
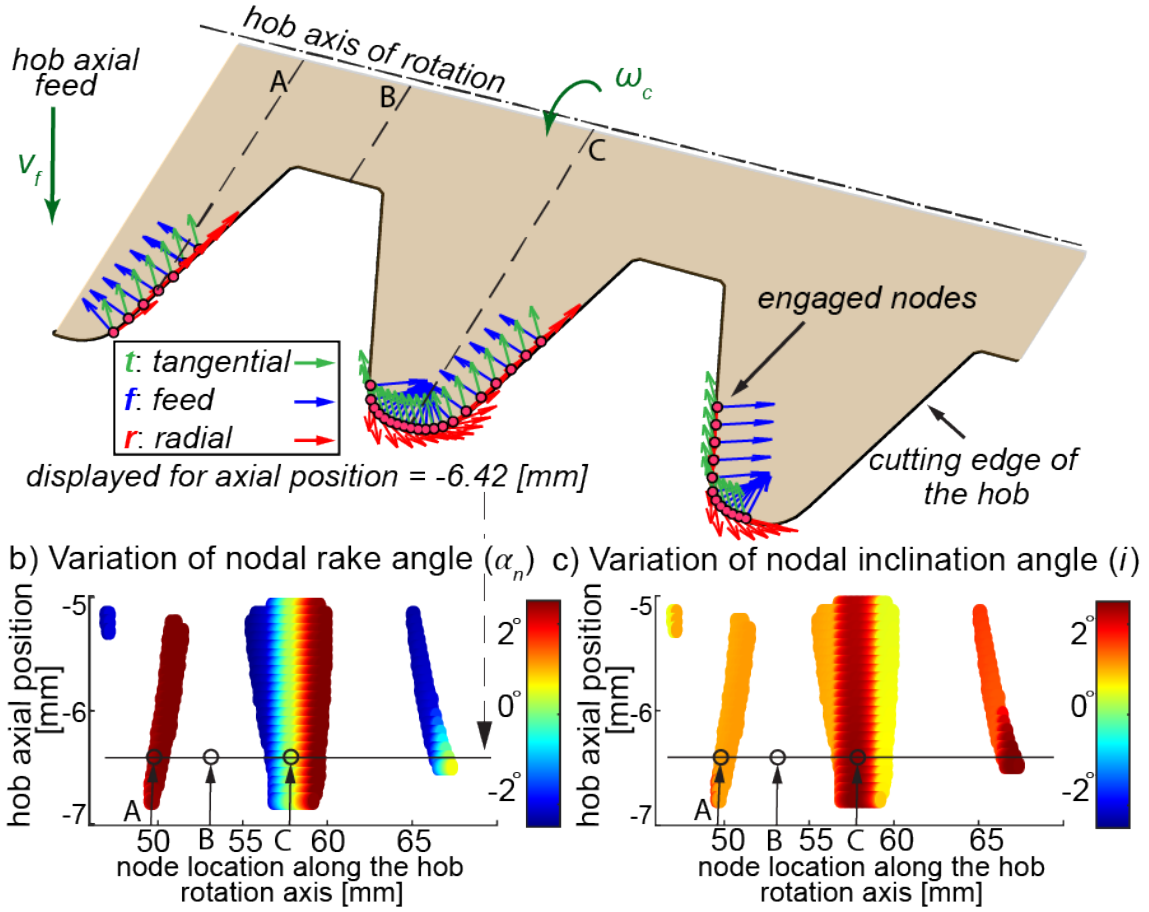
Figure 4.12: Distribution of inclination and rake angles over the cutting edge of the hob

all engaged nodes to be correctly added as vectors at each time step. The local tangential, feed, and radial forces (dF_t, dF_f, and dF_r) for each engaged node are calculated using the generalized oblique model as follows:

$$
dF_{t,f,r} = \left\{ K_{(t,f,r)c}(h, |\boldsymbol{V}_c|, ...) \underbrace{\sum_{\substack{\text{associated} \\ \text{triangles}}} (\varDelta)}_{\text{chip area, } a_\varDelta} \right\} + \left\{ K_{(t,f,r)e}(h, |\boldsymbol{V}_c|, ...) b \right\}
\tag{4.37}
$$

Above, $\varDelta$ is the area of each triangle which is calculated in equation 4.23. In the context of Kienzl's force model, the effect of edge forces are included in the cutting force coefficients

74
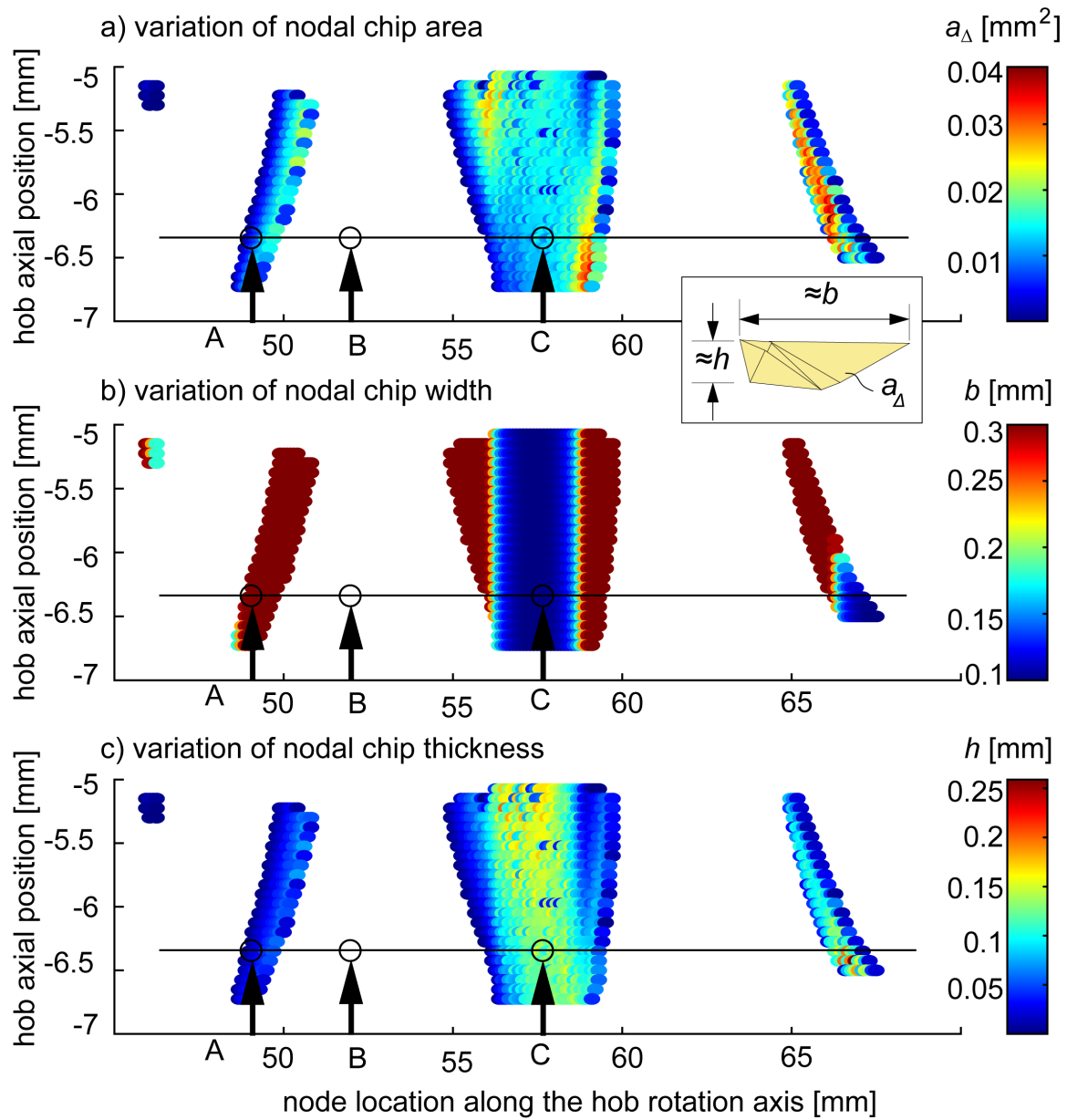
Figure 4.13: Distribution of local chip area (a), width (b), and thickness (c) over the cutting edge of the hob

and thus edge force coefficients are assumed to be zero. Finally, the total cutting force at each time step is determined by adding the local cutting forces from each node:

$$\bar{F}^{WCS} = \sum_{\substack{\text{associated} \\ \text{nodes}}} (dF_t \boldsymbol{t}^{WCS} + dF_f \boldsymbol{f}^{WCS} + dF_r \boldsymbol{r}^{WCS}) \tag{4.38}$$

The tangential, feed and radial directions were defined in the tool coordinate systems, thus they must be transformed into the workpiece coordinate system. The tangential unit vector in the WCS is determined as:

$$\underbrace{\boldsymbol{t}^{WCS}}_{\substack{\text{tangential} \\ \text{vector in WCS}}} = \underbrace{\boldsymbol{R}_{TCS}^{WCS}}_{\substack{\text{rotation matrix} \\ \text{between tool} \\ \text{and workpiece}}} \underbrace{\boldsymbol{t}^{TCS}}_{\substack{\text{tangential} \\ \text{vector in TCS}}} \tag{4.39}$$

The feed and radial unit vectors in the WCS are calculated similarly:

$$\boldsymbol{f}^{WCS} = \boldsymbol{R}_{TCS}^{WCS} \boldsymbol{f}^{TCS} \tag{4.40}$$

$$\boldsymbol{r}^{WCS} = \boldsymbol{R}_{TCS}^{WCS} \boldsymbol{r}^{TCS} \tag{4.41}$$

4.8   Hobbing integrated simulation engine

The hobbing simulation engine developed in this thesis uses a time-domain simulation that integrates the kinematic model, engagement geometry, and local cutting condition calculations. At each time step, the tool's position relative to the workpiece is determined by the kinematic model. The 3D CWE geometry is then calculated and used to predict the local cutting forces, which are summed to generate a final cutting force prediction. This process is repeated until the final gear is produced. The simulation has been incorporated inside an integrated gear machining and metrology simulation suite earlier developed at the University of Waterloo [75]. Figure 4.14 shows the extracted chip geometry and the simulated cutting forces for Trial 1 (introduced in Tables 3.2, 3.3, and 3.4).

76

a) chip geometry variation

b) predicted cutting forces expressed in WCS
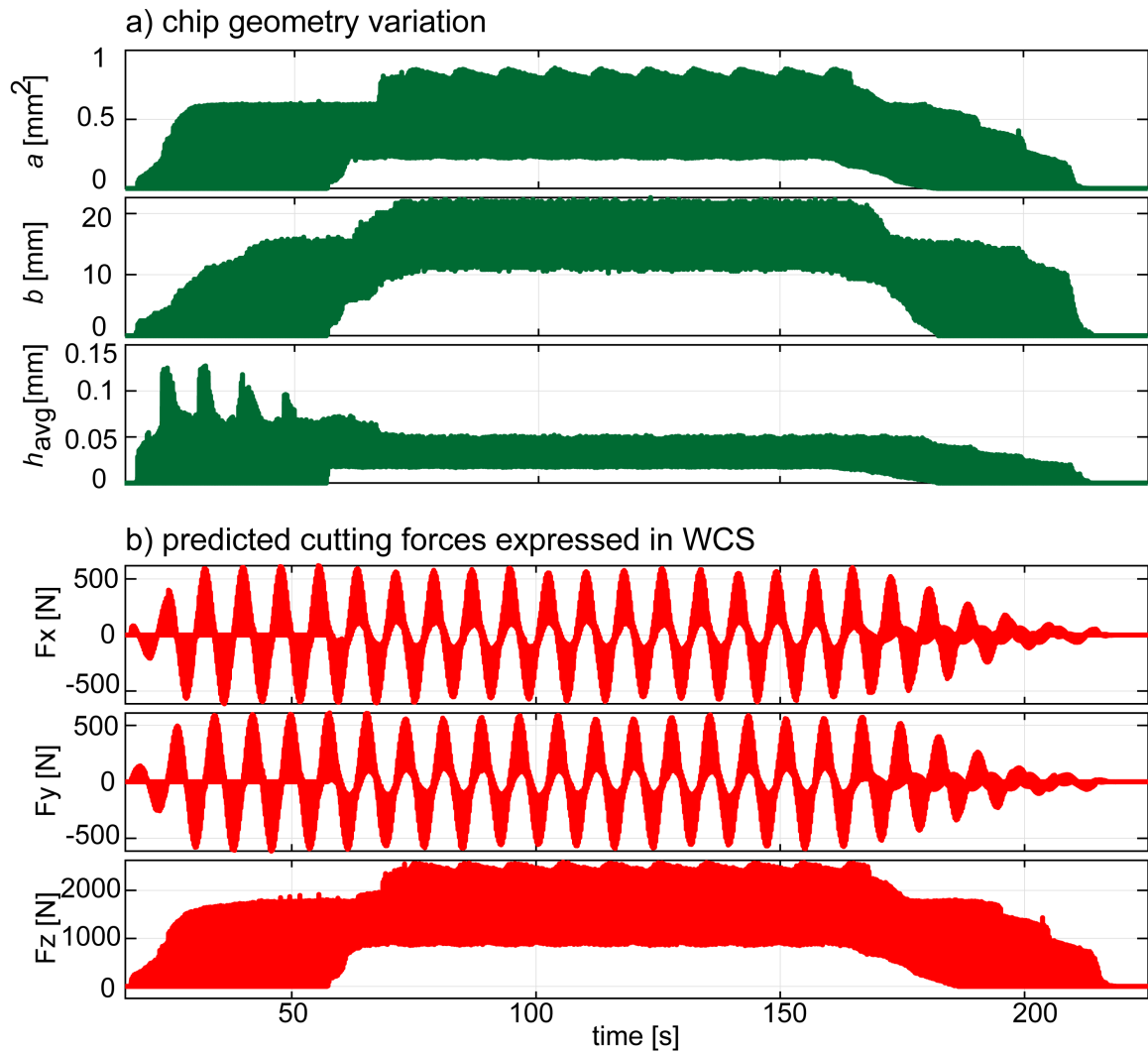
Figure 4.14: Simulated chip geometry and cutting forces for Trial 1

4.9 Dexel and time step resolution study

In the context of cutting force prediction using discrete geometric modelers, a dexel and time step resolution study is crucial to ensure accurate and reliable results. On the one hand, fine dexel and time step resolution are necessary for capturing the complex geometry and physics of hobbing. On the other hand, the computational cost of the problem grows

quickly if these parameters are unnecessarily chosen to be too fine. Figure 4.15 demonstrates the cutting force simulation results for different dexel resolution values while the time step of the simulation is kept constant as 1 ms (1 ms is equivalent to 1.38° of hob rotation). As can be seen, by reducing the dexel resolution from 0.5 mm to 0.3 mm, the simulation converges and becomes less dependent on the dexel resolution value (0.3 mm is about 10% of the gear module).
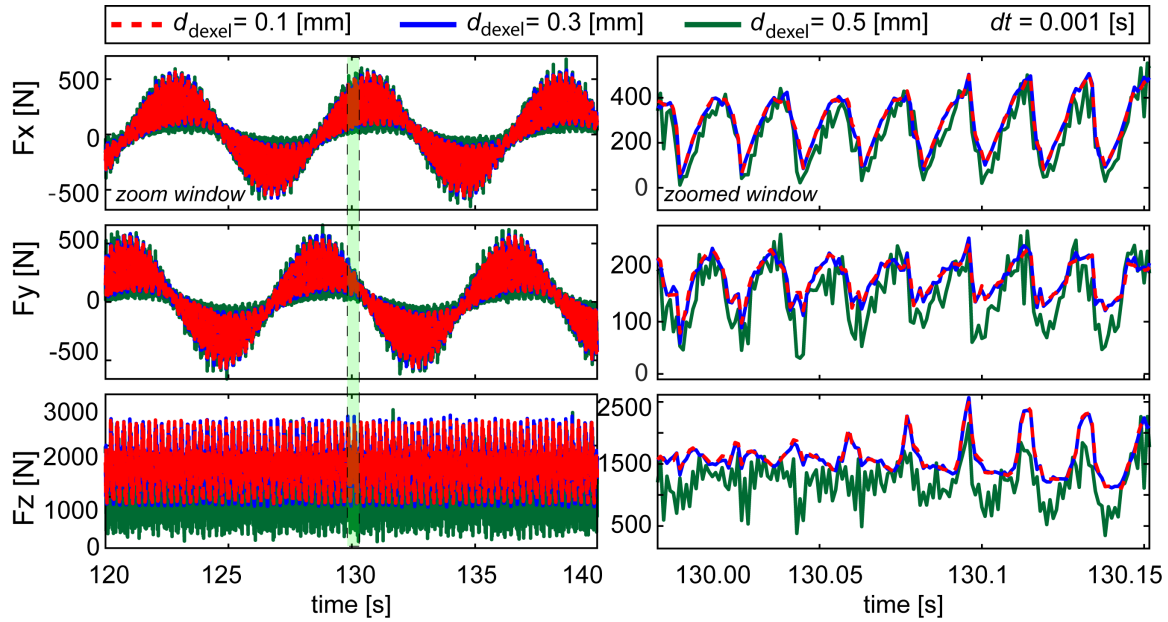
Figure 4.15: Effect of dexel resolution on the cutting force prediction results

Figure 4.16 illustrates the impact of adjusting the time step on the simulation results, with a dexel resolution of 0.1 mm. When the time step is set to 10 ms, the simulation is mainly capable of predicting the low-frequency component of the forces. However, when the time step is reduced to smaller values (5, 1, and 0.5 ms), the force prediction results begin to converge and become less dependent on the time step. A time step of 1 ms corresponds to approximately 18.6 simulation sample points for the highest frequency component in the force profile, which is the tooth passing frequency, i.e., 53.66 Hz. In the simulation performed to validate the cutting forces in Chapter 5, the dexel resolution and time step were chosen to be 0.1 mm and 1 ms, respectively. Moreover, it is not possible to adjust

78

the dexel resolution and time step separately. If the time step is set to a very small value while the dexel resolution is low, there may not be enough CWE data during each time step of the simulation, as shown in Figure 4.17. Thus, care must be taken when selecting these parameters.
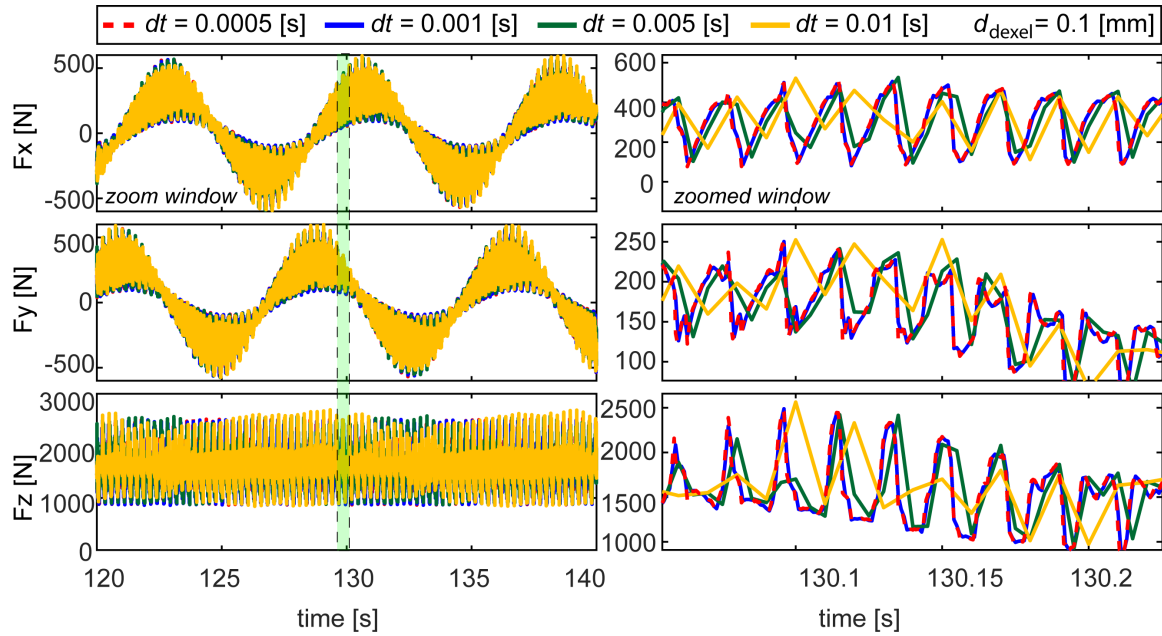
Figure 4.16: Effect of time step on the cutting force prediction results

Figure 4.17 displays the RMS error comparison of the different resolution values in relation to the finest resolution simulated (i.e., $dt = 1$ ms and $d_{dexel} = 0.1$ mm). The results show that as long as $dt \leq 3$ ms and $d_{dexel} \geq 0.2$ mm, the calculated RMS error for chip area and cutting forces remains within 5% of the results with the finest resolution.
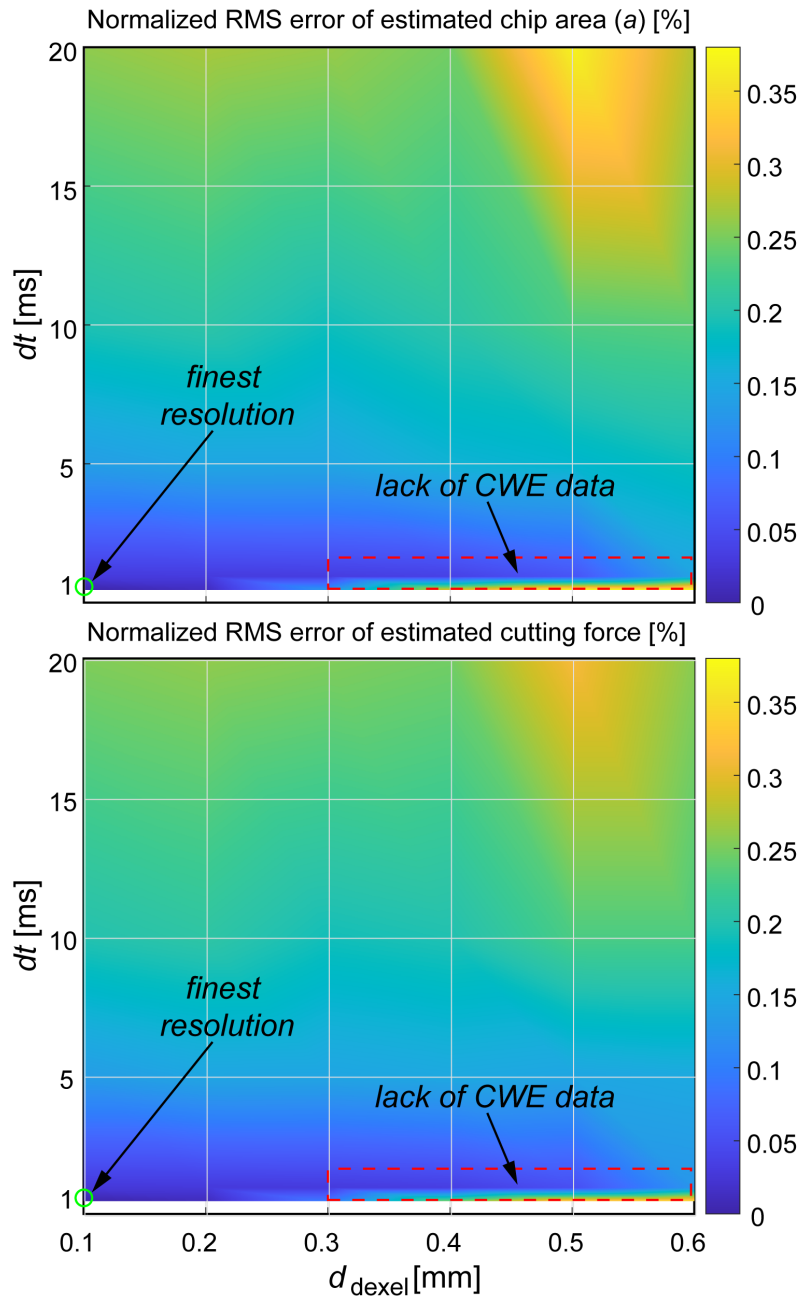
Figure 4.17: Effect of dexel resolution and time step on the chip area and cutting force prediction results

4.10   Conclusion

This chapter presented the extraction of uncut chip geometry and cutting force prediction for hobbing. The 3D uncut chip geometry is extracted during each time step of the simulation using a tri-dexel based geometric modeler, ModuleWorks. A 2D uncut chip cross-section is calculated by intersecting the rake plane of the hob with the 3D uncut chip geometry. After resolving the local cutting conditions and kinematics, the calculated 2D geometry is used in a generalized oblique cutting model to calculate the forces for each individual engaged node on the cutting edge of the hob. Finally, the local cutting forces are summed over the length of the cutting edge to calculate the total cutting force at that time step. The next chapter will discuss the validation of the proposed model through hobbing cutting trials.

Chapter 5

Experimental validation of cutting force predictions

5.1   Introduction

The experimental validation of the developed cutting force model is described in this chapter. Cutting forces during several hobbing operations were measured for model validation. In total, 9 cutting trials were conducted on a Liebherr LC 500 CNC hobbing machine [85]. Cutting force data was recorded during the machining of external spur and helical gears. The measured data was processed to remove any parasitic signals introduced by the measurement setup, such that only the pure cutting signature remained for comparison with the predictions.

The remainder of this chapter is as follows: the experimental setup is introduced in Section 5.2. Section 5.3 explains how the measured data was processed for comparison with the predictions. The calibration of the cutting force coefficients are discussed in Section 5.4, continued by the discussion of the results in Section 5.5.

5.2   Experimental setup

Since the cutter and workpiece are rotating simultaneously and undergo a large number of rotations (B1 and C2 axes in Figure 3.11), the use of a stationary dynamometer to measure force was not practical. To realize the direct measurement of the cutting forces rather than relying on indirect estimation from the feed drive currents, a Kistler 9123C rotary dynamometer was clamped on the worktable using a custom-developed fixture. This fixture provides a precision-ground mating surface to the instrument's conical tool-holder interface and enables the adjustment of the clamping preload as needed. The signal is wirelessly transmitted to the receiver and logged using a personal computer. The experimental setup is shown in Figure 5.1.
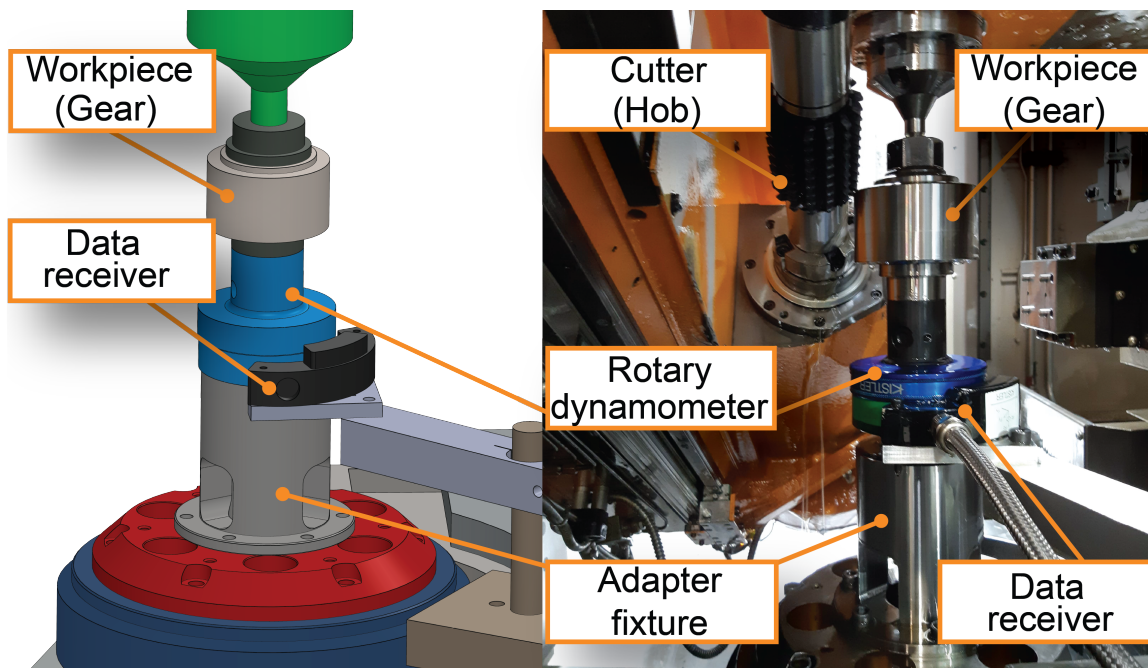
Figure 5.1: Cutting force measurement setup on the Liebherr LC 500 CNC hobbing machine

The cutting trials involved the cutting of five spur gears and four helical gears, with only one hob being used, geometry parameters of which are given in Table 5.1. One of the

spur gears and one of the helical gears were cut using a two-pass process (i.e., finishing and roughing), while the others were cut using a single pass process (i.e, only roughing). The workpiece geometries for both spur and helical gears are shown in Tables 5.2 and 5.3, respectively. The process parameters, including cutting speed, axial feed rate, and depth of cut, are given in Tables 5.4 and 5.5, for spur and helical gear cases, respectively. Two of the machined gears are shown in Figure 5.2.

Table 5.1: Tool geometry data (used in both spur and helical cases)

Parameters	Value
Normal module m_{nc} [mm]	3.175
Number of starts N_c	1
Number of flutes (gashes)	14
Addendum diameter d_{ac} [mm]	75.68
Dedendum diameter d_{dc} [mm]	60.325
Pitch diameter d_{pc} [mm]	68.263
Pressure angle α_{nc} [^{o}]	20.0
Length L_c [mm]	102.0
Rake angle α_r [^{o}]	0.0
Material	ASP 2052

Table 5.2: Workpiece geometry data (used in spur cases)

Parameters	Value
Normal module m_{ng} [mm]	3.175
Number of teeth	30
Addendum diameter d_{ag} [mm]	102.250
Dedendum diameter d_{dg} [mm]	87.316
Helix angle β [^{o}]	0.0
Pressure angle α_{ng} [^{o}]	20.0
Gear width w_g [mm]	56.6
Material	AISI 4320

Table 5.3: Workpiece geometry data (used in helical cases)

Parameters	Value
Normal module m_{ng} [mm]	3.175
Number of teeth	29
Addendum diameter d_{ag} [mm]	102.25
Dedendum diameter d_{dg} [mm]	87.70
Helix angle β [^{o}]	15.0
Pressure angle α_{ng} [^{o}]	20.0
Gear width w_g [mm]	56.6
Material	AISI 4320

Table 5.4: Cutting process for the spur gear trials

Trial number	1	2	3	4	5	5
roughing vs. finishing	rough.	rough.	rough.	rough.	rough.	finish.
v_f [mm/WR]	3.0	1.5	0.75	3.0	3.0	0.75
d_c [mm]	7.143	7.143	7.143	7.143	6.743	0.4
V_c [m/min]	55.0	55.0	55.0	30.0	55.0	55.0
v_r [mm/WR]	NA	NA	NA	NA	NA	0.4

85

Table 5.5: Cutting process for the helical gear trials

Trial number	6	7	8	9	9
roughing vs. finishing	rough.	rough.	rough.	rough.	finish.
v_f [mm/WR]	3.0	1.5	0.75	3.0	0.75
d_c [mm]	7.143	7.143	7.143	6.743	0.4
V_c [m/min]	55.0	55.0	55.0	55.0	55.0
v_r [mm/WR]	NA	NA	NA	NA	0.4

Figure 5.2: Finished workpiece for spur(left) and helical (right) case studies

5.3 Processing the measured cutting forces

5.3.1 Parasitic effect of tailstock axial preload

The dynamometer measures the raw cutting forces in the x, y, and z directions of the rotating WCS. Figure 5.3.a demonstrates the measured cutting forces in three axes. The rotary dynamometer was registering a sinusoidal force signal of ± 40 N in the x and y directions even with no cutting action taking place. It is believed that the primary cause is internal strains within the dynamometer induced by the automated tailstock preload system. This force signal needed to be compensated from the actual machining measurement to only account for pure machining force. The effect was compensated by synchronizing and then subtracting the recorded air-cutting forces from the cutting trial force signals.

5.3.2 Drift compensation

Drift problem is typical in piezo-electric dynamometers. As can be seen, the F_z data is susceptible to drift from its original value over time, which requires compensation. To address this issue, a linear compensation technique is employed. This technique involves selecting two time points during which no engagement occurs, and creating a line that describes the drift between those points. The line is then used to eliminate the drift from the data. Figure 5.3 demonstrates this approach and depicts the elimination of the drift from the original force data.

5.3.3 Structural distortion compensation using Kalman filter

In hobbing, the cutting forces are periodic and occur at tooth passing frequency and its harmonics. While the dynamometer bandwidth is sufficiently high ($\approx$10KHz), the actual bandwidth of the measurement is influenced by the structural resonances below $\approx$1KHz originating from the measurement device assembly. These resonances can amplify the dynamometer measurements in the x-y-z directions of the rotating WCS. To enable a practical
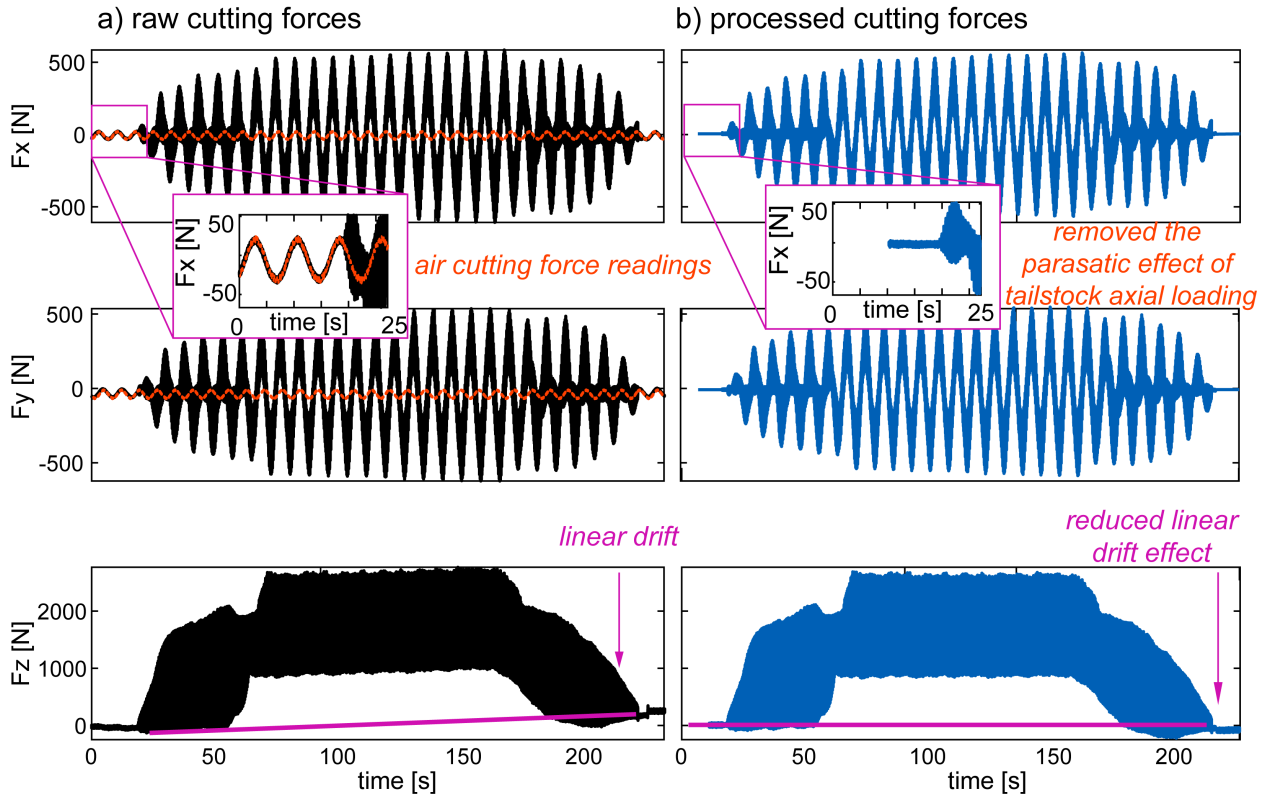
Figure 5.3: Raw and processed force measurements

measurement band above the tooth passing frequency and its harmonics, a Kalman filter is designed based on the technique introduced in [96]. The ultimate goal of the Kalman filter is to reconstruct the actual force (F_a) acting on the gear from distorted dynamometer force measurements, which will contain gain and phase aberration as a function of frequency. The overview of the process can be seen in Figure 5.4.

5.3.3.1 Identification of the measurement distortion FRFs

To identify the measurement distortions, the force input (F_a) to force measurement (F_m) frequency response functions (FRFs) were determined using impact hammer testing, by exciting the workpiece along the x-y-z directions of the MCS, and acquiring the correspond-
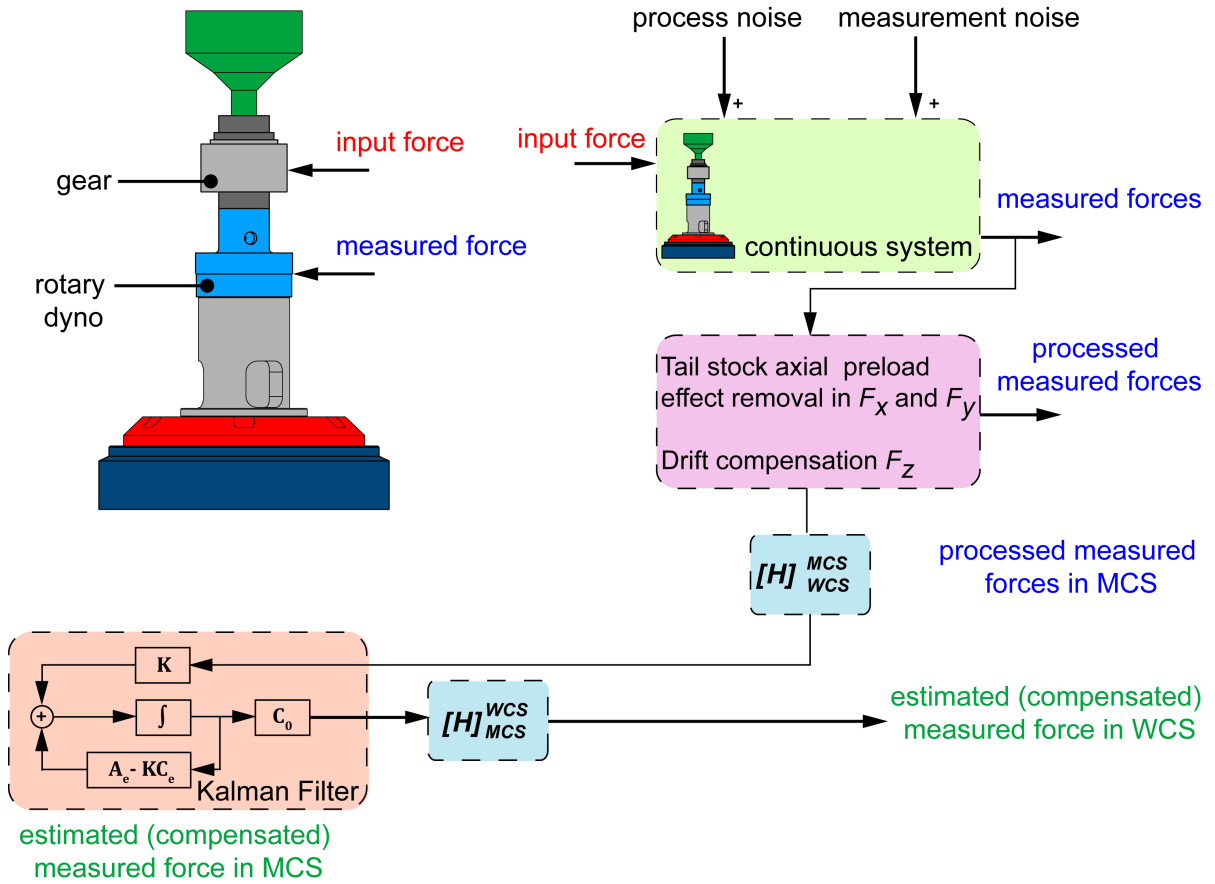
Figure 5.4: Overview of the application of Kalman filter for cutting force distortion compensation

ing dynamometer outputs while the workpiece was stationary (see Figure 5.5.a). The tests were performed in three orthogonal directions when the WCS and MCS axes were aligned. The measured FRFs are identified for all axes by the peak-picking approach [97] in the following transfer function format:

$$\phi(s) = \frac{F_m(s)}{F_a(s)} = \sum_{k=1}^{m_k} \frac{1}{\alpha_k} \frac{\omega_{n,k}^2}{s^2 + 2\zeta_k\omega_{n,k} + \omega_{n,k}^2} \tag{5.1}$$

where k is the mode number and m_k is the total number of modes. α_k, ζ_k, and $\omega_{n,k}$ are the modal contribution factor, damping ratio, and natural frequency for each mode,

89

respectively. The identified modal parameters describing the transfer functions in the x and y directions are given in Table 5.6 and 5.7, respectively.

Table 5.6: Identified modal parameters by fitting the measured FRF in x direction

Mode number (k)	ω_n	ζ	α
1	200	0.023	1.78
2	420	0.381	-0.42
3	495	0.077	-0.44
4	550	0.065	-0.40
5	610	0.079	1.01
6	750	0.024	-0.14
7	875	0.175	-0.40

Table 5.7: Identified modal parameters by fitting the measured FRF in y direction

Mode number (k)	ω_n	ζ	α
1	420	0.063	0.33
2	495	0.051	0.35
3	577	0.030	0.53
4	648	0.039	-0.50
5	820	0.061	0.28

The measured and fitted transfer functions in the x and y directions are provided in Figure 5.5.b. While careful and proper grounding practices were followed during the measurement conducted in the factory environment, unwanted parasitic noise artifacts at frequencies such as 60 Hz and 120 Hz were still present. Despite these challenges, the frequency response functions (FRFs) could still be measured and fitted successfully, as shown in Figure 5.5.b. The z direction was significantly more rigid ($\approx 50\times$), and the cross-sensitivities (e.g., $x - y$, $y - z$) were also observed to be negligible ($\approx 50\times$). It can be seen that the measured and curve-fitted transfer functions are in good agreement. The

resonances are attributing to the bending in the fixture adapter, dynamometer, and the work holding assembly. The transfer function measurements suggest that the dynamometer can effectively measure hobbing forces with harmonics below 100 Hz which is within the tooth passing frequency. However, the higher harmonics of the tooth passing frequency are amplified (for example 7 times around 600 Hz) and require compensation. While the inverse of the transfer function can be used to compensate for the distortions, it can result in the amplification of noise, or worse – an unstable filter if the identified dynamics is non-minimum phase. A Kalman filter is a better alternative as it can reduce noise while accounting for the effects of structural modes on the measured cutting forces.
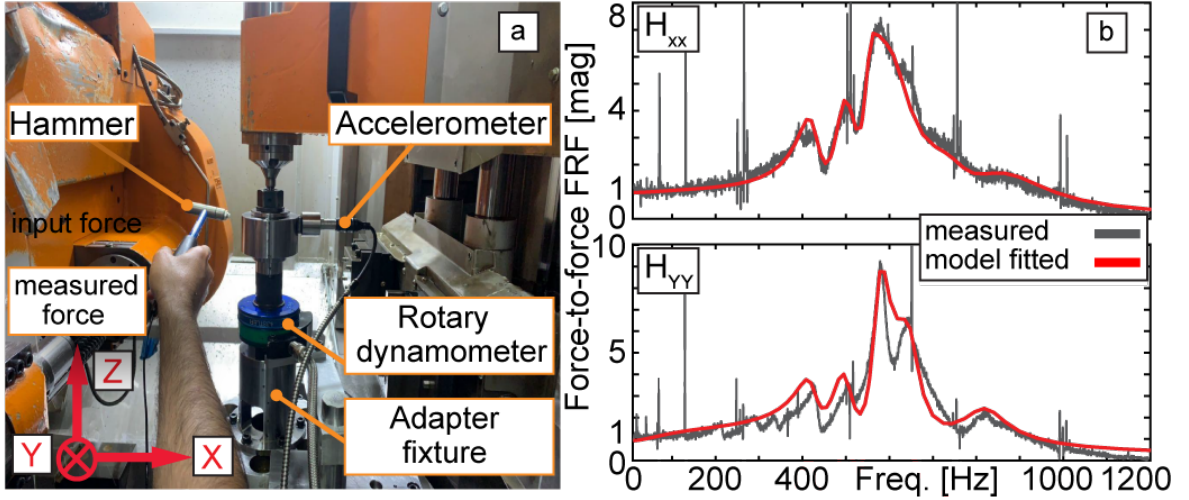

Figure 5.5: a) Measurement of structural distortions affecting cutting force measurement b) measured and fitted FRFs

5.3.3.2   State-space representation of the force measurement dynamics

To represent the dynamic system in the state-space form, equation 5.1 can be rewritten in the polynomial form as follows:

$$\phi(s) = \frac{F_m(s)}{F_a(s)} = \frac{b_1 s^{2m_k-2} + b_2 s^{2m_k-3} + ... + b_{2m_k-1}}{s^{2m_k} + a_1 s^{2m_k-1} + ... + a_{2m_k-1}s + a_{2m_k}} \tag{5.2}$$

91

While higher order dynamics for the numerator could have been chosen, the order is chosen to be -2 from denominator as shown in [96]. The polynomial coefficients for each axis are calculated from the modal parameters reported in Tables 5.6 and 5.7. The transfer function given in equations 5.1 and 5.2 is transformed into the state-space form:

$$\dot{\boldsymbol{x}}(t) = \boldsymbol{A}\boldsymbol{x}(t) + \boldsymbol{B}F_a(t)$$
$$F_m(t) = \boldsymbol{C}\boldsymbol{x}(t)$$

(5.3)

The representation above, involves a state vector $\boldsymbol{x}(t)$ and the measured output force $F_m(t)$, with the actual applied force being denoted as $F_a(t)$. The state space model in the continuous time domain includes the normalized state $\boldsymbol{A}$, the input $\boldsymbol{B}$, and the output $\boldsymbol{C}$. The input transmission $\boldsymbol{D}$ matrix is zero. The representation of the disturbance transfer function in the x direction, which is approximated using seven modes, is depicted below in state-space form.

$$\begin{bmatrix} \dot{x}_1 \\ \dot{x}_2 \\ \vdots \\ \dot{x}_{14} \end{bmatrix} = \underbrace{\begin{bmatrix} -a_1 & -a_2 & -a_3 & \cdots & -a_{14} \\ 1 & 0 & 0 & \cdots & 0 \\ 0 & 1 & 0 & \cdots & 0 \\ \vdots & \vdots & \ddots & \vdots \\ 0 & 0 & \cdots & 1 & 0 \end{bmatrix}}_{\boldsymbol{A}_{14\times14}} \begin{bmatrix} x_1 \\ x_2 \\ \vdots \\ x_{14} \end{bmatrix} + \underbrace{\begin{bmatrix} 1 \\ 0 \\ \vdots \\ 0 \end{bmatrix}}_{\boldsymbol{B}_{14\times1}} F_{a,x}$$

(5.4)

$$F_{m,x} = \underbrace{\begin{bmatrix} 0 & b_1 & b_2 & \cdots & b_{13} \end{bmatrix}}_{\boldsymbol{C}_{1\times14}} \begin{bmatrix} x_1 \\ x_2 \\ \vdots \\ x_{14} \end{bmatrix}$$

The state-space form of the disturbance transfer function in the y direction can be derived similarly.

5.3.3.3 State-space representation of the expanded disturbance model

Equation 5.4 can be expanded to include the actual cutting force exerted on the gear, which can be formulated as an unknown state. The cutting force measurement is taken

at a high frequency ($\approx$10 KHz), which is much faster than the tooth passing frequency of 53.66 Hz. Therefore, it is reasonable to assume that the input forces remain constant during the short sampling intervals. The dynamics of the input is then modeled as an integrated white noise process, receiving the input of process noise (w).

$$\dot{F}_a = 0F_a + w \tag{5.5}$$

Thus, the state-space model which contains this 'input' dynamics can now be written, for example for the x-direction, as

$$
\underbrace{\begin{bmatrix} \dot{x}_1 \\ \dot{x}_2 \\ \vdots \\ \dot{x}_{14} \\ \dot{F}_{a,x} \end{bmatrix}}_{\dot{x}_e \, 15 \times 1} = \underbrace{\begin{bmatrix} -a_1 & -a_2 & -a_3 & \cdots & -a_{14} & b_1 \\ 1 & 0 & 0 & \cdots & 0 & 0 \\ 0 & 1 & 0 & \cdots & 0 & 0 \\ \vdots & \vdots & \vdots & \ddots & \vdots & \vdots \\ 0 & 0 & 0 & \cdots & 0 & 0 \end{bmatrix}}_{A_e \, 15 \times 15} \begin{bmatrix} x_1 \\ x_2 \\ \vdots \\ x_{14} \\ F_{a,x} \end{bmatrix} + \underbrace{\begin{bmatrix} 0 \\ 0 \\ \vdots \\ 0 \\ 1 \end{bmatrix}}_{\Gamma \, 15 \times 1} w \tag{5.6}
$$

$$
F_{m,x} = \underbrace{\begin{bmatrix} 0 & b_1 & b_2 & \cdots & b_{13} & 0 \end{bmatrix}}_{C_e \, 1 \times 15} \begin{bmatrix} x_1 \\ x_2 \\ \vdots \\ x_{14} \\ F_a \end{bmatrix} + v
$$

The Kalman Filter estimates the 'expanded' state vector (x_e), taking into account the system model and known distribution of the measurement noise (v):

$$
\begin{aligned}
\dot{\hat{x}}_e &= A_e\hat{x}_e + K(F_m - \hat{F}_a) \\
&= A_e\hat{x}_e + K(F_m - C_e\hat{x}_e) \\
&= (A_e - KC_e)\hat{x}_e + Kz \\
\hat{F}_a &= C_0\hat{x}_e
\end{aligned} \tag{5.7}
$$

Aboce, $C_0 = \begin{bmatrix} 0 & 0 & \cdots & 0 & 1 \end{bmatrix}_{1 \times 15}$ and K is the Kalman gain. In equation 5.7 the actual cutting force (F_a) is estimated as $\hat{F}_a$. The Kalman Filter's transfer function can be obtained

93

by using the state space representation presented in 5.7 as:

$$\phi_k(s) = \frac{\hat{F}_a(s)}{F_m(s)} = \left\{ \frac{C_0 \text{adj}[sI - (A_e - KC_e)]}{\det[sI - (A_e - KC_e)]} \right\} K \tag{5.8}$$

To determine the Kalman Filter gain, the state estimation error covariance ($P = E[\tilde{x}\tilde{x}^T]$) is minimized using the actual and estimated models. The estimated error ($\tilde{x}$) is defined as the difference between the estimated state ($\hat{x}e$) and the actual state (xe). The resulting Kalman gain is obtained from this process:

$$K = PC_e^T R^{-1} \tag{5.9}$$

The covariance matrix for the state estimation error is calculated using the Riccati equation [98], as shown below:

$$\dot{P} = A_e P + P A_e^T - P C_e^T C_e P^T R^{-T} + \Gamma Q \Gamma^T \tag{5.10}$$

The covariances of the process noise ($Q = cov(w)$) and sensor noise ($R = cov(v)$) were determined as $Q = 10^9$ and $R = 10.5$, respectively. The covariance matrix for measurement noise (R) is determined by the difference between dynamometer readings when the machine is stationary and when air cutting is performed, in order to determine how much signal contamination is caused by the hobbing machine's feed drives. On the other hand, the system noise covariance matrix (Q) was adjusted to improve the compensation by trial and error.

The Kalman gains in the x and y directions were found to be:

$$K_x = [-1.2128 \quad 21.934 \quad 35.305 \quad -56.478 \quad -103.668$$
$$8.723 \quad 115.680 \quad 48.558 \quad -99.925 \quad -51.201$$
$$13.643 \quad 16.037 \quad -1.578 \quad -4.020 \quad -31.623] \times 10^4$$

$$K_y = [-0.600 \quad 0.103 \quad 2.167 \quad 0.152$$
$$-1.918 \quad -0.499 \quad 0.791 \quad 0.362$$
$$-0.312 \quad -0.107 \quad -10.00 \quad] \times 10^4$$

The Kalman filter's transfer function is converted into discrete-time domain using the Tustin's dicretization method, which is represented by the equation $2(z-1)/T_s(z+1)$. This conversion is done at every sampling time interval of $T_s = 9.7656 \times 10^{-5}$ seconds when the cutting force (F_m) is measured. The actual forces (F_a) acting on the gear can be reconstructed by applying the discrete-time version of the Kalman transfer function, as described in equation 5.8, to the measured and processed forces from the rotary dynamometer.

The effectiveness of the Kalman filter in compensating for transmission aberrations due to structural dynamics can be verified by checking whether the the product of the Kalman filter and mechanical transmission transfer functions approaches 1 (one) over a broad frequency range.

$$\phi_{KF}(s) \times \phi(s) = \frac{\hat{F}_a(s)}{F_m(s)} \times \frac{F_m(s)}{F_a(s)} \approx 1 \tag{5.11}$$

The structural measurement, modal fitting results, and the designed Kalman filter's compensation characteristics are shown in Figure 5.6. The Kalman filter enables a practical measurement band up to 450 Hz while correcting for most of the distortions caused by the resonances. This is around 8.3× that of the highest tooth passing frequency (53.66 Hz) used in the experiments.

Figure 5.7 shows the measured cutting forces after applying the developed signal conditioning and Kalman filter in the x and y directions of the WCS. As can be seen, the Kalman filter effectively reduces high-frequency signal content and retains the overall pattern of the forces resulting occurring at the tooth passing frequency and its few higher harmonics, as evidenced from the successful reconstruction of the general force waveforms. By truncating the modes, the assumptions regarding the unbiased estimate of the Kalman Filter (KF) is expected to be preserved, as the roll-over (i.e., attenuation) and limited bandwidth of the KF helps mitigate errors caused by unmodeled higher frequency modes.
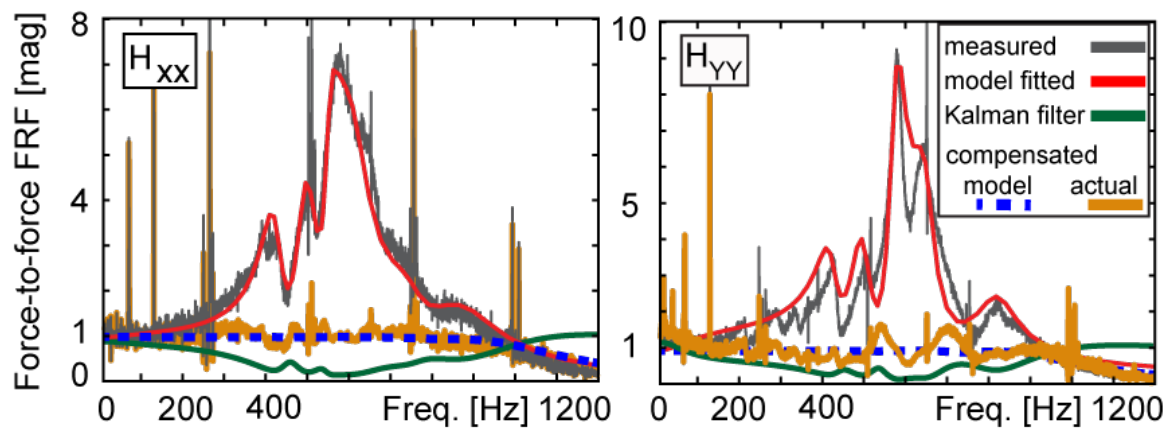
Figure 5.6: Developed Kalman filter and disturbance compensated FRFs in x and y directions
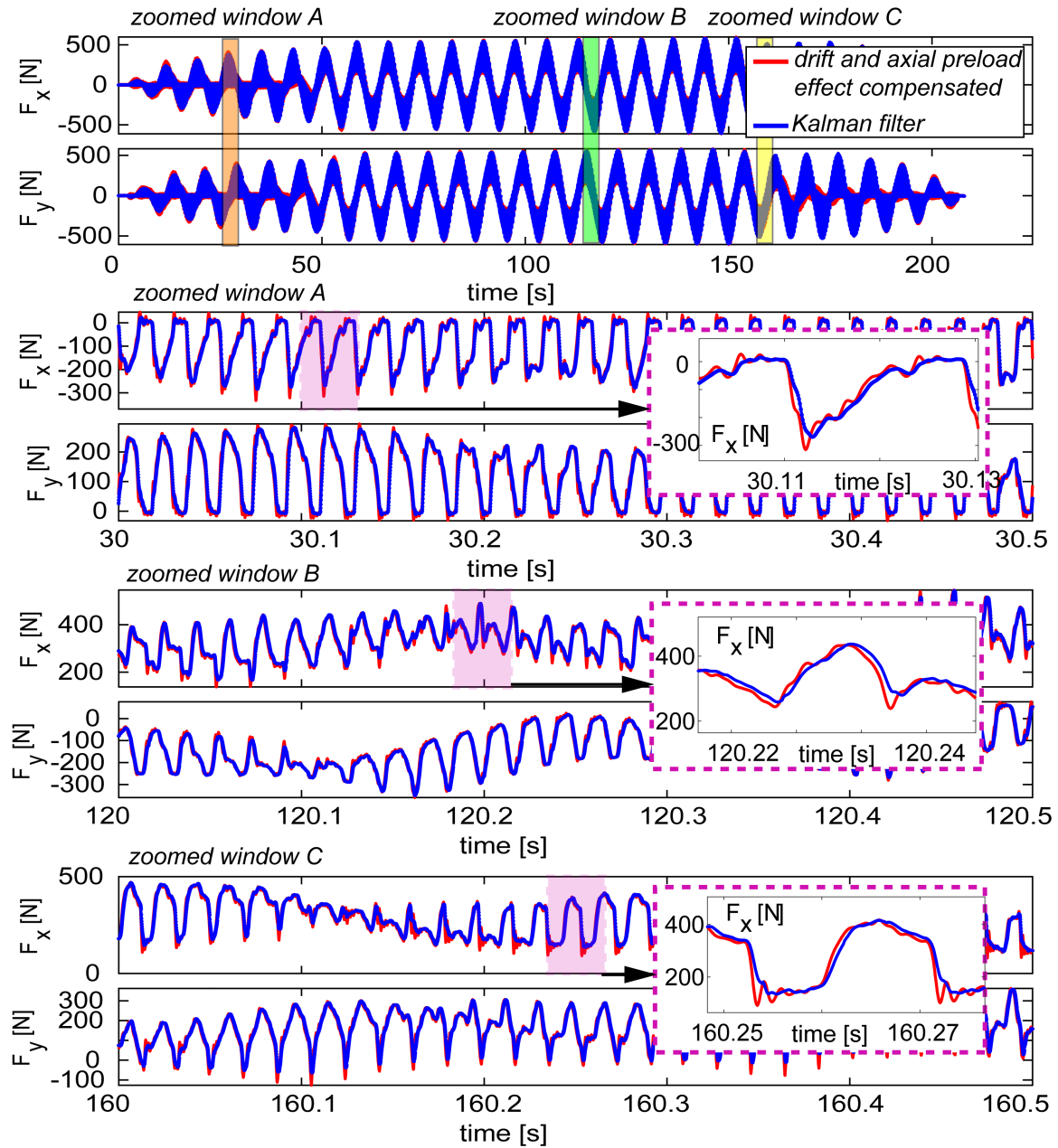
Figure 5.7: Kalman filtered cutting forces in the WCS

5.4 Calibration of cutting force coefficients

To enable the prediction of the hobbing forces using orthogonal and oblique models, a portion of the measured force data from Trial 1 (20-40 s and 80-100 s) was selected to calibrate the cutting force coefficients, which was then used to simulate the machining operation for the entire process (20-220 s).

5.4.1 Orthogonal model

In this model, it is assumed that the cutting velocity is perpendicular to the cutting edge of the hob. Thus, in the simulation, the effect of the axial feed rate and rotational velocity of the gear are excluded from the cutting velocity, and only the rotation of the hob is considered. As a result, the inclination angle is approximated to be zero and the cutting force only comprises of tangential and feed components. Furthermore, as there is no global rake angle on the hob, the local rake angle across the cutting edge is assumed to be zero. The orthogonal cutting force model consists of four parameters: K_{tc}, K_{fc}, K_{te} and K_{fe}, i.e., the tangential and feed direction cutting and edge force coefficients. The zero rake and inclination angle also implies that the cutting and edge force coefficients are the same at all point of contact along the cutting edges. To solve for the parameters, the measured forces and simulated chip characteristics were used to formulate a least-squares problem via linear regression. The data is collected from every sampled point during the process, and the problem is formulated as follows:

$$
\underbrace{\begin{bmatrix} \begin{bmatrix} F_x \\ F_y \\ F_z \end{bmatrix}_{i=1} \\ \vdots \\ \begin{bmatrix} F_x \\ F_y \\ F_z \end{bmatrix}_{i=S} \end{bmatrix}}_{\text{measured forces}} = \underbrace{\begin{bmatrix} \begin{bmatrix} \sum_{n=1}^{nodes} a\boldsymbol{t} & \sum_{n=1}^{nodes} a\boldsymbol{f} & \sum_{n=1}^{nodes} b\boldsymbol{t} & \sum_{n=1}^{nodes} b\boldsymbol{f} \end{bmatrix}_{i=1} \\ \vdots \\ \begin{bmatrix} \sum_{n=1}^{nodes} a\boldsymbol{t} & \sum_{n=1}^{nodes} a\boldsymbol{f} & \sum_{n=1}^{nodes} b\boldsymbol{t} & \sum_{n=1}^{nodes} b\boldsymbol{f} \end{bmatrix}_{i=S} \end{bmatrix}}_{\text{regressors (from simulations)}} \underbrace{\begin{bmatrix} K_{tc} \\ K_{fc} \\ K_{te} \\ K_{fe} \end{bmatrix}}_{\text{cutting coefficients}} \quad (5.12)
$$

Above, i is the sample point number, and S is the total number of samples used in the calibration (i.e., 20-40 s, 80-100 s). $\boldsymbol{t}$ and $\boldsymbol{f}$ are tangential and feed direction unit vectors that are calculated for each engaged node along the cutting edge of the hob. a and b are the chip area and chip width associated with each engaged node. The least-squares problem can be written as:

$$
Y = \begin{bmatrix} \phi_c & \phi_e \end{bmatrix} \begin{bmatrix} \theta_c \\ \theta_e \end{bmatrix} \quad (5.13)
$$

Y is a $3S \times 1$ vector of measured forces, ϕ_c is a $3S \times 2$ matrix of regressors for cutting coefficients, ϕ_e a $3S \times 2$ matrix of regressors for edge coefficients, θ_c and θ_e are vectors of cutting force and edge force coefficients, respectively. The cutting coefficients are obtained by solving the least-square problem shown in equation 5.13. The calibrated parameters obtained from the experimental data are shown in table 5.8.

Table 5.8: Calibrated parameters of the orthogonal model

parameter	calibrated value	
K_{tc}	2466.8	[MPa]
K_{fc}	891.0	[MPa]
K_{te}	25.0	[N/mm]
K_{fe}	30.4	[N/mm]

5.4.2 Oblique model

5.4.2.1 Orthogonal to oblique cutting force coefficient transformation

In hobbing, the cutting velocity is not actually perpendicular to the cutting edge, thus, it is expected that the oblique model will demonstrate better performance (compared to the orthogonal model) in predicting the cutting forces. The oblique model has six parameters: cutting force coefficients (K_{tc}, K_{fc} and K_{rc}), and edge force coefficients (K_{te}, K_{fe} and K_{re}). The cutting force coefficients are determined through orthogonal-to-oblique transformations (equations 4.6, 4.7 and 4.8) based on shear stress (τ_s), shear angle (ϕ_n), friction angle (β_n), and average rake and inclination angles. The process of estimating shear stress, shear angle, and friction angle from experimental data involves defining a 3D search space and selecting candidate points from that space. The cutting coefficients are then determined through the use of the average local inclination and rake angle via the orthogonal-to-oblique transformation. As with the previous section, a least-squares problem is formulated by utilizing the experimentally measured forces and simulated chip characteristics to solve for the edge coefficients through linear regression. The model prediction error for each candidate is evaluated, and the set with the lowest error is chosen. The least squares problem is formulated as follows:

$$
\underbrace{\begin{bmatrix} \begin{bmatrix} F_x \\ F_y \\ F_z \end{bmatrix}_{i=1} \\ \vdots \\ \begin{bmatrix} F_x \\ F_y \\ F_z \end{bmatrix}_{i=S} \end{bmatrix}}_{\text{measured forces}} = \underbrace{\begin{bmatrix} \begin{bmatrix} \sum\limits_{n=1}^{nodes} a\hat{\boldsymbol{t}} & \sum\limits_{n=1}^{nodes} a\hat{\boldsymbol{f}} & \sum\limits_{n=1}^{nodes} a\hat{\boldsymbol{r}} & \sum\limits_{n=1}^{nodes} b\hat{\boldsymbol{t}} & \sum\limits_{n=1}^{nodes} b\hat{\boldsymbol{f}} & \sum\limits_{n=1}^{nodes} b\hat{\boldsymbol{r}} \end{bmatrix}_{i=1} \\ \vdots \\ \begin{bmatrix} \sum\limits_{n=1}^{nodes} a\hat{\boldsymbol{t}} & \sum\limits_{n=1}^{nodes} a\hat{\boldsymbol{f}} & \sum\limits_{n=1}^{nodes} a\hat{\boldsymbol{r}} & \sum\limits_{n=1}^{nodes} b\hat{\boldsymbol{t}} & \sum\limits_{n=1}^{nodes} b\hat{\boldsymbol{f}} & \sum\limits_{n=1}^{nodes} b\hat{\boldsymbol{r}} \end{bmatrix}_{i=S} \end{bmatrix}}_{\text{regressors (from simulations)}}
$$

$$
\underbrace{\begin{bmatrix} K_{tc} \\ K_{fc} \\ K_{rc} \\ K_{te} \\ K_{fe} \\ K_{re} \end{bmatrix}}_{\text{cutting coefficients}} \tag{5.14}
$$

Similar to equation 5.12, i is the sample point number, and S is the total number of samples used in the calibration (i.e., 20-40 s, 80-100 s). $\boldsymbol{t}$, $\boldsymbol{f}$ and $\boldsymbol{r}$ are tangential, feed, and radial direction unit vectors that are calculated for each engaged node along the cutting edge of the hob. a and b are the chip area and chip width associated with each engaged node. The least-square problem can be written as:

$$
Y = \begin{bmatrix} \phi_c & \phi_e \end{bmatrix} \begin{bmatrix} \theta_c \\ \theta_e \end{bmatrix} \tag{5.15}
$$

Above, Y is a $3S \times 1$ vector of measured forces, ϕ_c is a $3S \times 3$ matrix of regressors for cutting coefficients, ϕ_e a $3S \times 3$ matrix of regressors for edge force coefficients, θ_c and θ_e are vectors of cutting force and edge force coefficients, respectively. The cutting coefficients are found by applying the orthogonal-to-oblique transformation on candidate points within a pre-defined cubic search space of shear stress (400-1000 MPa), shear angle (10-50°), and

friction angle (10-50°). Then, linear regression is used to determine the edge coefficients:

$$\theta_e = \text{pinv}\phi_e(Y - \phi_c\theta_c) \tag{5.16}$$

Here, the radial edge coefficient is usually considered negligible ($K_{re} \approx 0$), so the third column of ϕ_e is set to zero. The model prediction error for each set of coefficients is evaluated using the root-mean-square (RMS) error of normalized forces as follows:

$$RMS = \sqrt{\frac{1}{3S}\left(\sum_{i=1}^{S}(e_x^2 + e_y^2 + e_z^2)\right)} \tag{5.17}$$

where

$$
\begin{aligned}
e_x &= \frac{F_{x,\text{measured}} - F_{x,\text{simulated}}}{\max(F_{x,\text{measured}})} \\
e_y &= \frac{F_{y,\text{measured}} - F_{y,\text{simulated}}}{\max(F_{y,\text{measured}})} \\
e_z &= \frac{F_{z,\text{measured}} - F_{z,\text{simulated}}}{\max(F_{z,\text{measured}})}
\end{aligned}
\tag{5.18}
$$

Other methods can also be used, such as cross-correlation for comparing the predicted and measured forces, however, for the purpose of this research the RMS was found to be sufficient.

The identified best set of coefficients is shown in table 5.9.

Table 5.9: Calibrated parameters of the oblique model

parameter	calibrated value	
ϕ_n	27.5	[°]
β_n	22.5	[°]
τ_s	668.5	[MPa]
K_{te}	21.5	[N/mm]
K_{fe}	59.5	[N/mm]

Figure 5.8 demonstrates the variation of the total calculated error based on shear angle and friction angle candidate points for the identified shear stress.
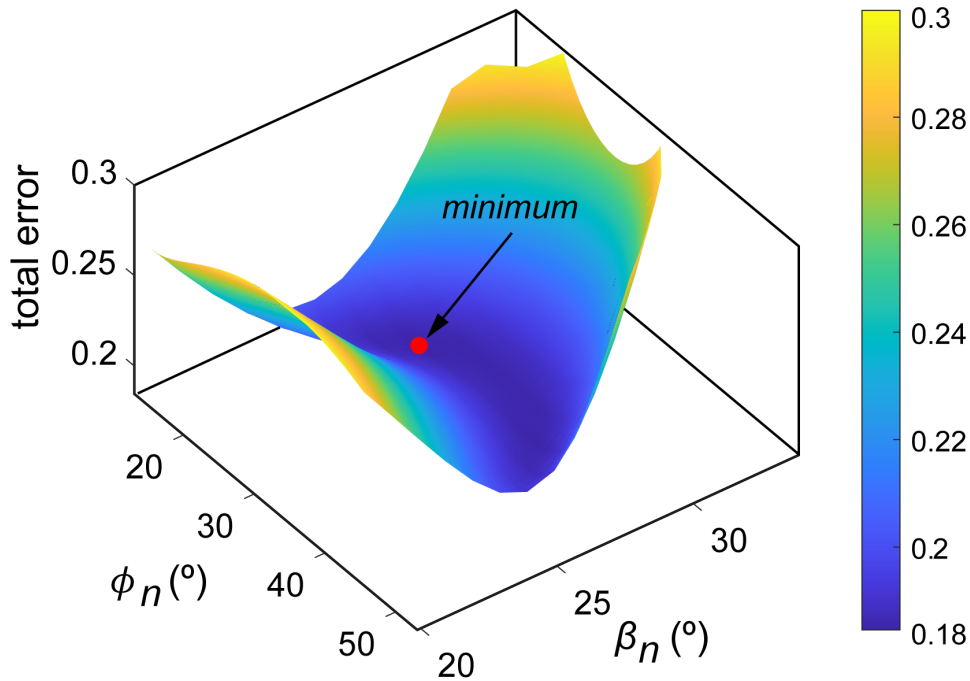
Figure 5.8: Error surface plot for AISI 4320 steel for shear stress τ_s=668.5 MPa

5.4.2.2 Kienzle model cutting force coefficients

Kienzle model parameters were also adopted and identified in setting up the simulations. Similarly, a portion of the experimental data (20-40 s and 80-100 s) of Trial 1 was selected to calibrate the cutting force model's parameter and then used to simulate the entire cutting process (20-220 s). To use the Kienzle model, the local cutting conditions such as force component directions (t, f and r), local rake (α_n) and inclination angles (i), and local chip width (b) and thickness (h) are extracted from the simulation. The Kienzle coefficients (K_u, u, K_v, and v) candidates were populated in a four-dimensional search space. Each

dimension consisted of equally spaced values for each of the Kienzle model's parameters.

$$
\begin{aligned}
K_u &= (200, 225, ..., 975, 1000) \\
u &= (0, 0.05, ..., 0.95, 1) \\
K_v &= (800, 825, ..., 1975, 2000) \\
v &= (0, 0.05, ..., 0.95, 1)
\end{aligned}
\tag{5.19}
$$

The cutting force components acting on each local node j at time step i are calculated as:

$$
\begin{bmatrix} F_x \\ F_y \\ F_z \end{bmatrix}_{j,i} = \begin{bmatrix} \boldsymbol{t}bh & \boldsymbol{f}bh & \boldsymbol{r}bh \end{bmatrix}_{j,i} \begin{bmatrix} K_{tc} \\ K_{fc} \\ K_{rc} \end{bmatrix}_{j,i}
\tag{5.20}
$$

where the cutting coefficients are transformed using equations 4.10, 4.11, and 4.12. The total predicted cutting force at time step i is then computed by summing the local cutting forces contributed by each engaged node:

$$
\boldsymbol{F}_i = \sum_{j=1}^{\text{nodes}} \boldsymbol{F}_{j,i}
\tag{5.21}
$$

As shown for orthogonal to oblique calibration in 5.4.2.1, for every set of candidates, a normalized RMS error is calculated through sample-by-sample subtraction of the simulated forces from their experimental counterparts. The set of coefficients that resulted in the smallest total RMS value is selected as the best candidate. Table 5.10 shows the calibrated parameters for the Kienzle model.

Table 5.10: Calibrated parameters of the Kienzle model

parameter	calibrated value
K_v	1300
v	0.3
K_u	400
u	0.1

5.5 Results and discussions

5.5.1 Accuracy performance of different cutting force models

The accuracy of the calibrated models is assessed by comparing the total root-mean-square error of normalized forces, as shown in Table 5.11. The corresponding time-domain simulation results can be seen in Figure 5.10. Although all three models have comparable accuracy, the Kienzle model is chosen for simulation as it slightly outperforms the others.

Table 5.11: Prediction accuracy of different cutting force models

	F_x[N]	F_y[N]	F_z[N]	total error (%)
Orthogonal model	100.3 (19.3%)	102.0 (19.6%)	170.5 (7.3%)	(16.5%)
Oblique model*	90.9 (17.5%)	97.2 (18.0%)	170.5 (7.3%)	(15.9%)
Oblique model**	84.2 (16.2%)	86.4 (16.6%)	212.6 (9.1%)	(15.6%)

*cutting force coefficients are calculated using orthogonal-to-oblique transformations
**cutting force coefficients are calibrated from Kienzle's model

Although simpler, the predictions of the orthogonal model are comparable to those of the oblique model. This is because the assumptions made in the orthogonal model align reasonably with the physics of the hobbing process. In hobbing, the cutting velocity vector is composed of three components: the velocity of the hob and gear due to their angular motions, and the axial feed of the hob. The tangential velocity of the cutting edge originating from the hob's angular motion accounts for 90% of the total cutting velocity,

making the other two components less significant, as assumed in the orthogonal model. This observation is further supported by the small and almost constant values of local inclination and rake angles, as illustrated in Figure 4.12. However, this approximation may not produce reasonable predictions when the other two components in the cutting velocity vector are more significant (e.g., in scenarios with smaller hob RPMs and/or aggressive axial feed rates). Additionally, with non-standard hobs (e.g., twisted or angled rake faces), it is possible to have larger local inclination and rake angle over the length of the cutting edge which reduces the accuracy of the orthogonal model predictions. Thus, while the orthogonal model yields relatively accurate results in the presented cases studies, it is prudent to establish a more general cutting force model that not only offers insight into the physics of the process but also delivers better accuracy in various hobbing scenarios.
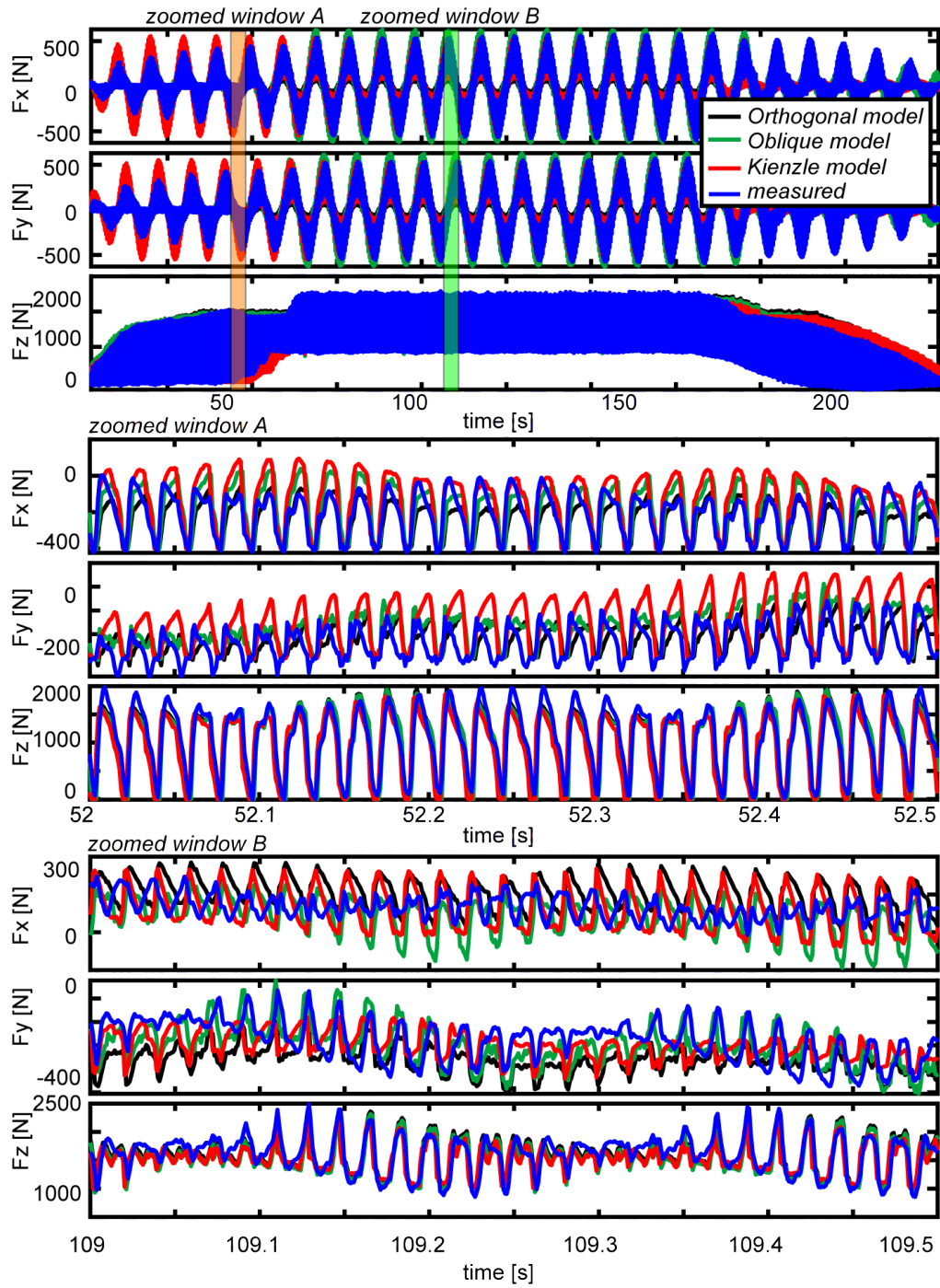
Figure 5.9: Comparison of cutting force models in the WCS [Trial 1]

5.5.2 Spur gear trials

The cutting forces observed in the spur and helical gear trials exhibit a consistent pattern overall with slight variations. As a result, Trial 1 will be analyzed in depth to provide a comprehensive understanding of the forces involved. Figure 5.10 shows the comparison between the prediction and the measured cutting forces for Trial 1, single pass hobbing process of an external spur gear. The forces are displayed for the x, y and z direction of the rotating WCS and zoomed in two distinct windows. The sinusoidal behavior of the measured cutting forces in x and y directions is attributed to the dynamometer rotating with the gear, while the direction of the forces along the z direction remains unchanged.

The observed trend in cutting forces could be explained by breaking the cutting process down into three distinct portions: entry, middle and exit. At entry stage, hobbing process exhibits an intermittent behavior as the cutting edge of the hob enters the blank gear, removes a small volume of the material and exits, resembling an impact force on the gear. During the first engagement of the cutter with the flat face of the gear blank, only the tip of 1-2 adjacent teeth on the engaged flute are involved in the cutting action. The magnitude of the cutting force gradually increases as the hob is moving downward, reaching its full depth of cut. The comparison of the results for this stage reveals that the simulated forces in the z direction, which mainly coincides with the tangential cutting direction, successfully capture the most dominant force component. The forces in lateral x/y axes reflect the influence of the local feed and radial cutting forces. While the simulation captures the the general force envelopes, the influence of tooth passing strokes, and the repetitive nature of the engagement, the maximum forces in each stroke are over-predicted.

As cutting progresses towards the middle of the process, the cutting edge consistently removes material from the blank, creating a steady-state cutting condition where the maximum and minimum forces remain constant. At this stage, depending on the geometry of the hob and gear, there are typically multiple engaged flutes simultaneously with each having 2-3 teeth involved in the cutting process. The generative meshing pattern shown in Figure 5.10 is due to the repetitive teeth engagement. When a tooth on an engaged flute comes into contact with the gear blank, the material is first removed by the leading

flank of the tooth, then by the leading flank and tip, and finally exits with only the trailing flank cutting. This behavior can be used to explain how the chip thickness (and also the cutting forces) start at a low value when the engaged flute first makes contact with the gear, increase to a maximum when the leading flank and tip of the tooth are cutting, and decrease to a minimum when only the trailing flank is cutting (see zoomed window A in Figure 5.10). Similar trend is observed when comparing the simulated and measured force profiles, with prediction in the z direction being the best captured component of the cutting force. Furthermore, the general min/max envelopes and generative meshing pattern in the predicted x/y forces are well-matched with the measurement.

The exit portion resembles the entry portion of the cut. The cutter-workpiece engagement becomes intermittent with less uniform chip engagement distributed over multiple engaged flutes. Similar behavior in the predicted cutting forces is observed.

Of course, the model prediction can be improved especially in the entry portion of the cut where the it has a tendency to over-predict the forces in x/y directions. The reason for over-prediction can be directly linked to the calibrated cutting force coefficients. While the calibrated coefficients produced the lowest total error, there exist another set of coefficients that yields a larger total error, but with a better prediction of the forces in the entry zone and under-prediction in the steady state portion. Thus, if better performance is required, different set of coefficients can be adopted for various cutting zones.

Moreover, it is expected that the accuracy of the prediction improves as the cutter and workpiece are more accurately represented. In the presented results, the hob geometry is generated from the tool manufacturer data. However, the hob had been used in several other trials and may have been worn out or alternatively been re-sharpened or re-grounded, causing its geometry to differ from the manufacturer-provided values. Also, in generating the blank geometry, the actual outer diameter of the blank gear should be employed, rather than the nominal values (i.e., $\pi m_n + d_{ag}$). Since the extracted chip geometry during the trials is quite thin (20-120 μm), even minor inaccuracies in these geometries may result in significant changes in the force predictions. Equally important, the commanded (or actual) axis motion of feed drives may not align with the nominal values derived from the

NC codes because of internal compensations and CNC-specific optimization algorithms that can slightly adjust the nominal values. One such example is temperature compensation, which automatically modifies the center-to-center distance to account for thermal distortions of the machine. Therefore, instead of relying on the developed kinematic model to accurately capture the feed axes motion, the commanded CNC data (or actual CNC data) can be directly input into the virtual model, resulting in improved chip geometry predictions.

Overall, the model performed better in predicting the z forces compared to the other axes. It is hypothesized that, in spite of removing the measurement distortions from the x/y axis, the measured forces still included some additional readings that can be associated with non-cutting sources, possibly originating from the CNC's servo response. Further research and measurement are needed to confirm this hypothesis, which is beyond the scope and of this thesis.

The cutting forces for Trial 3, with a smaller axial feed rate of $v_f = 0.75$ [mm/WR], are shown in Figure 5.11. As expected, the cutting process takes longer and the magnitude of the cutting forces is smaller compared to Trial 1. The behavior of the forces is generally similar to that observed for Trial 1. The accuracy of the prediction, however, is worse as the chips and apparent cutting forces are smaller. The primary cutting models are macro-level and empirical. Therefore, more calibration and data would improve the results. The poor performance in Trial 3 can thus be attributed to the assumption that the calibrated cutting forces are independent of the feed rate values. Nevertheless, a new set of parameters can marginally improve the accuracy of the predictions. Additionally, as the magnitude of the cutting forces are much smaller, the noise and parasitic influences captured by the the measurement device have a more dominant effect, thereby worsening the perceived accuracy of the prediction.
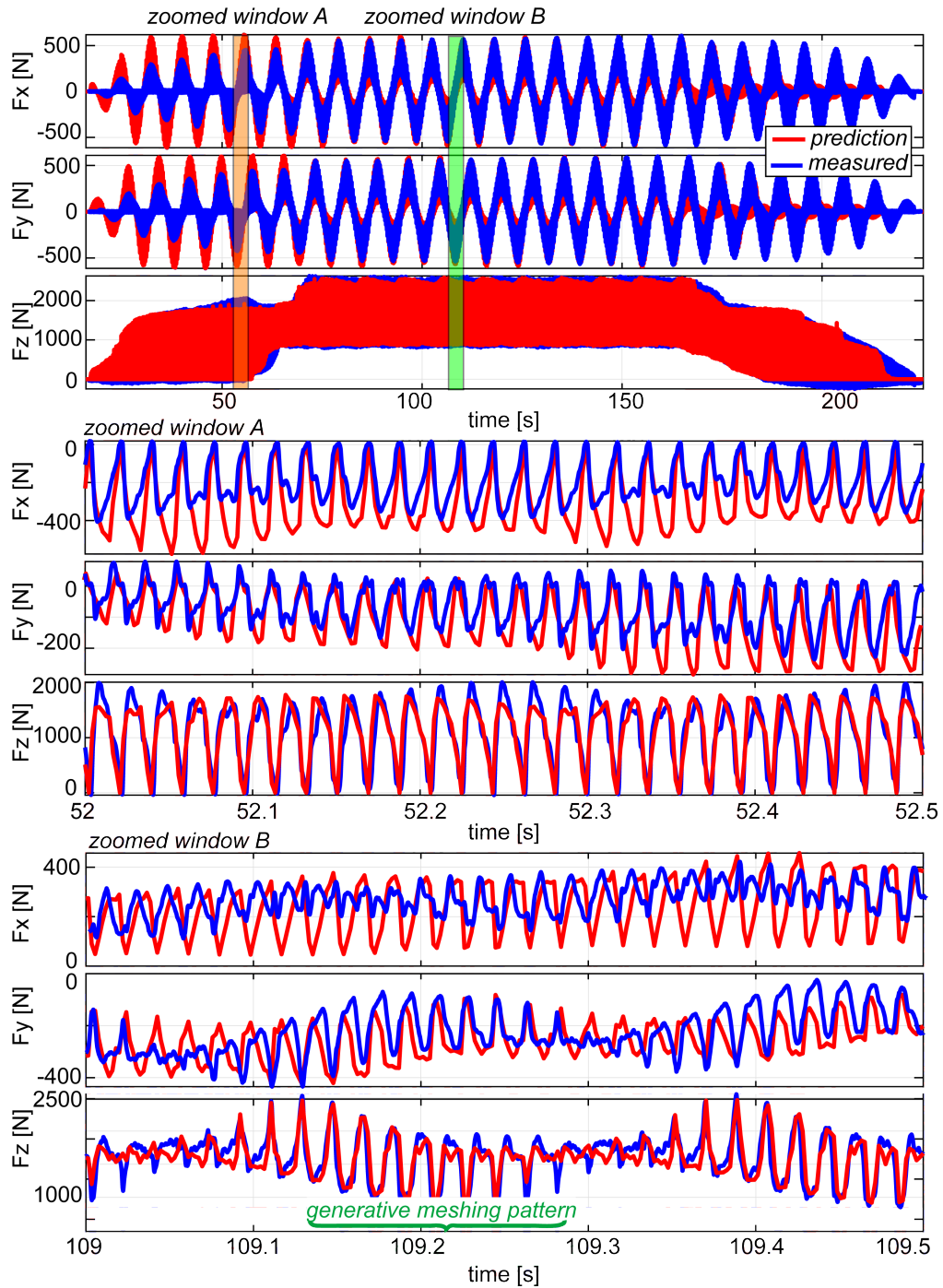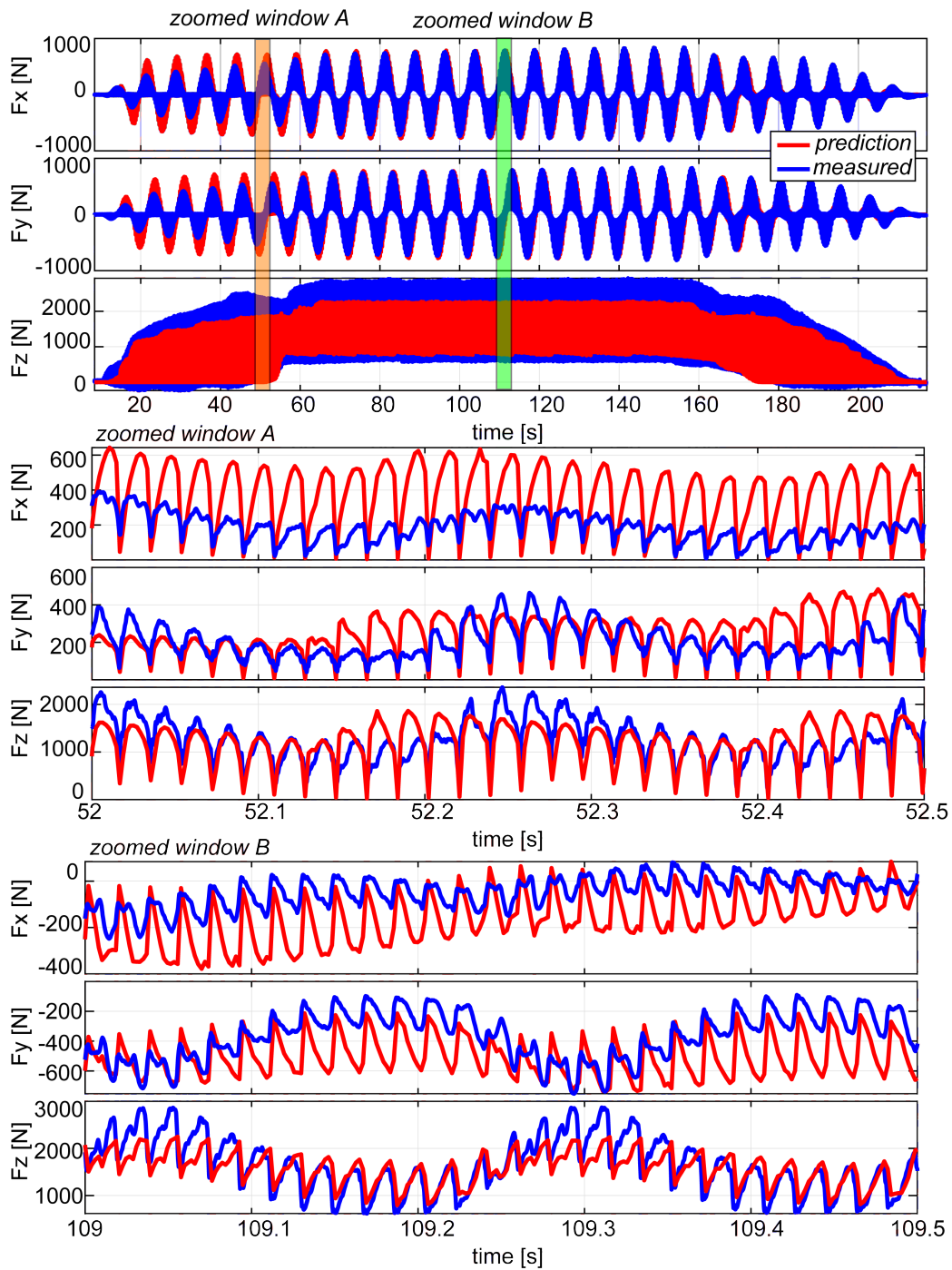
Figure 5.10: Predicted and measured cutting forces in the WCS [Trial 1]
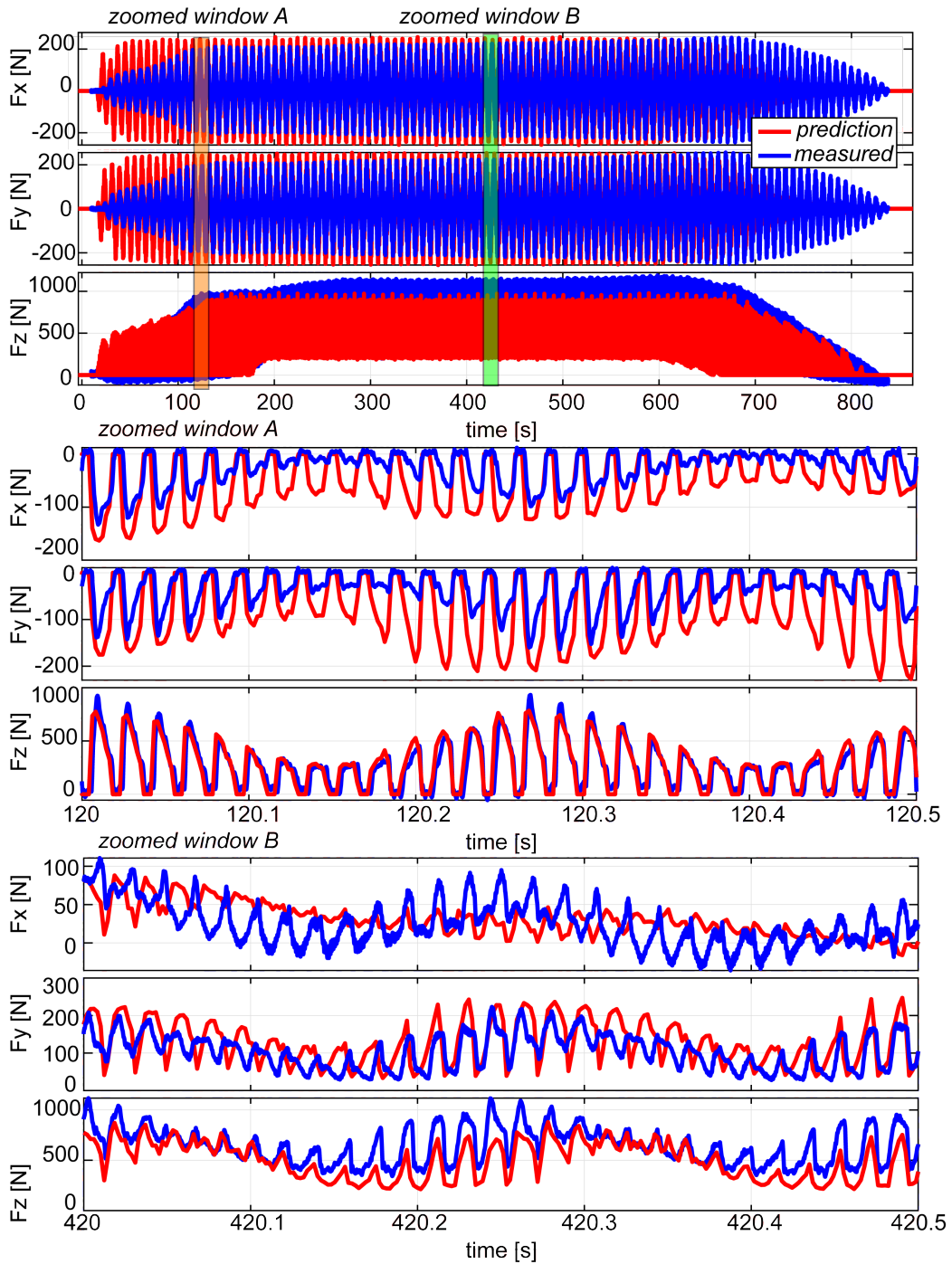
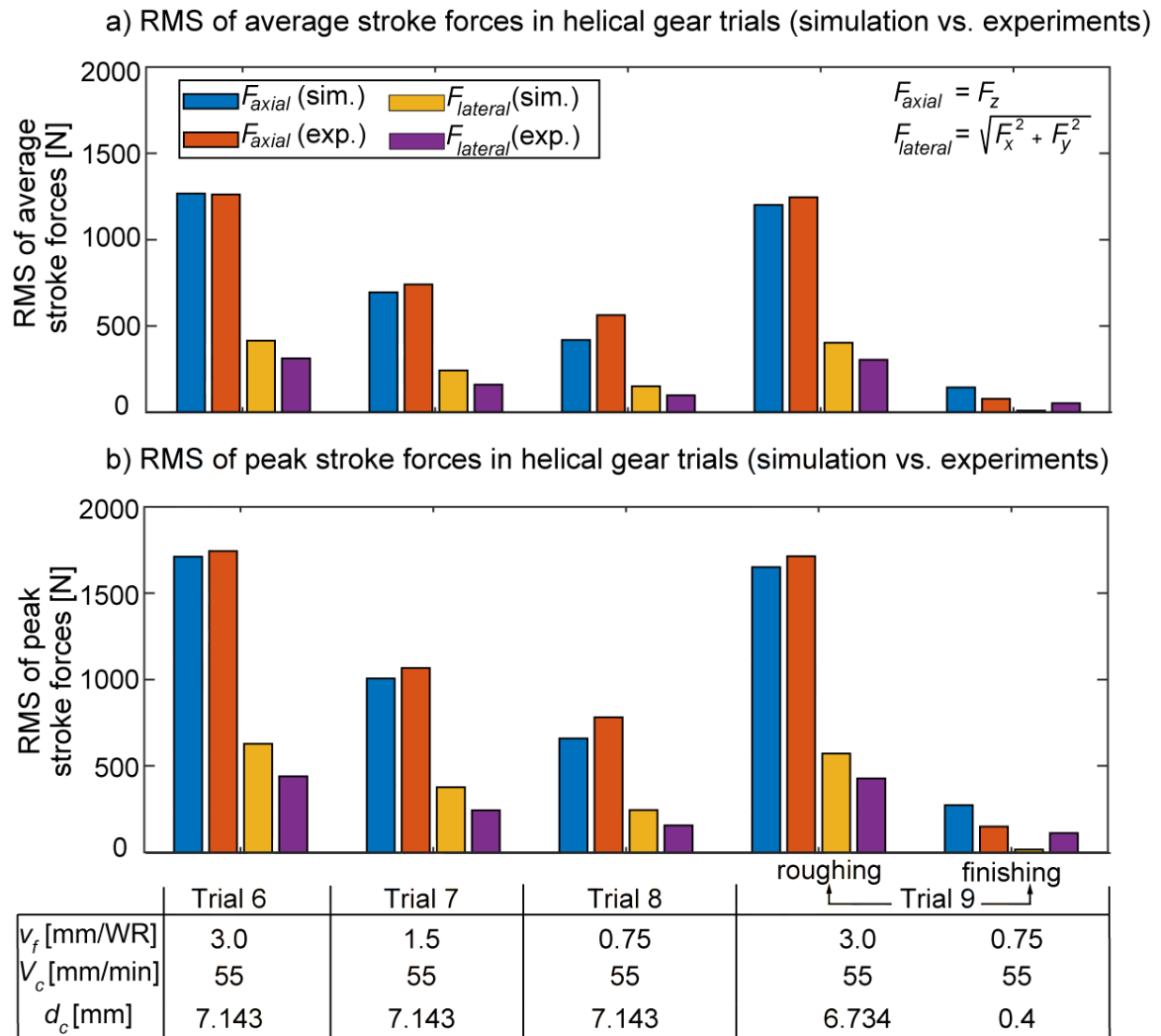Figure 5.11: Predicted and measured cutting forces in the WCS [Trial 3]

The accuracy performance of the prediction for spur gears across the cutting trials is presented in Table 5.12. The RMS values are obtained from sample-by-sample subtraction of every data point throughout the cut as shown in equation 5.17 and 5.18. As indicated, Trial 1 achieved the highest accuracy, which is expected given that the calibration was conducted on 25% of the cutting data specifically for this trial. Moreover, the cutting forces were greater in Trial 1 due to the higher axial feed, resulting in lower levels of noise compared to the force signal magnitudes.

The RMS values of the average and peak stroke forces for both axial ($F_{\text{axial}} = F_z$) and bending ($F_{\text{bending}} = \sqrt{F_x^2 + F_y^2}$) forces are shown in Figure 5.13. To obtain these results, the average and maximum forces were calculated for each hob stroke (i.e., tooth passing period), and their RMS values were calculated over the entire set of strokes (see Figure 5.12).

The results from Trial 1, Trial 2, and Trial 3 demonstrate that the prediction error decreases in different axes with an increase in axial feed rate. Trial 1 and Trial 4 share similar process parameters, except for the cutting velocity. The cutting coefficients are dependent on the cutting velocity, as it is directly related to friction in the process. Therefore, using the same coefficients that were calibrated for $V_c = 55$ [m/min] for a trial performed at a lower cutting velocity of $V_c = 30$ [m/min] would result in under-predicted cutting forces. In fact, the friction and apparent cutting forces observed in Trial 4 are larger than those in Trial 1. This is also supported by the average and peak force prediction demonstrated in Figure 5.13.

For the finishing cut in Trial 5, due to the forces being significantly smaller, the signal-to-noise ratio and apparent prediction accuracy is the worst.

Overall, these results indicate that the model predictions and calibrated coefficients are effective in predicting the general behavior (average, min/max envelopes) of the forces across the cutting trials with varying conditions.

Table 5.12: RMS of prediction error for spur gear cases

	F_x[N]	F_y[N]	F_z[N]
Trial 1	84.2 (16.2%)	86.4 (16.6%)	212.6 (9.1%)
Trial 2	67.1 (17.7%)	68.14 (18.1%)	214.42 (14.2%)
Trial 3	43.2 (19.6%)	43.6 (19.8%)	188.9 (16.7%)
Trial 4	135.6 (19.1%)	137.4 (19.6%)	424.32 (13.6%)
Trial 5 (roughing)	96.2 (16.6%)	92.0 (17.2%)	246.2 (10.3%)
Trial 5 (finishing)	46.58 (29.3%)	36.4 (30.6%)	88.0 (24.1%)
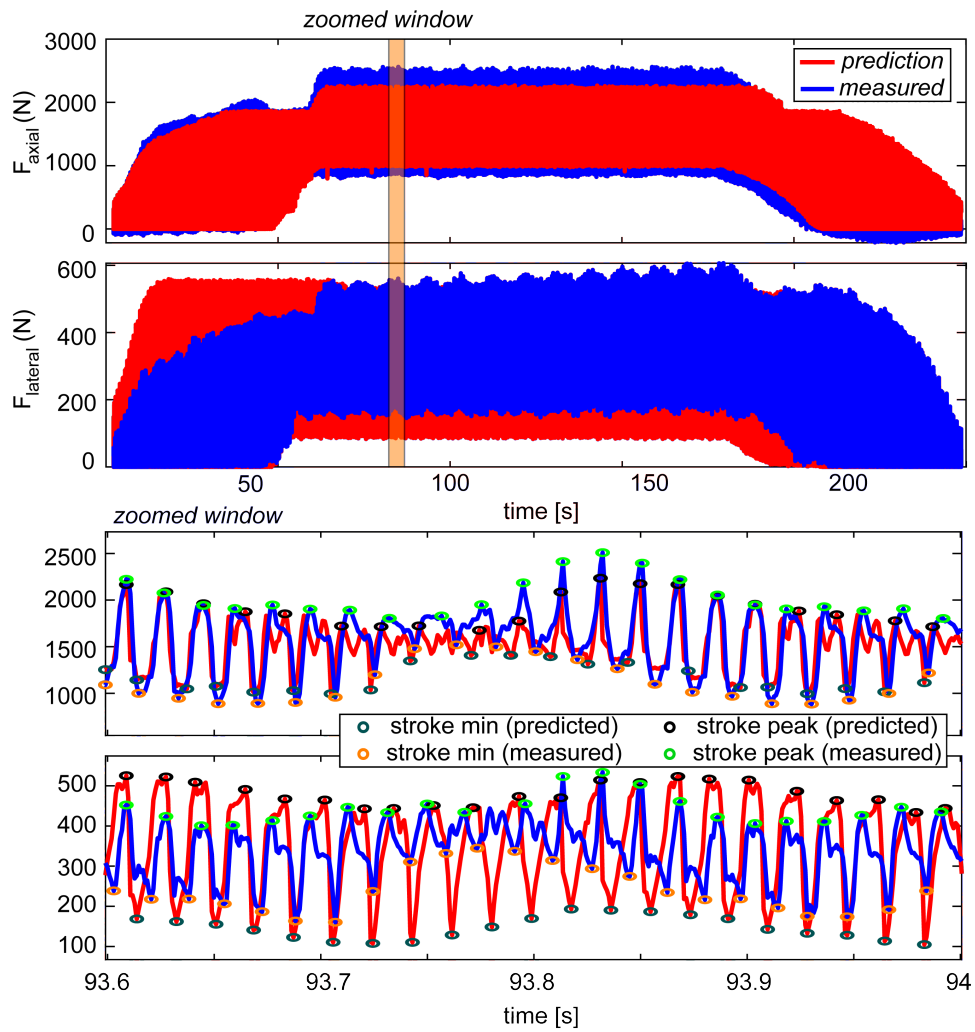
Figure 5.12: Peak and minimum stroke forces

These results indicate that the model predictions and calibrated coefficients are effective in predicting the general behavior (average, min/max envelopes) of the forces across the cutting trials with varying conditions.
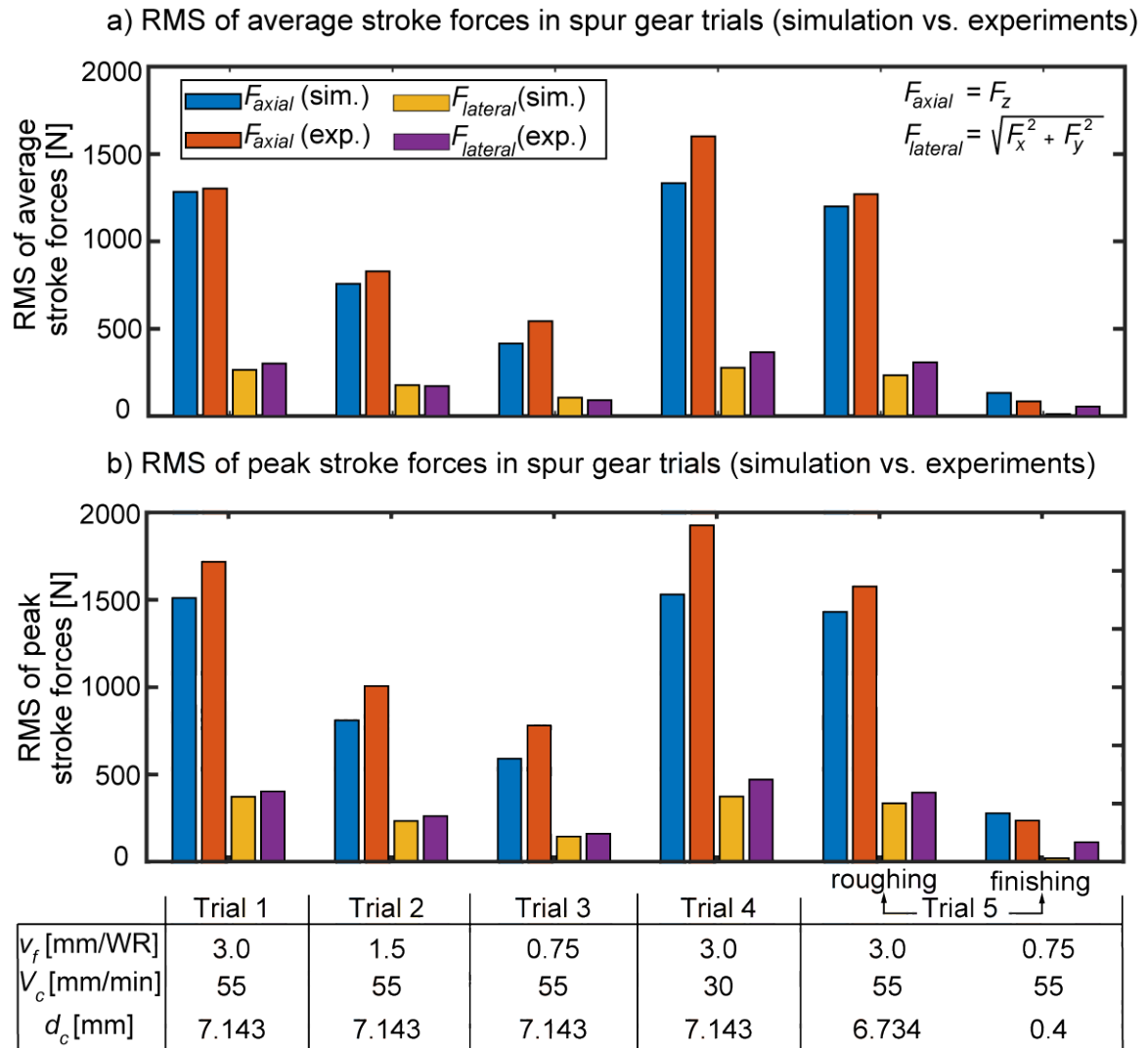
Figure 5.13: RMS of average and peak cutting forces for spur gear trials

5.5.3 Helical gear trials

The force profiles for helical gear cases in Trial 6 and 8 are displayed in Figures 5.14 and 5.15. Generally speaking, the forces have comparable profiles and magnitudes when considered alongside their spur counterparts. Upon closer inspection, the force profiles within each stroke are relatively flatter compared to spur cases. This is due to the fact that the majority of the material is uniformly removed when the engaged flute is in the middle of the stroke, while a minimal amount is removed when entering and exiting a gear gap, resulting in a flatter force profile as opposed to the spur cases.

Moreover, the cutting forces in the x/y directions have a slightly greater magnitude, whereas the z component of the cutting force is reduced in comparison to spur cases. This is because the swiveled hob (i.e., $\gamma=15°$-η) directs more of the tangential forces, which are the most significant force components, to be projected into the x-y plane, causing F_x and F_y to increase but F_z to decrease.

Table 5.13 lists the RMS of prediction errors for the helical cases studies, and similar trend with the spur case studies are observed. Additionally, Figure 5.16 demonstrates the same trend about the RMS of the peak and average stroke forces for the helical trials.

Table 5.13: Summary of prediction errors for helical gear cases

RMS of prediction error	F_x[N]	F_y[N]	F_z[N]
Trial 6	147.3 (17.6%)	148.8 (17.8%)	361.8 (12.1%)
Trial 7	88.9 (18.0%)	88.4 (18.6%)	302.2 (15.9%)
Trial 8	61.4 (18.1%)	64.5 (18.6%)	261.1 (19.2%)
Trial 9 (roughing)	147.0 (17.3%)	154.8(18.1%)	368.8 (13.1%)
Trial 9 (finishing)	84.3 (36.2%)	71.1 (31.6%)	110.9 (24.1%)

Figure 5.14: Predicted and measured cutting forces in the WCS [Trial 6]
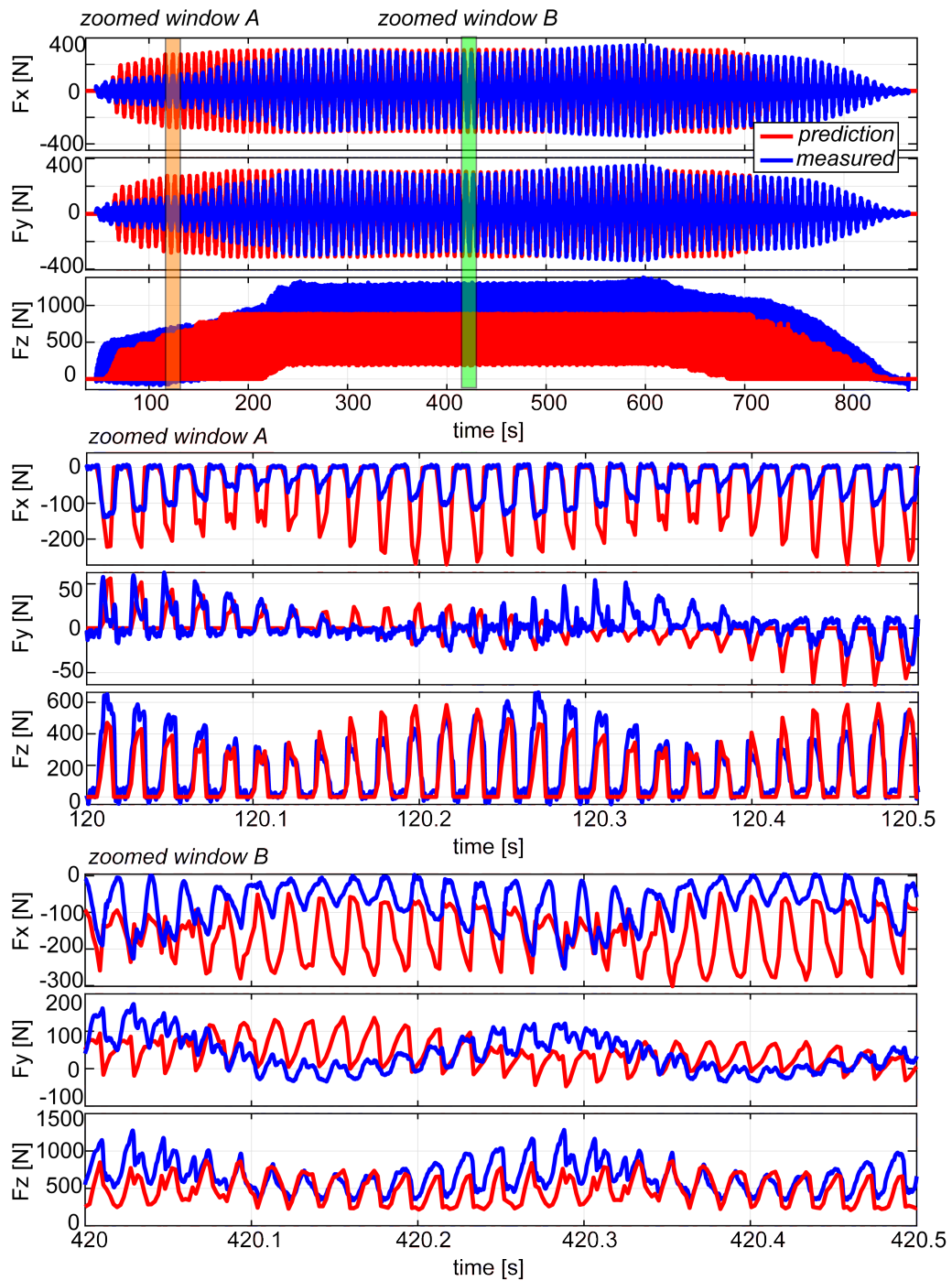
Figure 5.15: Predicted and measured cutting forces in the WCS [Trial 8]

a) RMS of average stroke forces in helical gear trials (simulation vs. experiments)

b) RMS of peak stroke forces in helical gear trials (simulation vs. experiments)

In the legend:
F_{axial} (sim.) $F_{lateral}$(sim.)
F_{axial} (exp.) $F_{lateral}$(exp.)

$$F_{axial} = F_z$$
$$F_{lateral} = \sqrt{F_x^2 + F_y^2}$$

	Trial 6	Trial 7	Trial 8	roughing $\quad$ finishing Trial 9	
v_f [mm/WR]	3.0	1.5	0.75	3.0	0.75
V_c [mm/min]	55	55	55	55	55
d_c [mm]	7.143	7.143	7.143	6.734	0.4

Figure 5.16: RMS of average and peak cutting forces for helical gear trials

120

5.5.4 Limitation of the cutting force models

Cutting force models are simplified representations of the complex cutting process, often assuming linearities and uniformities to facilitate analysis and prediction. However, it is important to recognize that there are a variety of non-linearities in the cutting process (e.g., non-uniform shear zone, complex and non-uniform contact and friction phenomena, thermomechanical behavior of the workpiece material under extremely high strain rates, tool wear, material heterogeneity etc.) that will not be fully captured by the cutting force coefficient identification. These factors can lead to deviations between the predicted cutting forces from the simplified models and the actual forces observed during machining. Therefore, while cutting force models provide valuable insights, it is crucial to consider and account for the potential non-linearities and limitations of these models. Some of the best practices are to parameterize the validity envelope of such models and to refine them with additional experimental data, when conditions allow.

5.6 Conclusion

In this chapter, the proposed cutting force model was validated through hobbing experiments involving the cutting of external spur and helical gears using both single and two-pass processes with varying process parameters. The trials were carried out on a Liebherr LC 500 CNC hobbing machine tool, with cutting forces being measured using a rotary dynamometer mounted via an adapter fixture. To ensure correct comparisons between predicted and measured forces, the measured forces were first processed by removing any distortions that may have arisen from non-cutting influences (e.g., repeating strain cycle due to dynamometer mounting concentricity and alignment, as well as sensor drift). The simulated forces were found to have a reasonable correlation with the measurements, although more discrepancies were observed in the finishing passes, where the signal-to-noise ratio is also smaller. Additional discrepancies in single pass processes are attributed to inaccuracies in the representation of the hob and gear geometries, calibration errors in the cutting force coefficients, CNC feed drive behavior, and the force measurement setup.

Chapter 6

Elastic deformation and gear quality prediction

6.1   Introduction

In the hobbing process, the cutting forces elastically deform the tool and the part assemblies. This deformation leads to inaccuracies in dimensions and leaves excess material on the part, especially when hobbing gear profiles on long and slender shafts, which causes transmission errors, vibrations, and operational noise later during their utilization [99]. To understand and mitigate these effects, the effect of tool and part deflection is studied in this chapter using the virtual gear measurement module of the integrated gear machining simulation and metrology software, previously developed at the University of Waterloo (UW) [75]. It is important to predict and possibly eliminate these sources of profile errors to ensure the quality and reliability of the machined gears.

The chapter begins by discussing the proposed elastic deformation model in Section 6.2 and continues by introducing introducing the virtual gear inspection module of UW's gear machining and metrology suite in Chapter 6.3. The chapter concludes by validating the predicted gear quality with the measured gear profiles in Section 6.4.

6.2 Elastic deformation model

The hob and the workpiece assemblies can be modelled as elastic structures. The static stiffness of the hob (c: cutter) and workpiece (g: gear) are measured in the x, y, and z direction of MCS (i.e., $K_{c,x}$, $K_{c,y}$, $K_{c,z}$, and $K_{g,x}$, $K_{g,y}$, $K_{g,z}$). The rotational stiffness of the components were assumed to be rigid relative to the bending stiffness. The predicted cutting forces from the previous time step are used to calculate the hob and gear deflections and then the deflections which are added to their nominal positions during the current time step.

6.2.1 Static stiffness measurement

The static stiffness values of the cutter and gear sides are approximated by inverting the receptance FRF value at zero frequency. To this end, the accelerance FRF (i.e., acceleration over force) of the hob and gear were identified through impact hammer testing as shown in Figure 6.1. The accelerance for a multi-mode system is defined as:

$$A(\omega) = \frac{\ddot{X}(\omega)}{F(\omega)} = \sum_{m=1}^{m_k} \frac{-K_m \omega^2}{-\omega^2 + 2j\zeta_m \omega_{n,m} \omega + \omega_{n,m}^2} \tag{6.1}$$

Above, m_k is the number of vibration modes, $\omega_{n,m}$ and ζ_m are the mode's natural frequency and damping ratio, respectively. K_m is the mode's contribution factor and is defined as:

$$K_m = \frac{\omega_{n,m}}{k_m} \tag{6.2}$$

where k_m is the modal stiffness. The accelerance FRF can be also written as receptance FRF (i.e., displacement over force) as follows:

$$R(\omega) = \frac{X(\omega)}{F(\omega)} = \frac{A(\omega)}{-\omega^2} = \sum_{m=1}^{m_k} \frac{\dfrac{\omega_{n,m}^2}{k_m}}{-\omega^2 + 2j\zeta_m \omega_{n,m} \omega + \omega_{n,m}^2} \tag{6.3}$$

123

The overall static stiffness of the system $K_{w,d}$ is approximated as:

$$K_{w,d} = \frac{1}{R(0)} = \frac{1}{\sum\limits_{m=1}^{m_k} \frac{1}{k_m}} \tag{6.4}$$

Above, w is c or g (representing the cutter or gear), and d is x, y, or z (representing the mechanical response direction). In this chapter, gears produced on two different experimental setups were considered to assess the accuracy of the developed elastic deformation model. While the first setup was also used to validate the cutting force model in Chapter 5, the second setup was only used in this chapter.

6.2.1.1 Setup I: Spur and helical gear case studies

The experimental setup used for the validation of cutting force prediction in the previous chapter is considered in this case. Specifically, the cutting trials involving one spur gear and one helical gear (Trial 1 and 6) are considered in this assessment. The process and geometry parameters for these trials were previously reported in Tables 5.1, 5.2, 5.3, 5.4, and 5.5. To estimate the static stiffness, the accelerance FRF of the workpiece and tool were measured in the machine's x, y and z directions. For the workpiece measurement, the hammer excitation and acceleration measurement were conducted at the top of the gear where cutting action takes place (see Figure 6.1.b). It was observed that moving the actuation and sensor points on the workpiece has negligible effect on the resulting FRF, implying the rigidity of the workpiece. After converting the accelerance to receptance (as shown in equation 6.3), several modes were fit to the experimentally measured FRFs using peak-picking technique. The estimated modal parameters are shown in Table 6.1. The measured and fitted model receptance FRF for the workpiece in the x and y directions of MCS are also shown in Figure 6.2. The part's z direction and the cross FRFs (e.g., x-y, y-z) were observed to be at least $8\times$ more rigid, and thus ignored.

The hob measurements also followed a similar procedure, with the hammer excitation and the acceleration measurement being performed at its midpoint (refer to Figure 6.1.a).
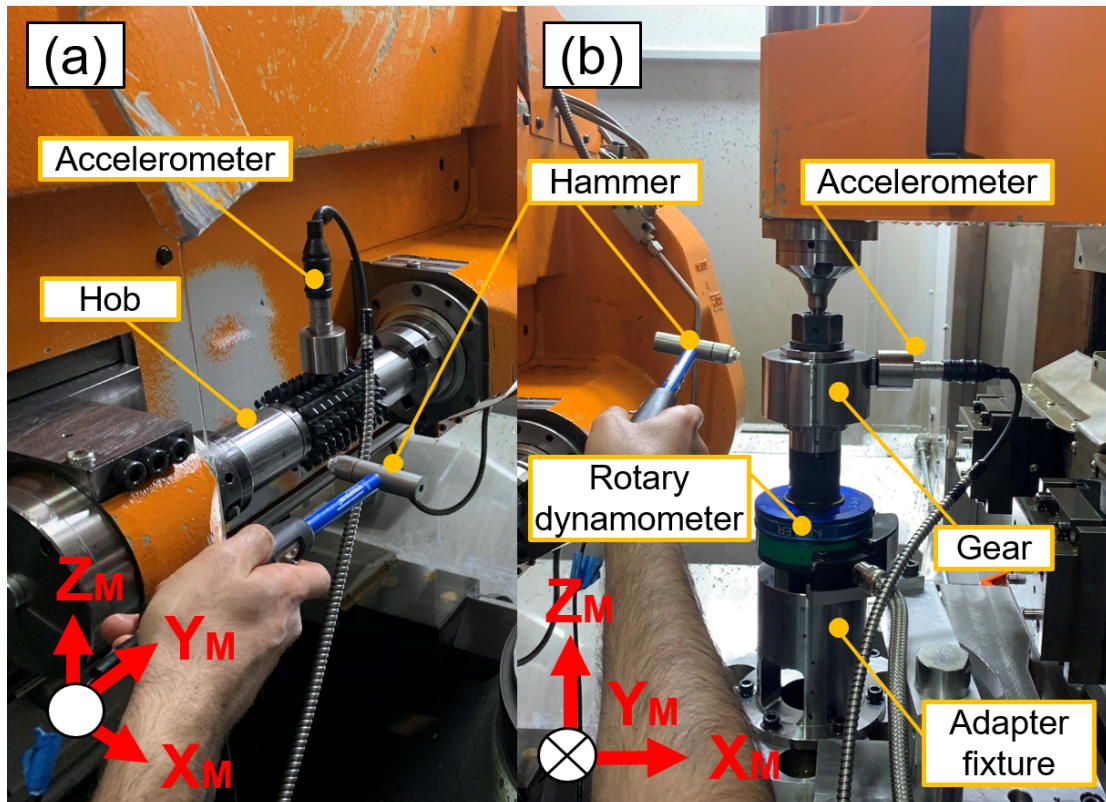
Figure 6.1: Impact hammer testing on a) hob and b) gear structure (Setup I)

Figure 6.3 displays the measured and fitted model receptance FRFs of the hob in the x and z directions of MCS. It was noted that the hob's y direction was 9$\times$ more rigid, and the cross sensitivities (such as x-y, y-z) were observed to be negligible ($> 10\times$ more rigid). In the static stiffness calculations, the effect of negative modes that appear as positive peaks in the imaginary component are ignored because they are believed to result from rotational modes of the hob, rather than bending modes. The modal parameters are displayed in Table 6.2.

In this study, the concurrent impact of workpiece and tool deformation will be taken into account, given that they have comparable static stiffness (with the tool being only 2-3 times stiffer). It is probable that a considerable portion of the flexibility observed in the

measured workpiece stiffness can be attributed to the additional fixturing that is required to attach the rotary dynamometer to the gear worktable. Hence, the workpiece employed in an actual production process would be considerably more rigid.

Table 6.1: Identified modal parameters by fitting the measured FRF in x and y directions of the workpiece (Setup I)

| m	ω_n [Hz]	ζ [%]	$k \times 10^8$ [N/m]
		x direction	
1	120	2.08	10.694
2	205	1.71	8.866
3	284	4.23	4.703
4	329	2.89	7.137
5	423	3.08	3.133
6	503	2.29	7.585
7	576	2.26	2.913
8	642	5.84	1.800
9	813	4.67	9.336
10	1249	4.96	11.612
			$K_{g,x} = 0.476$
		y direction	
1	381	3.94	5.731
2	421	4.16	4.037
3	491	3.16	5.747
4	583	9.26	0.881
5	850	3.24	19.758
6	1251	2.64	17.681
			$K_{g,y} = 0.543$
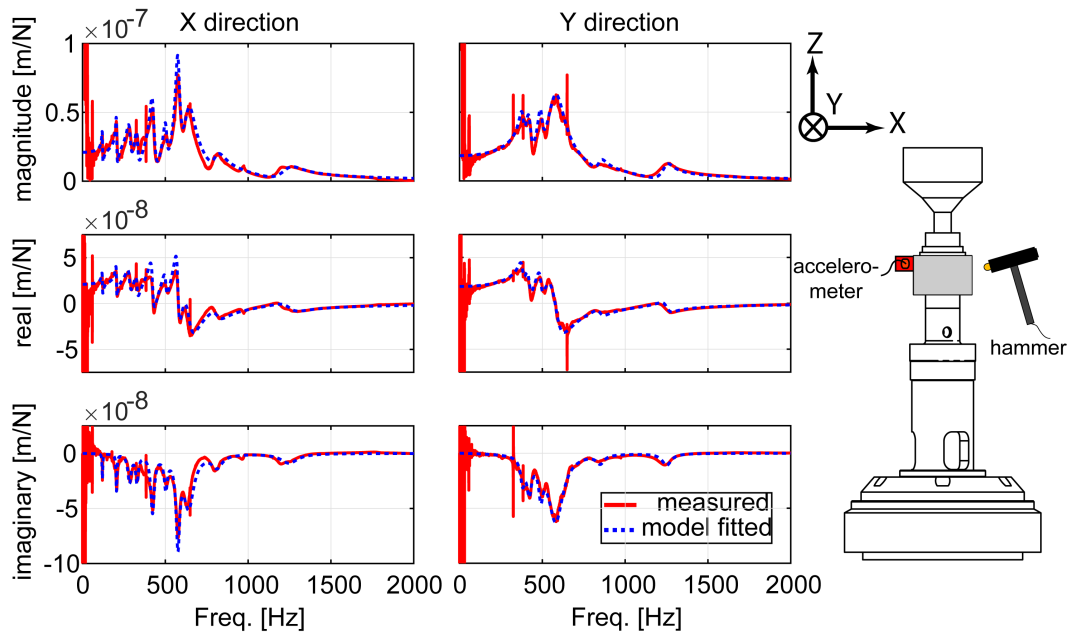
Figure 6.2: Measured and fitted model receptance FRF of the workpiece (Setup I)
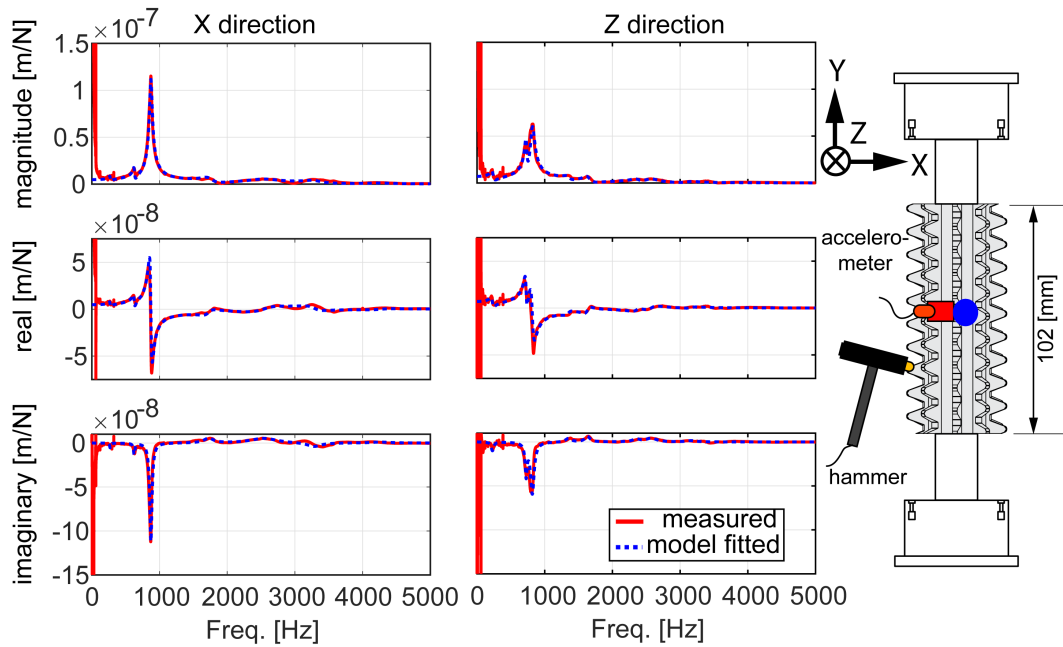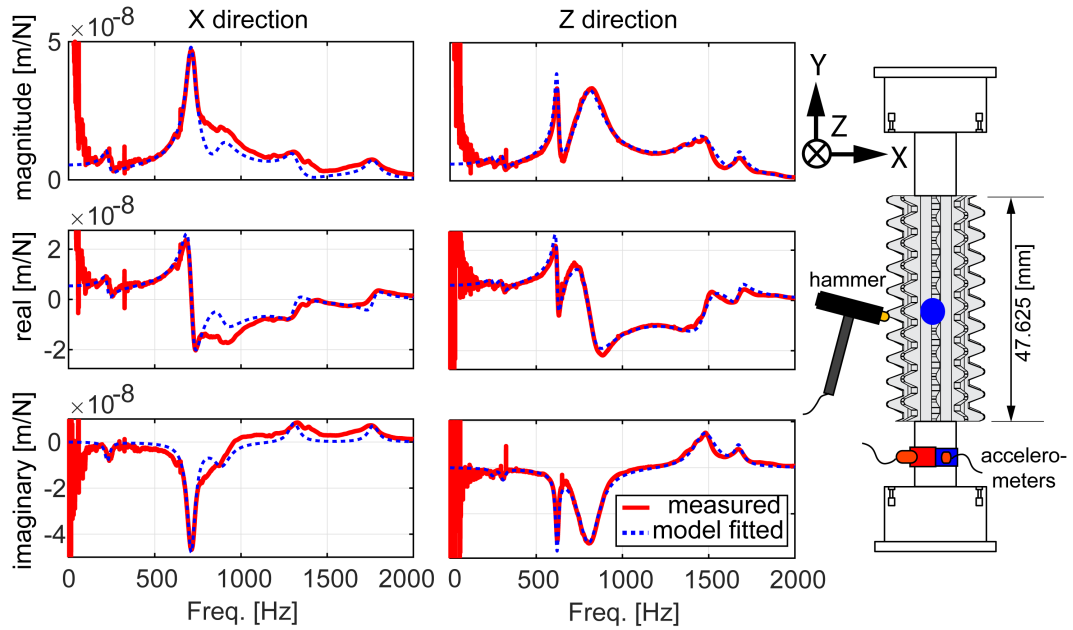

Figure 6.3: Measured and fitted model receptance FRF of the tool (Setup I)

127

Table 6.2: Identified modal parameters by fitting the measured FRF in x and z directions of the tool (Setup I)

m	ω_n [Hz]	ζ [%]	$k \times 10^8$ [N/m]
	x direction		
1	270	2.96	32.039
2	625	2.08	19.380
3	872.5	2.35	1.905
4	1728	4.86	-19.048
5	2553	9.48	-9.705
6	3286	3.90	29.233
7	4265	4.30	-108.41
			$K_{c,x} = 1.557$
	z direction		
1	229	9.61	5.273
2	726	2.41	5.849
3	818	3.97	2.159
4	1351	3.77	-32.352
5	1631	2.85	-27.454
6	2355	2.74	-59.291
7	2577	3.61	-33.353
8	3166	2.54	-142.810
			$K_{c,z} = 1.214$

6.2.1.2 Setup II: Crown-hobbed gear case study

A shaft measuring 565.5 mm in length and 31.38 mm in diameter was machined through a two-pass crown hobbing process to create a gear spline at the bottom of the shaft. Crown hobbing is a manufacturing method for producing gears with high accuracy and surface finish and is ideal for creating gears with complex tooth profiles and non-standard shapes. This is typically achieved by adjusting the center-to-center distance between the hob and gear as it is axially fed through the workpiece. In symmetrical crowning, this adjustment follows a symmetrical parabolic relationship between the center-to-center distance and the axial position of the hob. While the kinematics of the crown hobbing process can be modeled and fed into the developed integrated simulation engine, the commanded CNC data from the hobbing machine's feed drive axes were collected and directly applied as inputs to the hobbing simulation engine. The tool and gear geometries and process parameters used for this setup are shown in Tables 6.3, 6.4 and 6.5, respectively.

Table 6.3: Tool geometry data (Setup II)

Parameters	Value
Normal module m_{nc} [mm]	2.116
Number of starts N_c	1
Number of flutes (gashes)	12
Addendum diameter d_{ac} [mm]	47.625
Dedendum diameter d_{dc} [mm]	42.235
Pitch diameter d_{pc} [mm]	44.765
Pressure angle α_{nc} [^{o}]	30.0
Length L_c [mm]	47.625
Rake angle α_r [^{o}]	0.0

Similar to the procedure applied for Setup I, the accelerance FRF was experimentally measured in the machine's x, y and z directions for the workpiece and hob. For the workpiece measurements, the hammer excitation was performed at the top of the gear spline (where the cutting action takes place) while the acceleration measurements were
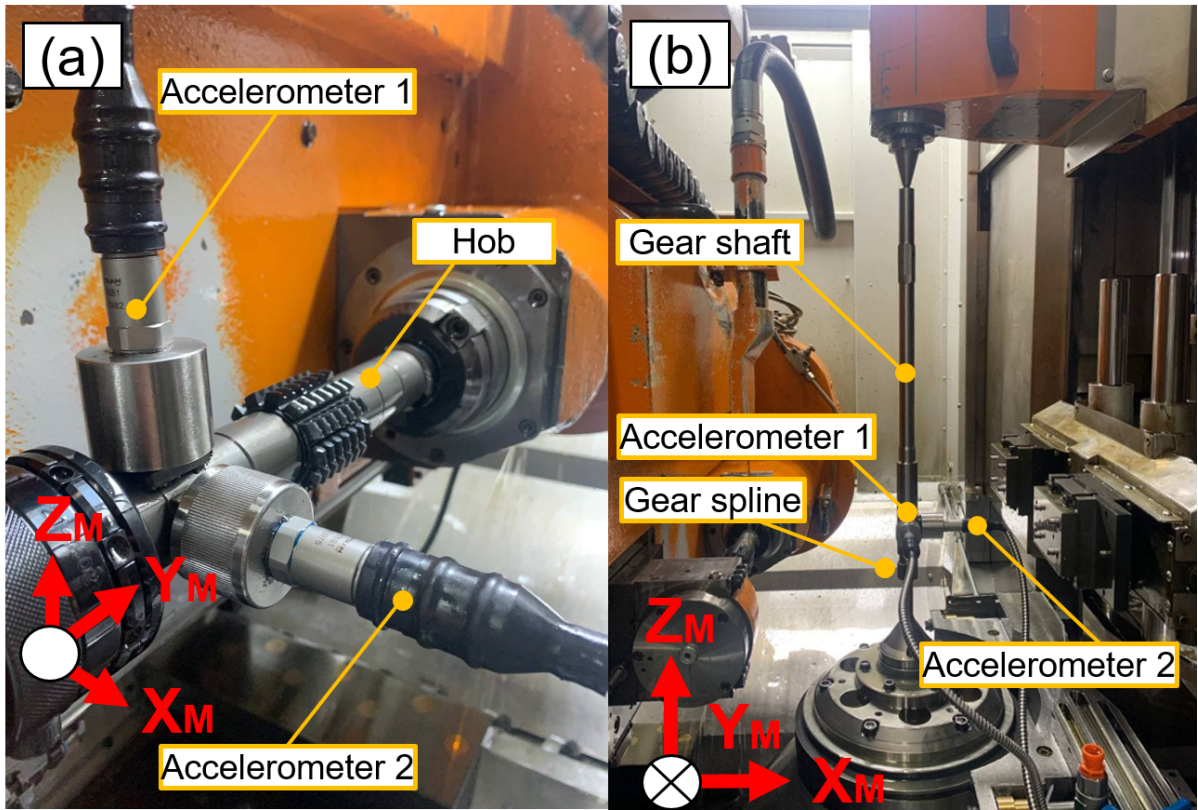
Figure 6.4: Impact hammer testing on a) hob and b) gear structure (Setup II)

taken 25 mm above the top of the gear where the sensors could be securely mounted (see Figure 6.4.b). The measured and fitted model FRFs, and extracted modal parameters are demonstrated in Figure 6.5 and Table 6.6, respectively. The hob measurements followed a similar procedure, with the hammer excitation being performed at its midpoint and the acceleration response measured near its end (refer to Figure 6.4.a). Figure 6.6 displays the measured and fitted model receptance FRF of the hob in the x and z directions of MCS. For both the hob and part, the axial directions and the cross FRFs were observed to be negligible ($> 8\times$). As in Setup I, the effect of negative modes are ignored in the static stiffness calculations. The modal parameters are displayed in Table 6.7.

In this setup, only the influence of the workpiece deformation will be taken into account

130

Table 6.4: Workpiece geometry data (Setup II)

Parameters	Value
Normal module m_{ng} [mm]	2.116
Number of teeth	14
Addendum diameter d_{ag} [mm]	31.377
Dedendum diameter d_{dg} [mm]	27.48
Helix angle β [^{o}]	0.0
Pressure angle α_{ng} [^{o}]	30.0
Gear width w_g [mm]	25.8
High point location [mm]	12.8
Lead crowning value [μm]	6.5
Material	AISI 4140

Table 6.5: Cutting process parameters (Setup II)

Pass number	1	2
roughing vs. finishing	roughing	finishing
v_f [mm/WR]	1.75	1.10
d_c [mm]	2.31	0.4
V_c [m/min]	60	88
v_r [mm/WR]	NA	0.16
axial feed strategy	climb	climb
crowning method	symmetrical	symmetrical

since the tool is about 50-65 times stiffer than the workpiece.
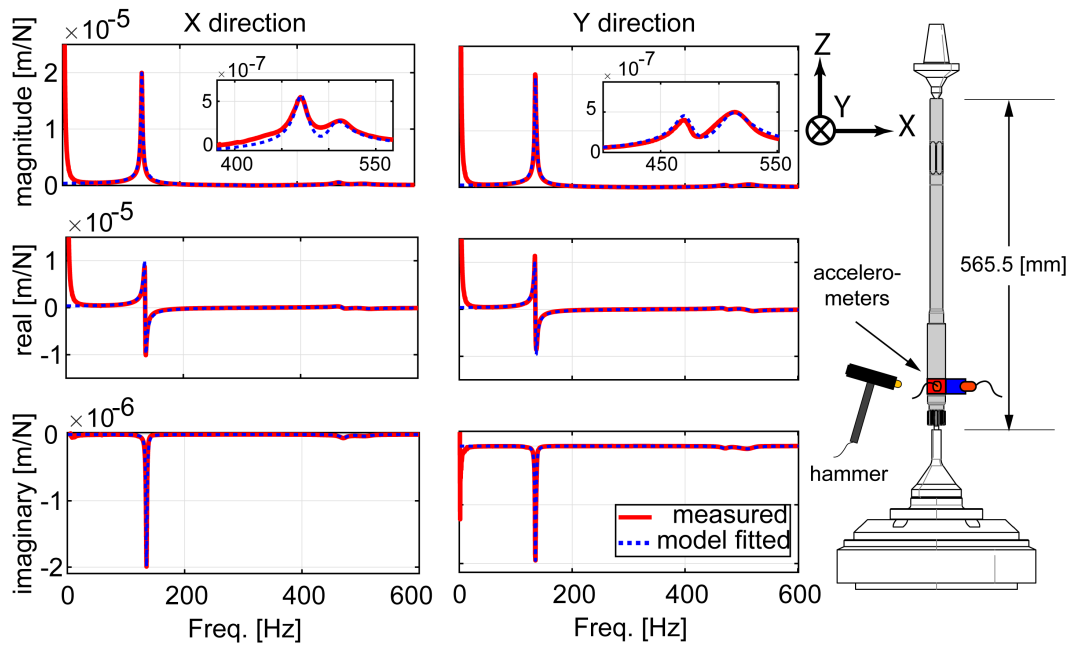
Figure 6.5: Measured and fitted model receptance FRF of the workpiece (Setup II)

Figure 6.6: Measured and fitted model receptance FRF of the tool (Setup II)

132

Table 6.6: Identified modal parameters by fitting the measured FRF in x and y directions of the workpiece (Setup II)

m	ω_n [Hz]	ζ [%]	$k \times 10^6$ [N/m]
		x direction	
1	135	0.093	2.7131
2	471	1.33	70.355
3	507	2.27	88.433
			$K_{g,x} = 2.537$
		y direction	
1	135	0.093	2.7751
2	472	1.63	80.285
3	511	2.69	40.095
			$K_{g,y} = 2.514$

Table 6.7: Identified modal parameters by fitting the measured FRF in x and z directions of the hob (Setup II)

m	ω_n [Hz]	ζ [%]	$k \times 10^6$ [N/m]
		x direction	
1	226	7.52	818.07
2	712	3.93	271.25
3	890	6.74	777.83
4	1308	2.94	-2012.4
5	1767	2.09	-3333.0
			$K_{c,x} = 161.43$
		z direction	
1	246	5.79	3046.3
2	308	4.87	2219.3
3	621	1.85	853.02
4	807	9.29	165.09
5	1480	5.47	-601.97
6	1674	1.79	-3475.0
			$K_{c,z} = 124.87$

6.2.2 Deflection calculation

The gear errors are defined as the deviation of the actual surface from its intended, or nominal one. The total deflection at a certain time step $(\bar{d}_t)$, can be written as follows:

$$\bar{d}_t = \bar{\delta}_{c,t} - \bar{\delta}_{g,t} \tag{6.5}$$

where $\bar{\delta}_{c,t}$ and $\bar{\delta}_{g,t}$ are the cutter and gear deflection at the current time step t. In a feedback loop, the total deflection at the previous time step is added to the tool's nominal position at the current time step as shown below:

$$\bar{p}_t = \bar{p}'_t + \bar{d}_{t-1} \tag{6.6}$$

Above, $\bar{p}$ and $\bar{p}'$ are the actual and nominal position of the hob, respectively. $\bar{d}$ denotes the total deflection due to elastic deformations of the cutter and gear. The true deflection at the current time step, which accounts for the deviation caused by cutting forces, is calculated through a simulation process that involves updating the CWE and cutting force calculations until the solution converges. This method, although accurate, is computationally expensive. For efficiency purposes, the deflection is calculated based on the cutting force from the previous time step. Reducing the simulation sampling period can decrease the size of the error in this approach. For a typical gear hobbing process, the simulation sampling period is set to a value lower than 10 milliseconds.

The cutter deflection is calculated by dividing the cutting force by the cutter's static stiffness. Before the calculation, the cutting force needs to be transformed from the workpiece coordinate system, in which the cutting force prediction algorithm operates, to the machine coordinate system wherein the modal testing was performed:

$$\bar{F}_t^{MCS} = [\boldsymbol{H}_{WCS}^{MCS}]\bar{F}_t^{WCS} \tag{6.7}$$

Above, $[\boldsymbol{H}_{WCS}^{MCS}]$ is the rotation matrix between machine and workpiece coordinate systems and is defined as:

$$[\boldsymbol{H}_{WCS}^{MCS}] = \boldsymbol{R}_{z,\theta_g(t)} = \begin{bmatrix} \cos(\theta_g(t)) & -\sin(\theta_g(t)) & 0 \\ \sin(\theta_g(t)) & \cos(\theta_g(t)) & 0 \\ 0 & 0 & 1 \end{bmatrix} \tag{6.8}$$

Here, $\bar{F}_t^{MCS}$ and $\bar{F}_t^{WCS}$ are the cutting force vectors in the machine and workpiece coordinate systems, respectively. Then, the cutter deflection is calculated by dividing each element of the cutting force vector by its corresponding element in the stiffness vector (i.e., $\bar{K}_c^{MCS} = \begin{bmatrix} K_{c,x} & K_{c,y} & K_{c,z} \end{bmatrix}$:

$$\bar{\delta}_{c,t}^{MCS} = \bar{F}_t^{MCS} \oslash \bar{K}_c^{MCS} \tag{6.9}$$

Similarly, the gear deflection is calculated as:

$$\bar{\delta}_{g,t}^{MCS} = -\bar{F}_t^{MCS} \oslash \bar{K}_g^{MCS} \tag{6.10}$$

Finally, the total deflection is transformed back into the workpiece coordinate system as below:

$$\bar{d}_t^{WCS} = [\boldsymbol{H}_{WCS}^{MCS}]^T \bar{d}_t^{MCS} = [\boldsymbol{H}_{WCS}^{MCS}]^T \bar{F}_t^{MCS} \oslash (\bar{K}_c^{MCS} + \bar{K}_g^{MCS}) \tag{6.11}$$

6.3 Virtual gear measurement

The virtual gear inspection module of UW's gear machining simulation and metrology software [75] was used to determine the impact of tool deflection on machined gear quality. This module can predict the errors that are typically used in the gear industry to assess gear quality, which are deviations in the profile and helix curves. The profile curve is the flank curve of a gear tooth in the transverse plane, while the lead curve is the curve along the width of the flank. For spur gears, the lead curve is a straight line, while for helical gears, it is a helix. The lead curve is typically determined at the tolerance diameter, which is halfway between the gear's addendum and dedendum. The ANSI/AGMA 2015-1-A01 standards define the metrics used to develop virtual measurements, as shown in Figure 6.7 and Figure 6.8, as follows:

- Total error: distance between two nominal profiles that completely enclose the actual profile

- Form error: The form error is defined as the horizontal distance between two mean profiles which enclose the actual profile where the mean profile is the line of best fit of the unwrapped actual profile determined by least squares

- Slope error: horizontal distance between two points where the mean profile intersects the evaluation range lines

- Pitch error: error in the position of each flank relative to the adjacent tooth's corresponding flank

- Index error: error in the position of each flank relative to a datum tooth (cumulative pitch error)

The metrics used to measure profile deviations can also be used to assess lead deviations, although they are only presented for profile deviations. By examining cross-sections of the virtually manufactured gear established within the tri-dexel CAM engine (ModuleWorks), the virtual gear measurement module can predict profile and lead deviations, as well as their respective metrics.
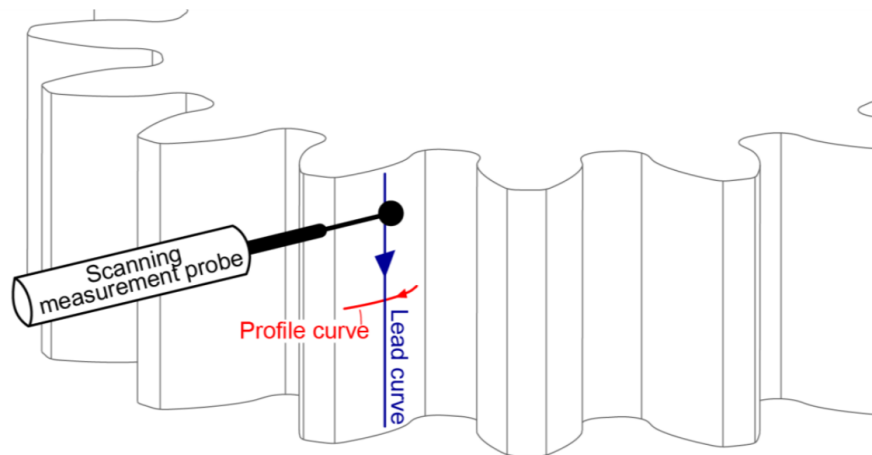
Figure 6.7: Profile and lead curve measurement (from [75])
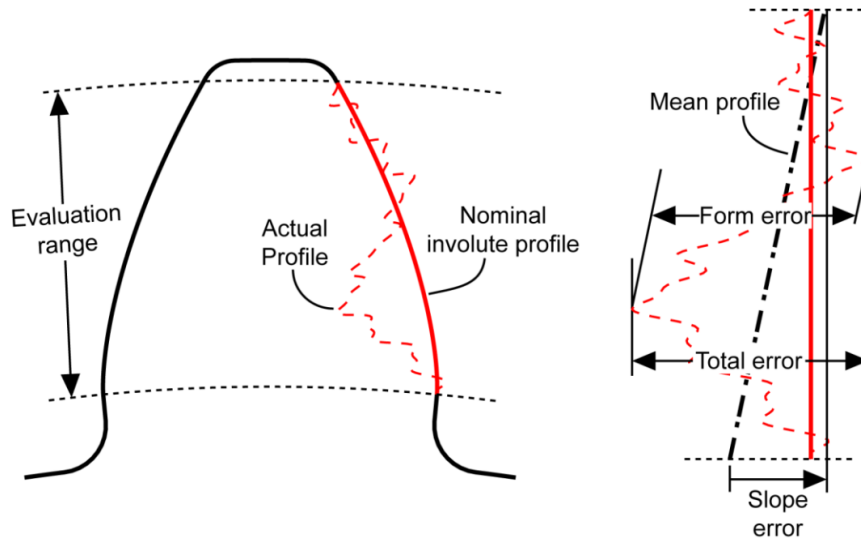
Figure 6.8: Profile error in gear inspection (from [75])

6.4   Experimental validation

This study examines the impact of cutter and gear deflections on profile and lead deviations of two case studies: two 3.175 mm module spur and helical gear which were produced on Setup I (see Figure 6.1) in a one-pass conventional hobbing process. The study focuses on the deviations on both sides of the gear (left flank and right flank) and compares the results for a rigid and a flexible structure. The actual deviations were measured after production using a GLEASON 300GMS Lead & Involute Checker to examine the manufactured gear (see Figure 6.9) and then the virtually machined gear was examined with a virtual gear measurement algorithm which replicates the standard gear metrology metrics (see Figure 6.10).

The gear inspection report produced by the Lead & Involute Checker was not available in the discrete format (e.g., csv format) and only a PDF was generated. Thus, the provided PDF report was digitized by automatically selecting each point on the curves in pixel coordinates and then converting them back to actual coordinates. A typical gear inspection report is shown in Figure 6.11.

138
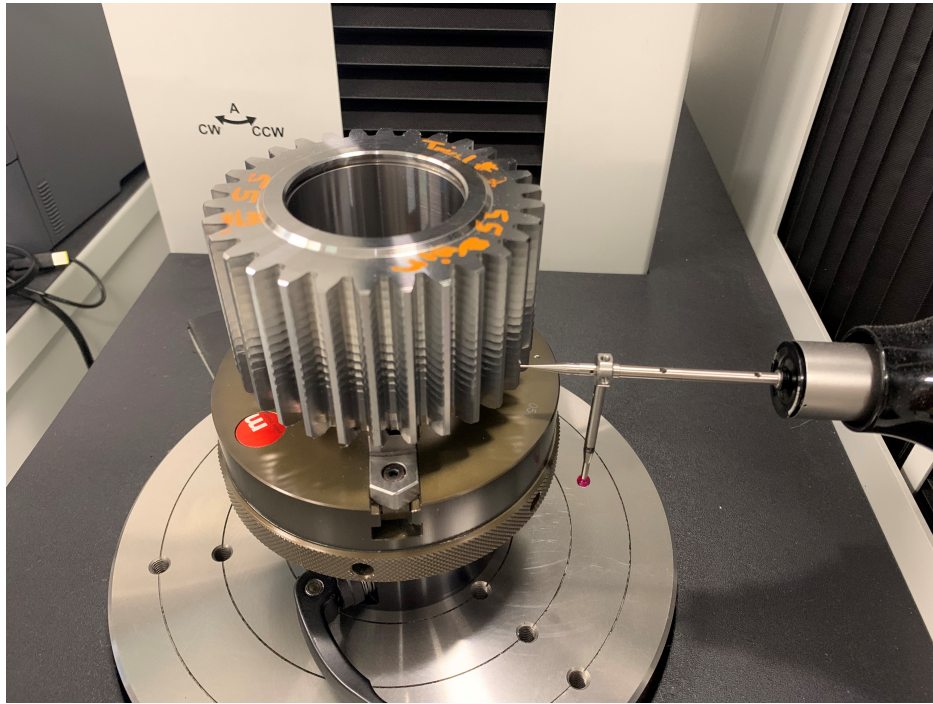
Figure 6.9: Gear inspection on GLEASON 300GMS Lead & Involute Checker
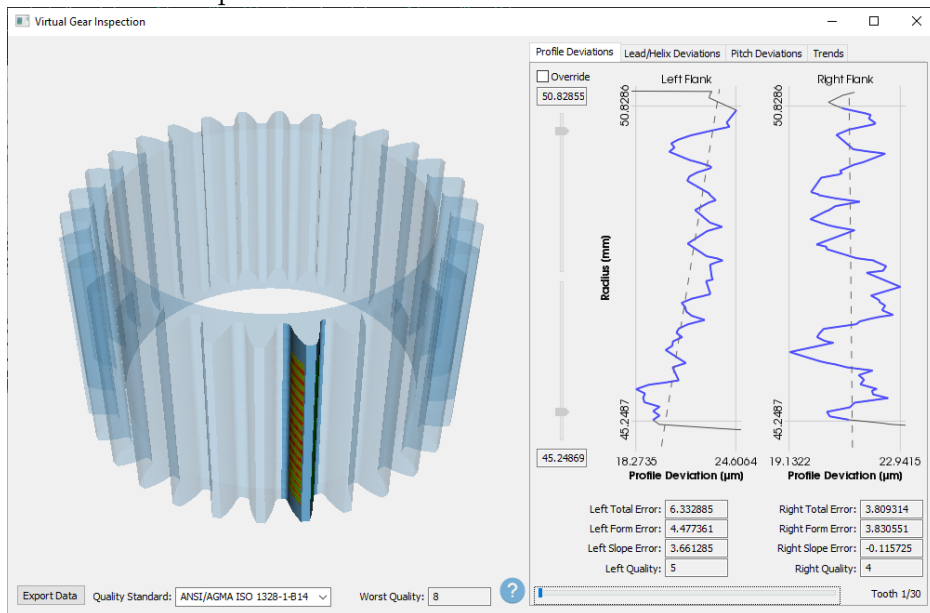
Figure 6.10: Virtual gear inspection via UW's gear metrology software [75]

PROFILE — left flank / right flank

Tolerance	Avg.	Act.value[μm]				Qual	Tolerance	Act.value[μm]				Avg.	Qual
Var Pr	13.1											13.5	
P Ang 16/10	12.0	18.0	14.9	4.9	10.0		-16/10	11.2	-2.3	0.8	11.0	5.2	
PTotal Er	12.2	17.6	14.1	6.1	11.0			14.6	9.0	7.9	15.7	11.8	
PForm Er	7.6	7.9	7.7	7.4	7.4			7.5	7.9	7.7	9.6	8.2	
A/T-ø[mm]	26.555	[26.543/26.99]						31.257	[31.123/31.377]				

Tooth: 11 8 4 1 | 1 4 8 11

LEAD VDI — left flank / right flank

	Avg.												Avg.
Var Ld	4.0												3.0
L Ang Er ±20	-2.3	-4.5	-2.2	-0.5	-2.0		±20	-11.0	-8.4	-8.0	-10.5	-9.5	
LTotal Er 18	4.8	6.2	4.4	3.5	5.2		18	10.3	8.2	9.0	11.3	9.7	
L Crown 6.5±3.5	6.1	6.0	5.8	6.1	6.6		6.5±3.5	4.7	4.0	4.3	3.9	4.2	

Tooth: 11 8 4 1 | 1 4 8 11

Figure 6.11: A generated PDF gear inspection report

Figures 6.12 and 6.13 display the lead and profile deviations of a spur gear manufactured in a single-pass process on setup I. The deviations of the flanks for teeth 3, 10, 18, and 25 are depicted. Furthermore, three error metrics (i.e., total, form and slope errors) are illustrated for each tooth. Both the measured and simulated (including rigid and elastic cases) deviations are presented, with only the horizontal axis being adjusted for an easier comparison. Hence, the horizontal axis does not depict the actual error for a particular height (for lead deviation) and flank radius (for profile deviation), but only the relative error. Although the simulation has the ability to predict this offset, the provided measurement report does not contain the actual offset values. It should be noted that the error metrics (i.e., total, form, and slope errors) remain unaffected by the offset value.

The examination of Figure 6.12 reveals that there is a good correlation in the shape and magnitude of the lead deviation on both of the right and left flanks. This is also evident from the total and form error metrics. While there is clear mismatch between the slope error prediction and measurement values, their magnitude is relatively smaller in comparison to the form and total error. Figure 6.13 reveals a noticeable difference between the predicted profile deviation and the measured one. It is apparent that other forms of deformation exist, which lead to excess material being left on the machined gear that the elastic deformation model does not account for. These deformations may include individual tooth deformation on the hob and gear, as the current model translates the entire tool profile due to cutting forces, whereas in actuality, each tooth on the hob and gear may also deform relative to its neighboring tooth. Additionally, the hob and part may undergo rotational deformation due to torque generated from the cutting force. Incorporating these effects into the model could result in improved predictions. Profile error and tool wear on the gear hob teeth can be some other sources of error, not accounted in the predictions.

Figures 6.14 and 6.15 present the lead and profile deviations of a helical gear that was machined with a single-pass process on Setup I. A similar trend to the spur gear case (illustrated in 6.12 and 6.13) is observed. Although the lead prediction correlates well with the measurements, the profile deviation predictions could benefit from further refinement of the elastic deformation model. It should be emphasized that the difference in profile variation between helical gears and spur gears is more pronounced. This is

unexpected because the static stiffness and cutting forces for both cases are nearly the same. Additionally, in the preceding two cases, the elastic deformation model and the rigid model produce comparable values, indicating that the dimensions of the virtually-machined gear are primarily affected by the kinematics of the process, rather than the bending deformation of the cutter and gear. For instance, the simulation model accurately predicts the peaks and valleys on the lead deviation (depicted in Figures 6.12 and 6.14), which originate from the process axial feed motion (3 [mm]/WR).

The lead and profile deviations of a spur gear machined using a two-pass process on Setup II are shown in Figures ?? and ??. The predicted lead deviation for teeth on the left flank closely matches the measured deviation in terms of shape and magnitude, while the lead deviation on the right flank is smaller than the actual measurement. The simulation with an elastic workpiece resulted in a better match between the simulated and measured profile deviations compared to the simulation with a rigid workpiece, as evidenced in Figure ??, where the predicted profile total and form error metrics are closer to the measured values. Despite the finishing operation having a light depth of cut (0.4 [mm]), the gear shaft in Setup II was found to be significantly flexible, which caused noticeable elastic deformation compared to the previous two cases.

In the best of the author's knowledge, these results represent the first time where hobbing process simulated in a multi-dexel environment is then used to predict the gear quality errors. While some of the predictions show some promise, especially in the case of pronounced part or tooling flexibility, and in the prediction of lead deviations, it is clear that the modeling needs to be refined further to facilitate accurate profile predictions as well.
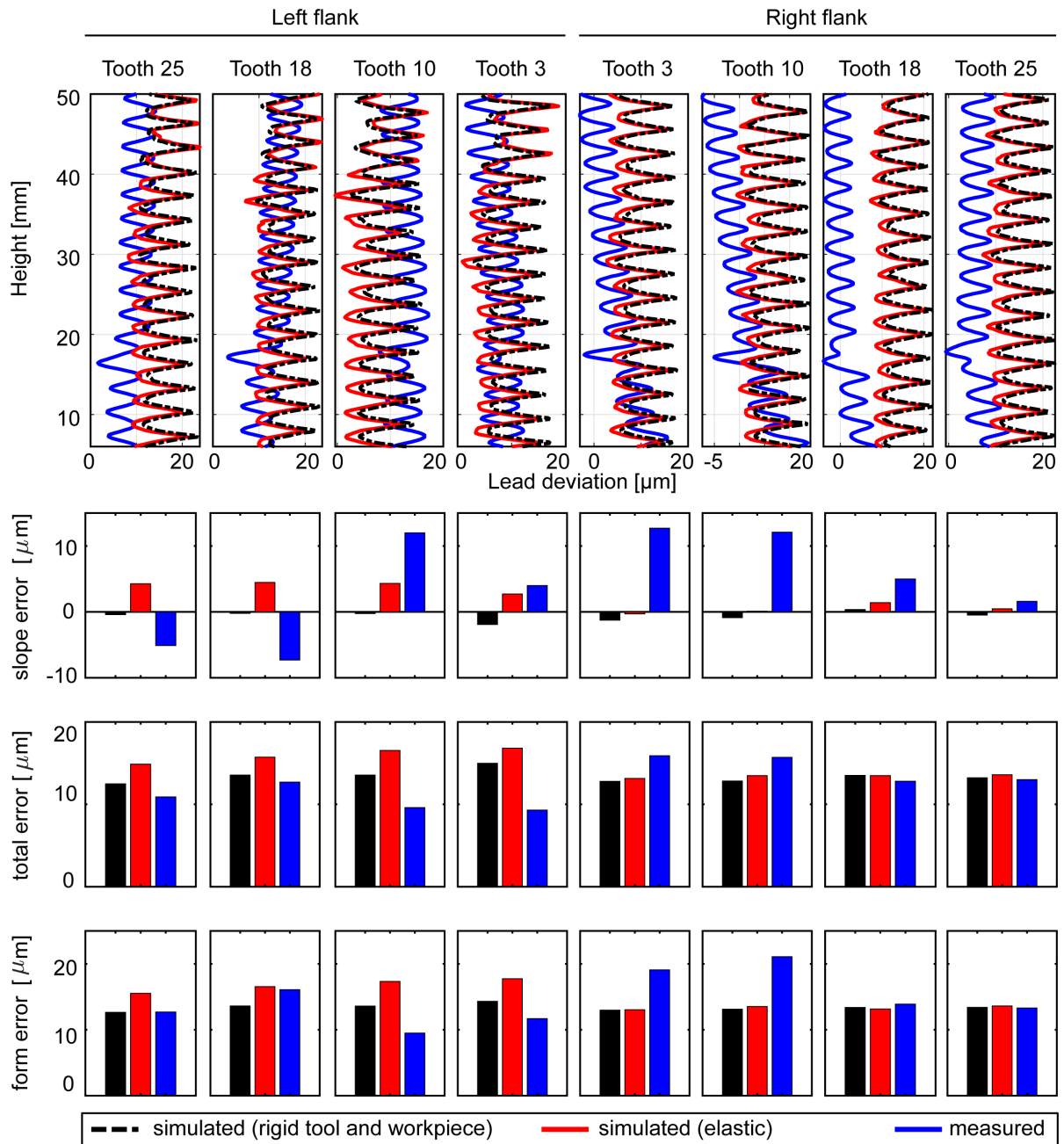
Figure 6.12: Measured and simulated lead deviation in a spur gear, Setup I (Teeth 3, 10, 18 and 25)
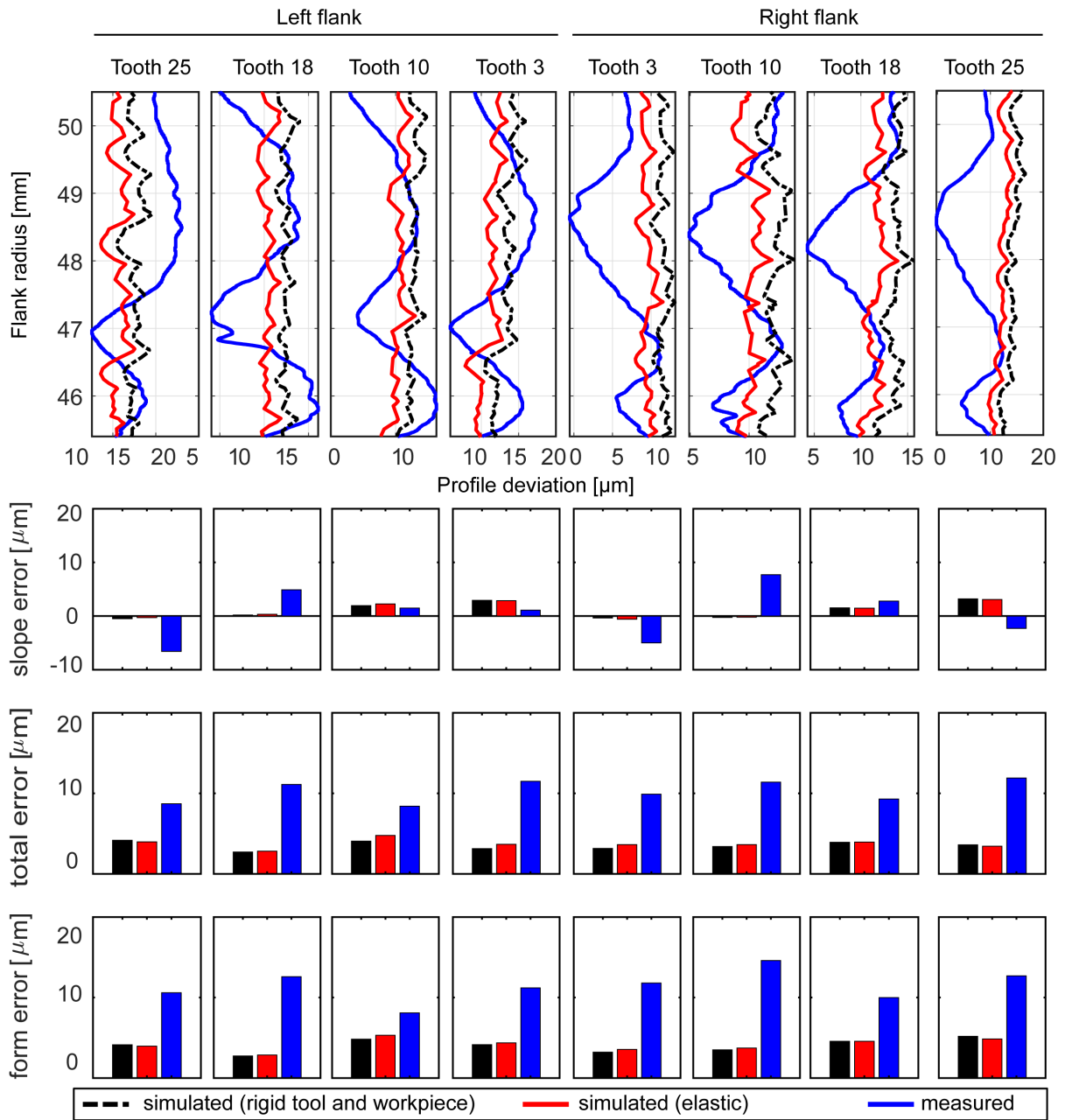
Figure 6.13: Measured and simulated profile deviation in a spur gear, Setup I (Teeth 3, 10, 18 and 25)
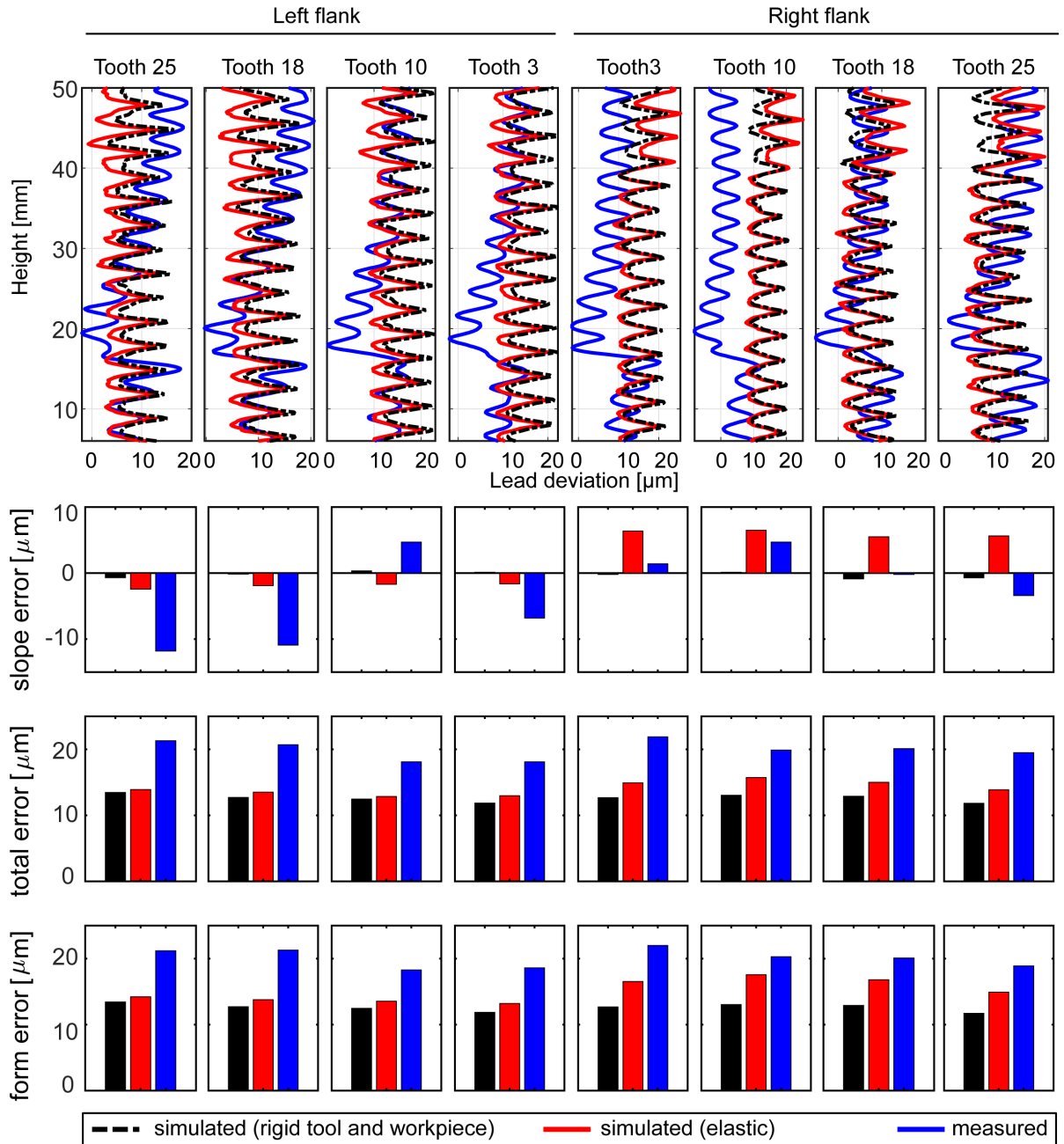
Figure 6.14: Measured and simulated lead deviation in a helical gear, Setup I (Teeth 3, 10, 18 and 25)
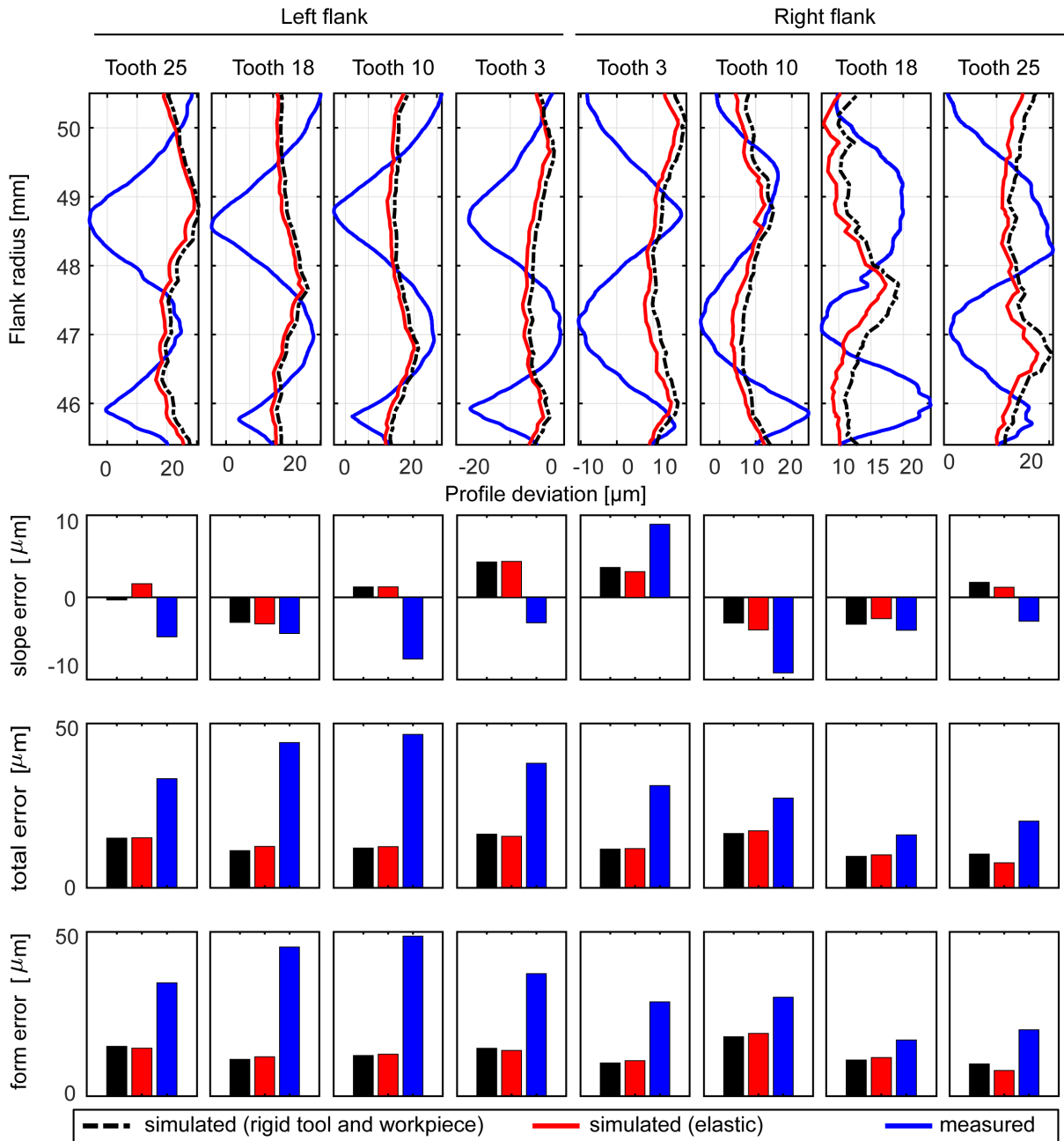
Figure 6.15: Measured and simulated profile deviation in a helical gear, Setup I (Teeth 3, 10, 18 and 25)
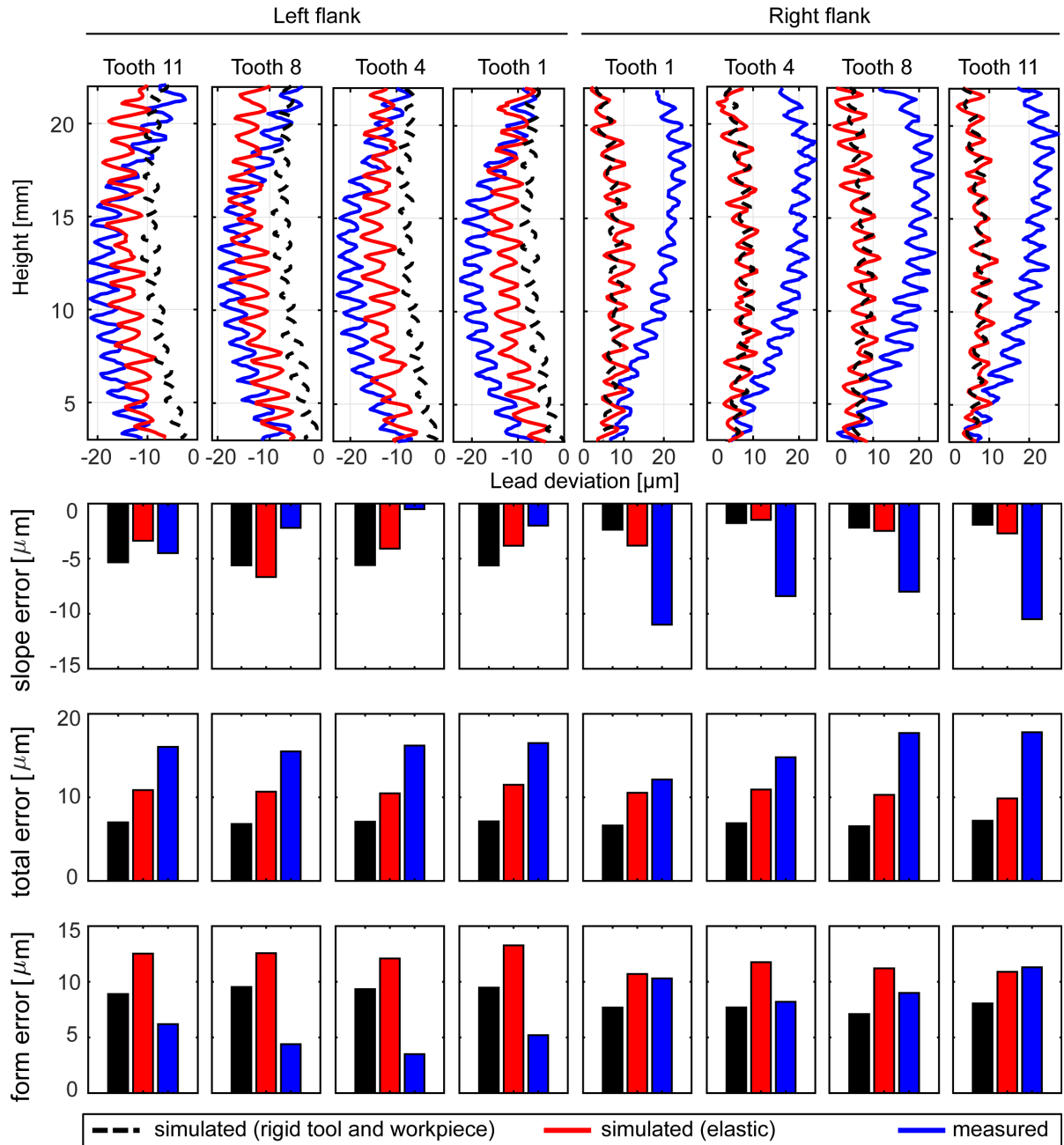
Figure 6.16: Measured and simulated lead deviation in crown-hobbed gear, Setup II (Teeth 1, 4, 8 and 11)
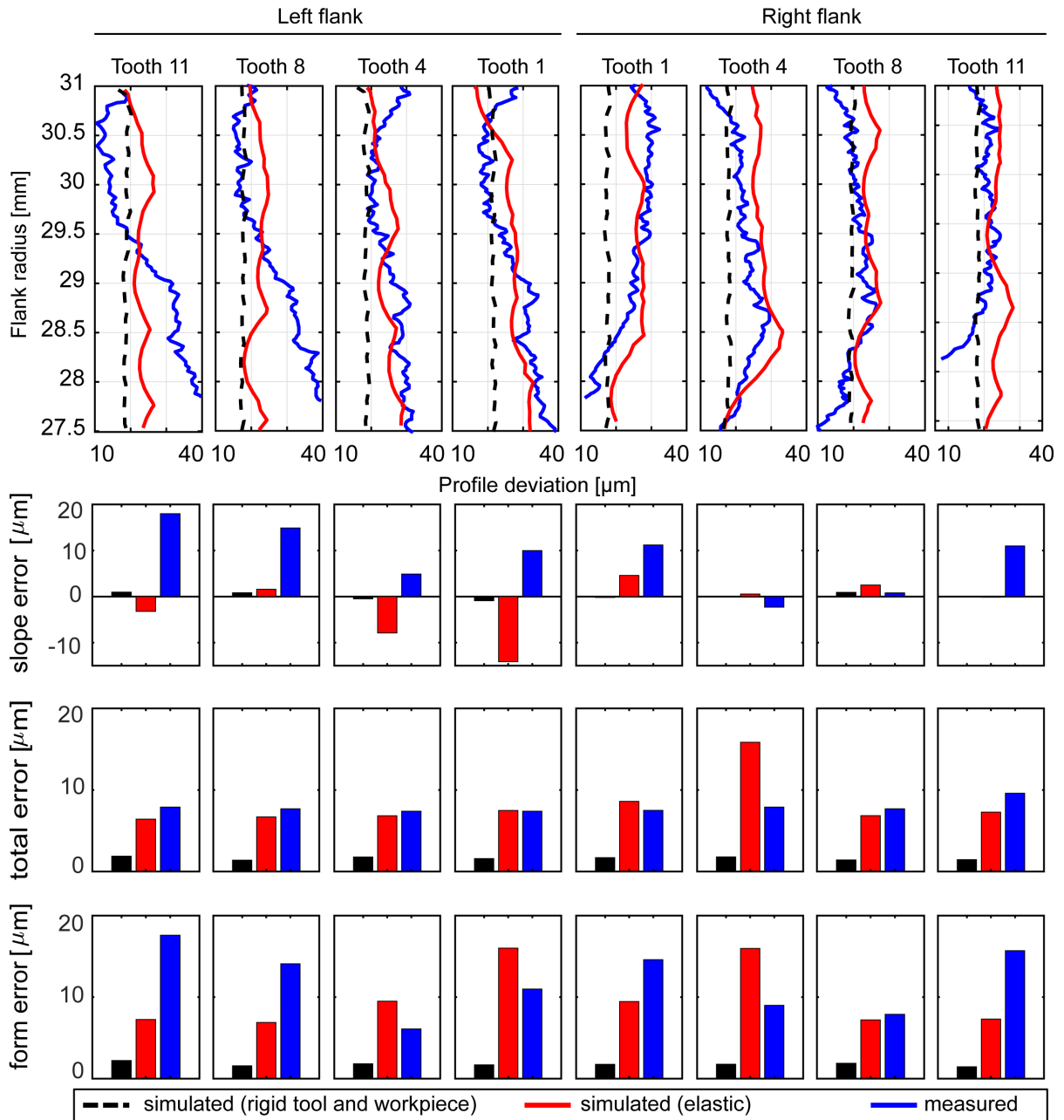
Figure 6.17: Measured and simulated profile deviation in crown-hobbed gear, SetupII (Teeth 1, 4, 8 and 11)

6.5 Conclusion

This chapter described a model for predicting hob and gear elastic deflection and their impact on lead and profile deviations of hobbed gears. The hob and gear stiffness is evaluated in the x, y, and z axes using tap testing. The measured stiffness along with simulated cutting forces are then used to calculate hob and gear deflections in a feedback loop, where the hob's deflection from the previous time step is added to its nominal position in the current time step. The virtual gear measurement module of UW's gear machining simulation and metrology software was employed to assess the impact of elastic deflections on the quality of the manufactured gear by evaluating the profile and lead deviations. The simulated lead deviation showed a reasonable correlation in different case studies. However, discrepancies are observed, particularly for the profile deviation, suggesting that there may be other significant sources of dimensional error that require further research. This research provides a foundation for future investigations into quality prediction and the simulation of vibrations during gear machining by hobbing.

Chapter 7

Conclusions and future work

7.1 Conclusions

In this thesis, a comprehensive physics-based model for prediction of the uncut chip geometry, cutting forces, and elastic deformation in gear hobbing is presented. The outcome of the thesis can play a key role in meeting the gear machining industry demands, by enabling accurate process simulation, analysis, and optimization. Additionally, it is also well-aligned with the long- term objectives of the Industry 4.0 initiative, towards digitalization and intelligent manufacturing. The main contributions and conclusions of this thesis are summarized as follows:

In Chapter 3, the kinematics of the hobbing process is mathematically modeled. The kinematic model establishes the relative motion of the cutter with respect to the workpiece at every point along the cutting edges, and thus is an essential component of the cutting force model. The kinematic model was experimentally validated partially by comparing the predicted feed drive movements with the collected position trajectories of a hobbing machine's CNC (Siemens 840D). Another verification of the kinematic model was obtained by coupling the position trajectories with the dexel-based geometric modeler, which succeeded in producing correct gear geometries upon via subtractive Boolean operations.

As the first main contribution of this thesis, a new method for predicting the cutting forces in gear hobbing has been proposed in Chapter 4. In this model, the cutting edge of the hob is discretized into nodes. Each of these nodes represents a generalized oblique cutting force model with their local cutting condition and kinematics. By integrating the kinematic model within a tri-dexel CWE calculator, the uncut chip geometry is extracted in 3D dexel format at each simulation time step. The 2D cross section of the chip geometry is constructed using Delaunay triangulation and alpha shape reconstruction methods. Chip are triangles were associated with their neighboring nodes to establish local uncut chip attributes (i.e., thickness, width, and area). Finally, the incremental forces are summed over the length of the cutting edge to determine the total cutting force at each time step.

The predictions of presented cutting force model were compared with the cutting force measurements obtained from cutting external spur and helical gears in Chapter 5. To measure the forces on a Liebherr LC 500 hobbing CNC machine, a rotary dynamometer was adapted using a custom fixture. Before comparing the results, the parasitic effect of harmonic tailstock axial force was removed and the vibratory structural distortion caused by the measurement assembly itself was compensated using Kalman filtering. In the best of the author's knowledge, this is the first time in literature that such a force measurement apparatus and data processing approach has been applied for hobbing. Excluding the finishing passes, the comparison revealed that prediction results are within 7-21% RMS error from the measured forces, with forces in z direction (i.e., largest component) demonstrating the least discrepancy. The accuracy of the prediction reduces when the magnitude of the cutting forces are smaller (e.g., cutting with lower axial feed rates or depth of cut). For example, the finishing passes showed the most discrepancy (24-36% RMS error) due to forces being smaller, and the apparent signal-to-noise ratio. Nevertheless, the RMS of the predicted peak stroke forces and average stroke forces matched closely with the measured forces throughout the trials.

The second main contribution of this thesis is presented in Chapter 6. A model for predicting the elastic deformation of the hob and gear based on the estimated static stiffness of the machine is presented. The static stiffness is approximated from experimentally-measured mechanical FRFs of the system, which were obtained from tap testing. The

gear and hob deflection are calculated by dividing the cutting forces with the estimated static stiffness, and then superposing the deflections on top of the the nominal position of the tool. The effect of hob and gear deflection on the machined gear quality was virtually investigated in UW's integrated gear machining simulation and metrology software following ANSI/AGMA gear error metrics. The simulated profile and lead deviations were compared with the report obtained from GLEASON 300GMS Lead & Involute Checker. The simulated lead deviation showed good correlation to its measured counterpart, through capturing the effects of kinematics and elastic deformations. However, the profile deviations demonstrated more discrepancy for which further research is required. Nevertheless, in the best of the author's knowledge, this study investigated for the first time the prediction of gear quality errors due to kinematics and elastic deformations, through simulation using a tri-dexel solid modeling engine.

7.2   Future work

There are several avenues of research that can be followed to improve the current development with the cutting force and elastic deformation in the focal point. Although the cutting forces may have been distorted by the dynamometer and its adapter fixture, improving the accuracy of the hob and blank geometry representation is expected to enhance the cutting force prediction. Due to the thin and small chip geometry in hobbing trials, ranging from 20-120 μm, even a slight inaccuracy in the representation of the hob and gear blank geometries, of the relative axis motions generated by the gear hobbing CNC machine tool, can lead to significant changes in the CWE and chip geometry predictions. For example, adopting more precise representations of the hob and workpiece geometry (via direct measurement rather than through nominal specifications) may provide further prediction accuracy.

Although most hobbing tools are produced without a global rake angle and with flat flutes, the model can be expanded to incorporate hobs with a global rake angle and twisted flutes in order to simulate a broader range of hobbing scenarios.

152

The elastic deformation model employs a simplified elastic deformation model to determine the hob and gear deflections. Although bending deflection may be the primary mode of deformation, particularly in the analysis of long and slender shafts, the inclusion of the torsional stiffness of the hob and gear can enhance the accuracy of the predictions. It should be emphasized that installing an accelerometer on the flutes of the hob is challenging due to the hob's complex geometry. Therefore, accurate characterization of the hob's flexibility and mode shapes is difficult. Additionally, directing a laser vibrometer beam towards the cutting edge is difficult due to the limited accessibility within the hobbing machine. Moreover, the elastic deformation model utilized in this study assumes that the geometry of the hob and gear do not deform from their nominal geometries, and are simply translated away from their nominal position. While this assumption may be a reasonable approximation, in reality, the adjacent hob flutes may experience relative deformation. Also, consideration of the rotational flexibility around multiple axes may help improve the model fidelity. Therefore, further research could explore new deformation models that incorporate the rotational degrees of freedom for rigid-body movement of the hob and workpiece, as well as the deformation of the individual flutes and teeth.

Chatter vibration is a common problem in the hobbing of long and slender workpieces. The measured FRF that was utilized for estimation of static stiffness can be used in the time-domain modeling of forced and chatter vibrations in hobbing. Therefore, future studies can prioritize the development of a chatter model in the time domain with experimental investigations. Simulating chatter in the time domain is more computationally intensive than simulating static or elastic deformations, since it necessitates higher numerical integration frequencies. Consequently, it is crucial to explore stability issues using semi-discretization and frequency domain methods, which naturally present another significant avenue for future research.

To complete the virtual simulation of gear hobbing, optimization algorithms can be incorporated. In most cases, gears that do not require additional grinding undergo multi-pass hobbing that includes roughing and finishing. Optimization can be conducted subjected to controlling the cutting force, elastic deformations, number of finishing/roughing passes or the final quality of the gear. However, it is important to note that these optimiza-

153

tion methods entail running numerous hobbing simulations, which can be time-consuming. Nevertheless, as this study has established a foundation for realistic prediction of hobbing physics and process outcomes, its results can now be integrated with various optimization algorithm for streamlining production planning in industry, and reducing energy consumption and material waste due to physical trial-and-errors.

Letters of copyright permission

Figure 7.1: Copyright for Figures 2.1 and 2.2.b

Figure 7.2: Copyright for Figures 2.2.a, 2.10 and A.4

Figure 7.3: Copyright for Figure 2.3.a

Figure 7.4: Copyright for Figure 2.3.b

159

Figure 7.5: Copyright for Figure 2.6

Figure 7.6: Copyright for Figure 2.8

Figure 7.7: Copyright for Figure 2.9

Figure 7.8: Copyright for Figure 2.11

Figure 7.9: Copyright for Figure 2.12.a

164

Figure 7.10: Copyright for Figures 2.12.b, 2.12.c, 6.7 and 6.8

RE: Requesting permission to use an image from Liebherr public-domain documentation in a PhD thesis

Kaan Erkorkmaz
To   Weber Thomas (LVT)
Cc   Milad Azvar

Dear Mr. Thomas,

Thank you very much for your swift reply!

Best regards,
Kaan Erkorkmaz

From: Weber Thomas (LVT) <▮▮▮▮▮▮▮▮▮▮▮▮▮▮>
Sent: July 7, 2023 3:53 AM
To: Kaan Erkorkmaz ▮▮▮▮▮▮▮▮▮▮
Cc: ▮▮▮▮▮▮▮▮▮▮▮▮▮▮▮▮▮▮
Subject: AW: Requesting permission to use an image from Liebherr public-domain documentation in a PhD thesis

Dear Mr. Erkormaz,

This is our permission to use this illustration.

Best Regards
Thomas Weber

Figure 7.11: Copyright for Figure 3.10

References

[1] Prem H Daryani. *The art of gear fabrication*. Industrial Press Inc., 2001.

[2] Mikel Armendia, Aitor Alzaga, Flavien Peysson, Tobias Fuertjes, Frédéric Cugnon, Erdem Ozturk, and Dominik Flum. Machine Tool: From the Digital Twin to the Cyber-Physical Systems. In *Twin-Control*, pages 3–21. Springer, 2019.

[3] Yusuf Altintas. *Manufacturing automation: metal cutting mechanics, machine tool vibrations, and CNC design*. Cambridge university press, 2012.

[4] O Burak Ozdoganlar and William J Endres. An analytical representation of chip area for corner-radiused tools under both depth-of-cut and feed variations. *Journal of manufacturing science and engineering*, 122(4):660–665, 2000.

[5] Emre Ozlu and Erhan Budak. Analytical modeling of chatter stability in turning and boring operations—part I: model development. *Journal of Manufacturing Science and Engineering*, 129(4):726–732, 2007.

[6] F Atabey, I Lazoglu, and Y Altintas. Mechanics of boring processes—part I. *International journal of machine tools and manufacture*, 43(5):463–476, 2003.

[7] H Q Zheng, X P Li, Y S Wong, and A Y C Nee. Theoretical modelling and simulation of cutting forces in face milling with cutter runout. *International Journal of Machine Tools and Manufacture*, 39(12):2003–2018, 1999.

[8] H S Kim and K F Ehmann. A cutting force model for face milling operations. *International Journal of Machine Tools and Manufacture*, 33(5):651–673, 1993.

[9] Erhan Budak. Analytical models for high performance milling. Part I: Cutting forces, structural deformations and tolerance integrity. *International Journal of Machine Tools and Manufacture*, 46(12-13):1478–1488, 2006.

[10] Haiyan Wang, Xuda Qin, Chengzu Ren, and Qi Wang. Prediction of cutting forces in helical milling process. *The International Journal of Advanced Manufacturing Technology*, 58(9-12):849–859, 2012.

[11] Minyang Yang and Heeduck Park. The prediction of cutting force in ball-end milling. *International Journal of Machine Tools and Manufacture*, 31(1):45–54, 1991.

[12] P Lee and Yusuf Altintas. Prediction of ball-end milling forces from orthogonal cutting data. *International Journal of Machine Tools and Manufacture*, 36(9):1059–1072, 1996.

[13] F Abrari, M A Elbestawi, and A D Spence. On the dynamics of ball end milling: modeling of cutting forces and stability analysis. *International Journal of Machine Tools and Manufacture*, 38(3):215–237, 1998.

[14] E Ozturk and Erhan Budak. Modeling of 5-axis milling processes. *Machining Science and Technology*, 11(3):287–311, 2007.

[15] M Pirtini and I Lazoglu. Forces and hole quality in drilling. *International journal of machine tools and Manufacture*, 45(11):1271–1281, 2005.

[16] P A Rey, J LeDref, Johanna Senatore, and Yann Landon. Modelling of cutting forces in orbital drilling of titanium alloy Ti–6Al–4V. *International Journal of Machine Tools and Manufacture*, 106:75–88, 2016.

[17] Mohammad Rezayi Khoshdarregi and Yusuf Altintas. Generalized modeling of chip geometry and cutting forces in multi-point thread turning. *International Journal of Machine Tools and Manufacture*, 98:21–32, 2015.

[18] M Kaymakci, Z M Kilic, and Y Altintas. Unified cutting force model for turning, boring, drilling and milling operations. *International Journal of Machine Tools and Manufacture*, 54:34–45, 2012.

[19] Y Boz, H Erdim, and I Lazoglu. A comparison of solid model and three-orthogonal dexelfield methods for cutter-workpiece engagement calculations in three-and five-axis virtual milling. *The International Journal of Advanced Manufacturing Technology*, 81(5-8):811–823, 2015.

[20] A D Spence and Y Altintas. A solid modeller based milling process simulation and planning system. *Journal of Engineering for Industry*, 116(1):61–69, 1994.

[21] Altintas Larue and Yusuf Altintas. Simulation of flank milling processes. *International Journal of Machine Tools and Manufacture*, 45(4-5):549–559, 2005.

[22] B M Imani, M H Sadeghi, and M A Elbestawi. An improved process simulation system for ball-end milling of sculptured surfaces. *International Journal of Machine Tools and Manufacture*, 38(9):1089–1107, 1998.

[23] Allan D Spence, Farid Abrari, and Mohamed A Elbestawi. Integrated solid modeller based solutions for machining. *Computer-Aided Design*, 32(8-9):553–568, 2000.

[24] B M Imani and M A Elbestawi. Geometric simulation of ball-end milling operations. *Journal of manufacturing science and engineering*, 123(2):177–184, 2001.

[25] I Lazoglu, Y Boz, and H Erdim. Five-axis milling mechanics for complex free form surfaces. *CIRP annals*, 60(1):117–120, 2011.

[26] Barry K Fussell, Robert B Jerard, and Jeffrey G Hemmett. Modeling of cutting geometry and forces for 5-axis sculptured surface machining. *Computer-Aided Design*, 35(4):333–346, 2003.

[27] Taner Tunc, Omer Mehmet Ozkirimli, Erdem Ozturk, Yavuz Murtezaouglu, and Erhan Budak. Machining strategy development in 5-axis milling operations using process models. 2010.

[28] Tim Van Hook. Real-time shaded NC milling display. In *ACM SIGGRAPH Computer Graphics*, volume 20, pages 15–20. ACM, 1986.

[29] B K Fussell, R B Jerard, and J G Hemmett. Robust feedrate selection for 3-axis NC machining using discrete models. *Journal of manufacturing science and engineering*, 123(2):214–224, 2001.

[30] Alptunc Comak and Yusuf Altintas. Mechanics of turn-milling operations. *International Journal of Machine Tools and Manufacture*, 121:2–9, 2017.

[31] Manufacturing Automation Laboratory, MAL Inc. MACHPRO: THE VIRTUAL MACHINING SYSTEM, accessed = March, 2023.

[32] M Eugene Merchant. Mechanics of the metal cutting process. I. Orthogonal cutting and a type 2 chip. *Journal of applied physics*, 16(5):267–275, 1945.

[33] E Budak, Y Altintas, and E J A Armarego. Prediction of milling force coefficients from orthogonal cutting data. *Journal of Manufacturing Science and Engineering*, 118(2):216–224, 1996.

[34] Erhan Budak and Yusuf Altintas. Peripheral milling conditions for improved dimensional accuracy. *International Journal of Machine Tools and Manufacture*, 34(7):907–918, 1994.

[35] Erhan Budak and Yusuf Altintas. Modeling and avoidance of static form errors in peripheral milling of plates. *International Journal of Machine Tools and Manufacture*, 35(3):459–476, 1995.

[36] Jer-Shyong Tsai and Chung-Li Liao. Finite-element modeling of static surface errors in the peripheral milling of thin-walled workpieces. *Journal of Materials Processing Technology*, 94(2-3):235–246, 1999.

[37] Svetan Ratchev, Shulong Liu, Wei Huang, and Adib A Becker. Milling error prediction and compensation in machining of low-rigidity parts. *International Journal of Machine Tools and Manufacture*, 44(15):1629–1641, 2004.

[38] Shi Hyoung Ryu, Hae Sung Lee, and Chong Nam Chu. The form error prediction in side wall machining considering tool deflection. *International Journal of Machine Tools and Manufacture*, 43(14):1405–1411, 2003.

[39] Erhan Budak. *Mechanics and dynamics of milling thin walled structures*. PhD thesis, University of British Columbia, 1994.

[40] Jiri Tlusty. The stability of the machine tool against self-excited vibration in machining. *Proc. Int. Res. in Production Engineering, Pittsburgh, ASME*, 465, 1963.

[41] Franz Koenigsberger and Jiri Tlusty. *Machine tool structures*. Elsevier, 2016.

[42] Ioannis Minis, Rafael Yanushevsky, Abel Tembo, and Robert Hocken. Analysis of linear and nonlinear chatter in milling. *CIRP annals*, 39(1):459–462, 1990.

[43] Y Altintas and E Budak. Analytical prediction of stability lobes in milling. *CIRP Annals-Manufacturing Technology*, 44(1):357–362, 1995.

[44] Y Altintas and E Budak. Analytical prediction of chatter stability in milling—part I: general formulation. *Journal of Dynamic Systems, Measurement, and Control*, 120:22–30, 1998.

[45] Y Altintas and E Budak. Analytical prediction of chatter stability in milling—part II: application of the general formulation to common milling systems. *Journal of Dynamic Systems, Measurement, and Control*, 120(1):31–36, 1998.

[46] Erdem Ozturk, L Taner Tunc, and Erhan Budak. Investigation of lead and tilt angle effects in 5-axis ball-end milling processes. *International Journal of Machine Tools and Manufacture*, 49(14):1053–1062, 2009.

[47] M Eynian and Y Altintas. Chatter stability of general turning operations with process damping. *Journal of Manufacturing Science and Engineering*, 131(4):41005, 2009.

[48] Jochem C Roukema and Yusuf Altintas. Generalized modeling of drilling vibrations. Part II: Chatter stability in frequency domain. *International Journal of Machine Tools and Manufacture*, 47(9):1474–1485, 2007.

[49] K Ahmadi and Y Altintas. Stability of lateral, torsional and axial vibrations in drilling. *International Journal of Machine Tools and Manufacture*, 68:63–74, 2013.

[50] Tony L Schmitz and K Scott Smith. *Machining dynamics*. Springer, 2014.

[51] K-D Bouzakis, E Lili, N Michailidis, and O Friderikos. Manufacturing of cylindrical gears by generating cutting processes: A critical synthesis of analysis methods. *CIRP Annals*, 57(2):676–696, 2008.

[52] A M Abood, R Bicker, and T Pennell. An analysis of cutting forces in gear hobbing. *VDI BERICHTE*, 1665:255–262, 2002.

[53] Ali Muzhir Abood. Dynamic analysis of the cutting forces in gear hobbing. 2003.

[54] Dimitriou Vasilis, Vidakis Nectarios, and Antoniadis Aristomenis. Advanced computer aided design simulation of gear hobbing by means of three-dimensional kinematics modeling. *Journal of Manufacturing Science and Engineering*, 129(5):911–918, 2007.

[55] V Dimitriou and A Antoniadis. CAD-based simulation of the hobbing process for the manufacturing of spur and helical gears. *The International Journal of Advanced Manufacturing Technology*, 41(3-4):347–357, 2009.

[56] Tapoglou Nikolaos and Antoniadis Aristomenis. CAD-based calculation of cutting force components in gear hobbing. *Journal of Manufacturing Science and Engineering*, 134(3):31009, 2012.

[57] Nikolaos Tapoglou and Aristomenis Antoniadis. Hob3D: a novel gear hobbing simulation software. In *Proceedings of the World Congress on Engineering*, volume 1, pages 861–864, 2011.

[58] Fritz Klocke, Christof Gorgels, Gerd-Thomas Weber, and Rolf Schalaster. Prognosis of the local tool wear in gear finish hobbing. *Production Engineering*, 5(6):651–657, 2011.

[59] F Klocke, C Gorgels, A Stuckenberg, and R Schalaster. Software- Based Process Design in Gear Finish Hobbing. *Gear Technology*, 27(3):48–52, 2010.

[60] Fritz Klocke, Christian Brecher, Christoph Löpenhaus, and Markus Krömer. Calculating the workpiece quality using a hobbing simulation. *Procedia CIRP*, 41:687–691, 2016.

[61] F Klocke, B Döbbeler, S Goetz, and T Deeke Viek. Model-based online tool monitoring for hobbing processes. *Procedia CIRP*, 58:601–606, 2017.

[62] W V Pittler. Verfahren zum Schneiden von Zahnrädern mittels eines zahnradartigen, an den Stirnflächen der Zähne mit Schneidkanten versehenen Schneidwerkzeugs. *Deutsche Patentschrift*, (243514), 1910.

[63] Herman J Stadtfeld. Power skiving of cylindrical gears on different machine platforms. *Gear Technology*, 31(1):52–62, 2014.

[64] Ichiro Moriwaki, Tsukasa Osafune, Morimasa Nakamura, Masami Funamoto, Koichiro Uriu, Takanori Murakami, Eiri Nagata, Nobuaki Kurita, Tomokazu Tachikawa, and Yoshinori Kobayashi. Cutting tool parameters of cylindrical skiving cutter with sharpening angle for internal gears. *Journal of Mechanical design*, 139(3):33301, 2017.

[65] Nikolaos Tapoglou. Calculation of non-deformed chip and gear geometry in power skiving using a CAD-based simulation. *The International Journal of Advanced Manufacturing Technology*, 100(5-8):1779–1785, 2019.

[66] Fritz Klocke, Christian Brecher, Christoph Löpenhaus, Philipp Ganser, Julian Staudt, and Markus Krömer. Technological and simulative analysis of power skiving. *Procedia CIRP*, 50:773–778, 2016.

[67] D Spath and A Hühsam. Skiving for high-performance machining of periodic structures. *CIRP Annals*, 51(1):91–94, 2002.

[68] Tomokazu Tachikawa, Daisuke Iba, Nobuaki Kurita, Morimasa Nakamura, and Ichiro Moriwaki. Basic study on calculation of cutting forces useful for reducing vibration in skiving. *Journal of Mechanical Design*, 139(10):104501, 2017.

[69] Pierce Raymond McCloskey. Virtual Model of Power Skiving Cutting Mechanics. Master's thesis, University of Waterloo, 2019.

[70] Pierce McCloskey, Andrew Katz, Luke Berglind, Kaan Erkorkmaz, Erdem Ozturk, and Fathy Ismail. Chip geometry and cutting forces in gear power skiving. *CIRP Annals*, 2019.

[71] W König and K Bouzakis. Chip formation in gear-shaping. *CIRP Ann*, 25(1):17–20, 1977.

[72] P P Datta, T K Chattopadhyay, and R N Banerjee. Computer aided stress analysis of Fellow's gear-shaping cutter at different stages of a cutting stroke. *Proceedings of the Institution of Mechanical Engineers, Part B: Journal of Engineering Manufacture*, 218(10):1297–1306, 2004.

[73] Chung-Biau Tsay, Wen-Yao Liu, and Yi-Cheng Chen. Spur gear generation by shaper cutters. *Journal of Materials Processing Technology*, 104(3):271–279, 2000.

[74] Kaan Erkorkmaz, Andrew Katz, Yasin Hosseinkhani, Denys Plakhotnik, Marc Stautner, and Fathy Ismail. Chip geometry and cutting forces in gear shaping. *CIRP Annals-Manufacturing Technology*, 65(1):133–136, 2016.

[75] Andrew Katz. Cutting Mechanics of the Gear Shaping Process. Master's thesis, University of Waterloo, 2017.

[76] Andrew Katz, Kaan Erkorkmaz, and Fathy Ismail. Virtual Model of Gear Shaping—Part I: Kinematics, Cutter–Workpiece Engagement, and Cutting Forces. *Journal of Manufacturing Science and Engineering*, 140(7):71007, 2018.

[77] Andrew Katz, Kaan Erkorkmaz, and Fathy Ismail. Virtual model of gear shaping—part ii: Elastic deformations and virtual gear metrology. *Journal of Manufacturing Science and Engineering*, 140(7):071008, 2018.

[78] Manufacturing Automation Laboratory, The University of British Columbia. ShapePro, accessed = March, 2023.

[79] Faydor L Litvin and Alfonso Fuentes. *Gear geometry and applied theory*. Cambridge University Press, 2004.

[80] I S O Standard and B S ISO. Technical report, Technical report, International Organization for Standardization, Geneva, title = 53. Cylindrical gears for general and heavy engineering-standard basic rack tooth profile, year = 1998.

[81] NC Ainsworth. Design implications for shaper cutters. *Gear Technology*, 13(4), 1996.

[82] Denis Gimpert. Gear fundamentals-the Gear hobbing process. *Gear Technology*, 11:38, 1994.

[83] Earle Buckingham. *Analytical mechanics of gears*. Courier Corporation, 1988.

[84] Robert Endoy. *Gear hobbing, shaping, and shaving: a guide to cycle time estimating and process planning*. Society of Manufacturing Engineers, 1990.

[85] Liebherr international group and family enterprise. Liebherr, accessed = March, 2023.

[86] GV Stabler. The chip flow law and its consequences. *Advances in Machine Tool Design and Research*, 5:243–251, 1964.

[87] Emre Ozlu, Erhan Budak, and A. Molinari. Analytical and experimental investigation of rake contact and friction behavior in metal cutting. *International Journal of Machine Tools and Manufacture*, 49(11):865–875, 2009.

[88] O Kienzle. Die bestimmung von kräften und Leistungen an spanenden Werkzeugen und Werkzeugmaschinen. *VDI-Z*, 94(11):299–305, 1952.

[89] ModuleWorks GmbH. https://moduleworks.com/, accessed = March, 2023.

[90] MC Leu, X Peng, and W Zhang. Surface reconstruction for interactive modeling of freeform solids by virtual sculpting. *CIRP annals*, 54(1):131–134, 2005.

[91] Weihan Zhang and Ming C Leu. Surface reconstruction using dexel data from three sets of orthogonal rays. *Journal of computing and information science in engineering*, 9(1), 2009.

[92] H. Edelsbrunner, D. Kirkpatrick, and R. Seidel. On the shape of a set of points in the plane. *IEEE Transactions on Information Theory*, 29(4):551–559, 1983.

[93] E. W. Weisstein. "Circumcircle", MathWorld–A Wolfram Web Resource. Available online: http://mathworld.wolfram.com/Circumcircle.html, accessed = March, 2023 .

[94] D. F. Watson. Computing the n-dimensional Delaunay tessellation with application to Voronoi polytopes*. *The Computer Journal*, 24(2):167–172, 01 1981.

[95] E. W. Weisstein. "Heron's Formula.", MathWorld–A Wolfram Web Resource. Available online: https://mathworld.wolfram.com/HeronsFormula.html, accessed = March, 2023 .

[96] Y. Altintas and S.S. Park. Dynamic compensation of spindle-integrated force sensors. *CIRP Annals*, 53(1):305–308, 2004.

[97] David J Ewins. *Modal testing: theory, practice and application*. John Wiley & Sons, 2009.

[98] Robert Grover Brown and Patrick YC Hwang. Introduction to random signals and applied kalman filtering: with matlab exercises and solutions. *Introduction to random signals and applied Kalman filtering: with MATLAB exercises and solutions*, 1997.

[99] Fakher Chaari, Tahar Fakhfakh, Riadh Hbaieb, Jamel Louati, and Mohamed Haddar. Influence of manufacturing errors on the dynamic behavior of planetary gears. *International Journal of Advanced Manufacturing Technology*, 27, 2006.

APPENDIX

Appendix A

Comparison of the developed cutting force model with the available CAD-based model

In this section, the cutting force model developed in this thesis is compared with the results presented in literature [56], obtained using a exact modeler based force simulation for hobbing. Direct access to the hobbing simulation code used by the researchers of [56] was not available. Therefore, results reported in [56] is used for qualitative comparison with the developed dexel-based method.

In [56], no cutting force coefficients or depth of cut are directly reported, only the material type is given as 16MnCr5BG. Additionally, the simulation results in [56] are provided for the cutting of a single tooth gap, whereas in a realistic hobbing simulation, multiple (simultaneous) tooth engagements need to be considered. Hence, these factors make one-to-one duplication of the results in [56], and the comparison with the developed model in this thesis, challenging. Nevertheless, the best effort was made to come up with a comparison study to determine if the proposed model can replicate prediction results and trends reported in [56].

A single tooth gap workpiece hobbing simulation was created, as shown in Figure

A.1. The process parameters are summarized in Tables A.1, A.2 and A.3. The cutting coefficients were obtained from the MAL Inc. (Manufacturing Automation Laboratories) CutPRO material database for an equivalent North American steel (AISI 5115). Also, it was assumed that the nominal root diameter is reached in a single pass hobbing process (i.e., depth of cut = 8.5275 [mm]). It is important to note that only the steady-state part of the process, in which the maximum cutting forces occur, is selected for simulation. This is, again, due to results in [56] not being sufficiently clear about which phase of the operation they were simulated for (i.e., entry, steady-state, or completion).

Table A.1: Tool geometry data (used in [56])

Parameters	Value
Normal module m_{nc} [mm]	3.79
Number of starts N_c	1
Number of flutes (gashes)	9
Addendum diameter d_{ac} [mm]	75.0
Dedendum diameter d_{dc} [mm]	57.945
Pitch diameter d_{pc} [mm]	67.42
Pressure angle α_{nc} [^{o}]	20.0
Length L_c [mm]	100.0
Rake angle α_r [^{o}]	0.0
Material	P25

Table A.2: Workpiece geometry data (used in [56])

Parameters	Value
Normal module m_{ng} [mm]	3.79
Number of teeth	56
Addendum diameter d_{ag} [mm]	219.82
Helix angle β [^{o}]	0.0
Pressure angle α_{ng} [^{o}]	20.0
Gear width w_g [mm]	150.0
Material	16MnCr5 BG

Table A.3: Cutting process data (one-pass process) (used in [56])

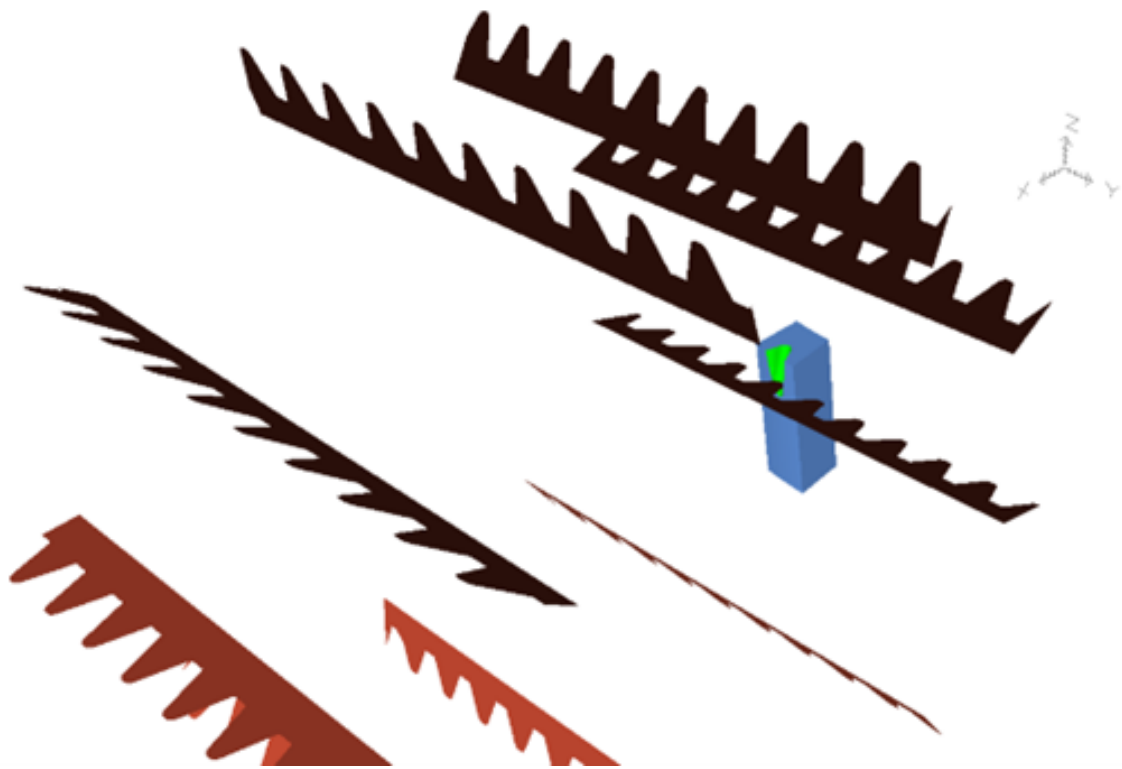| Parameters	Value
Axial feed rate v_f [mm/WR]	4.0
Depth of cut d_c [mm]	8.528
Cutting speed V_c [m/min]	120.0
Axial feed strategy	Conventional
Radial infeed strategy	None

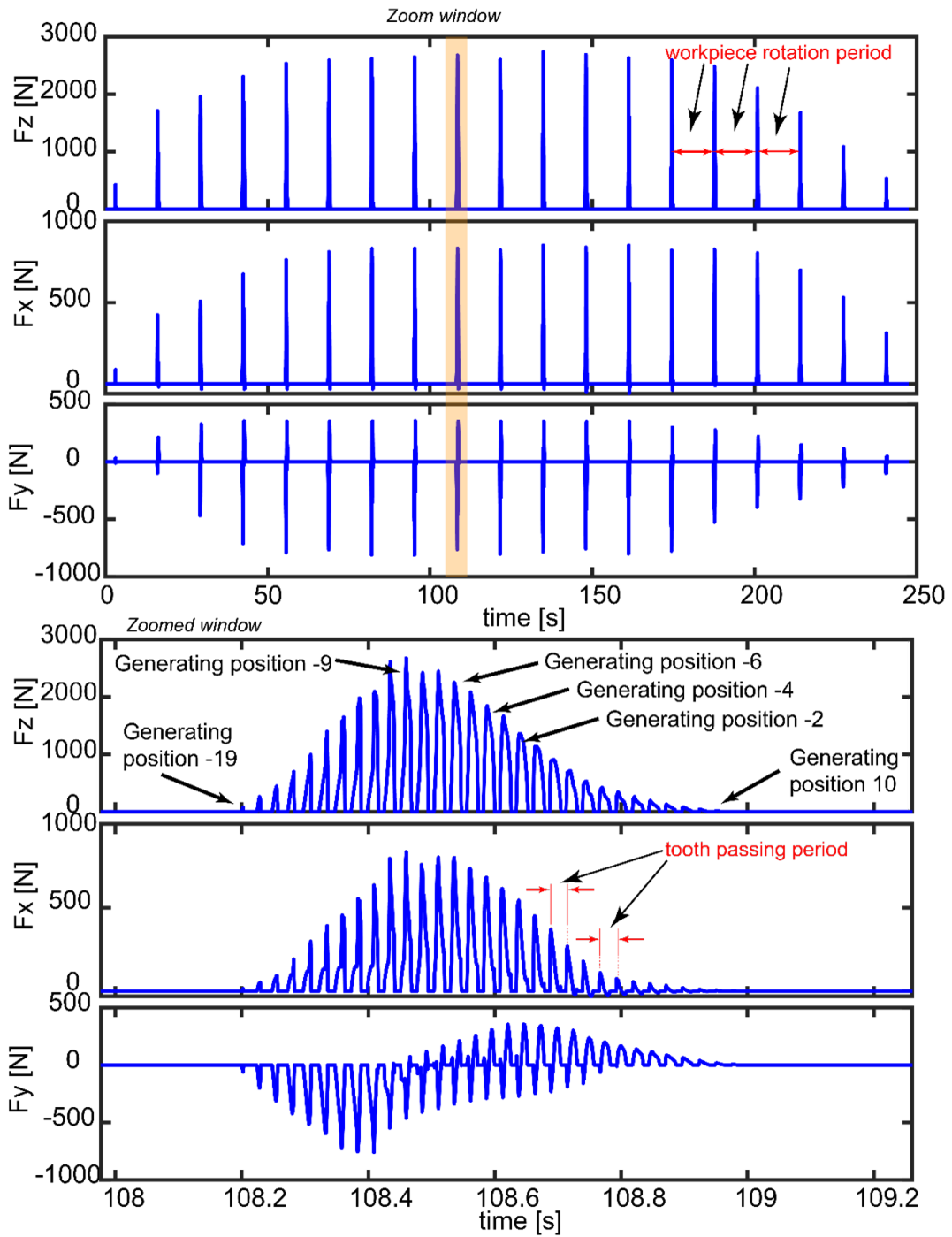Figure A.1: Hobbing simulation for a single tooth gap workpiece

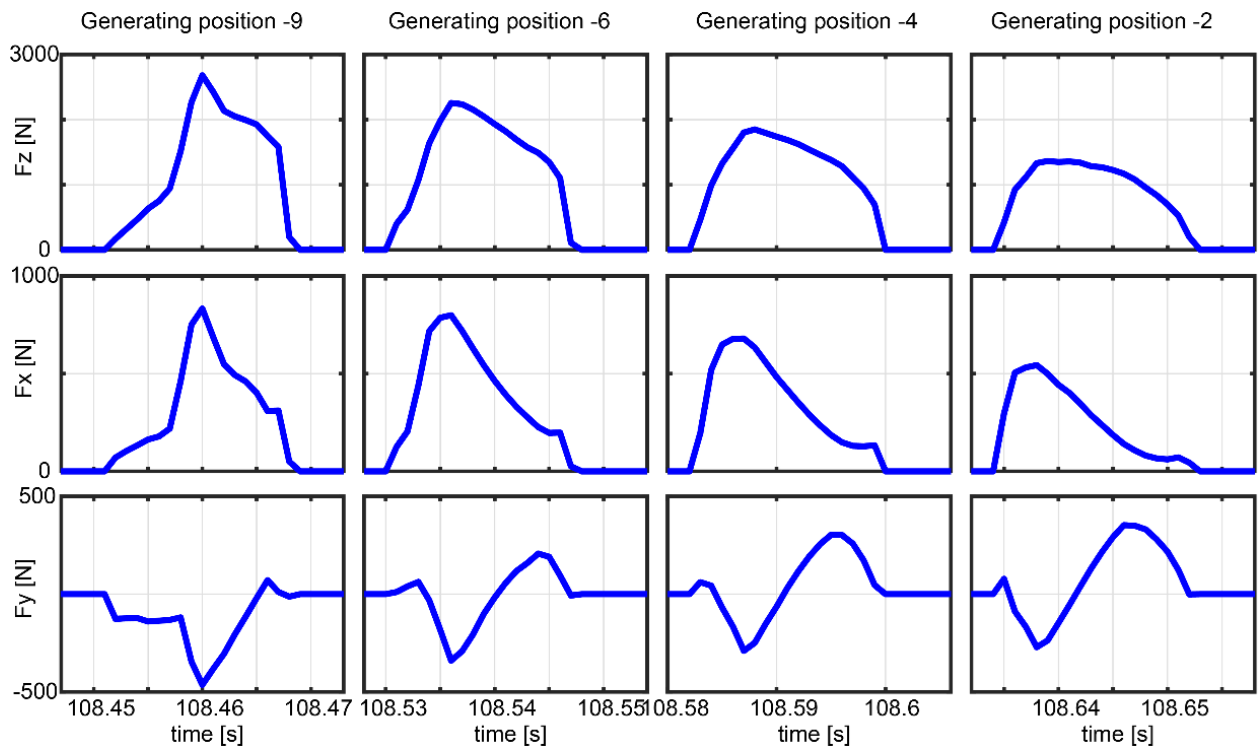Figure A.2: Prediction results for the case study presented in [56]

Figure A.3: Predicted cutting forces in different generating positions for the case study in [56]

Comparison of the developed model predictions results and the predictions obtained in [56] are shown in Figures A.3 and A.4. As can be verified, comparison between the force profiles and magnitudes predicted with the proposed model and those in [56] generally show good agreement. Nevertheless, there are also discrepancies, which may be attributed to the cutting force coefficients that are used in the simulations, as well as further assumptions that would be needed, to create a closer simulation to the conditions tested in [56].
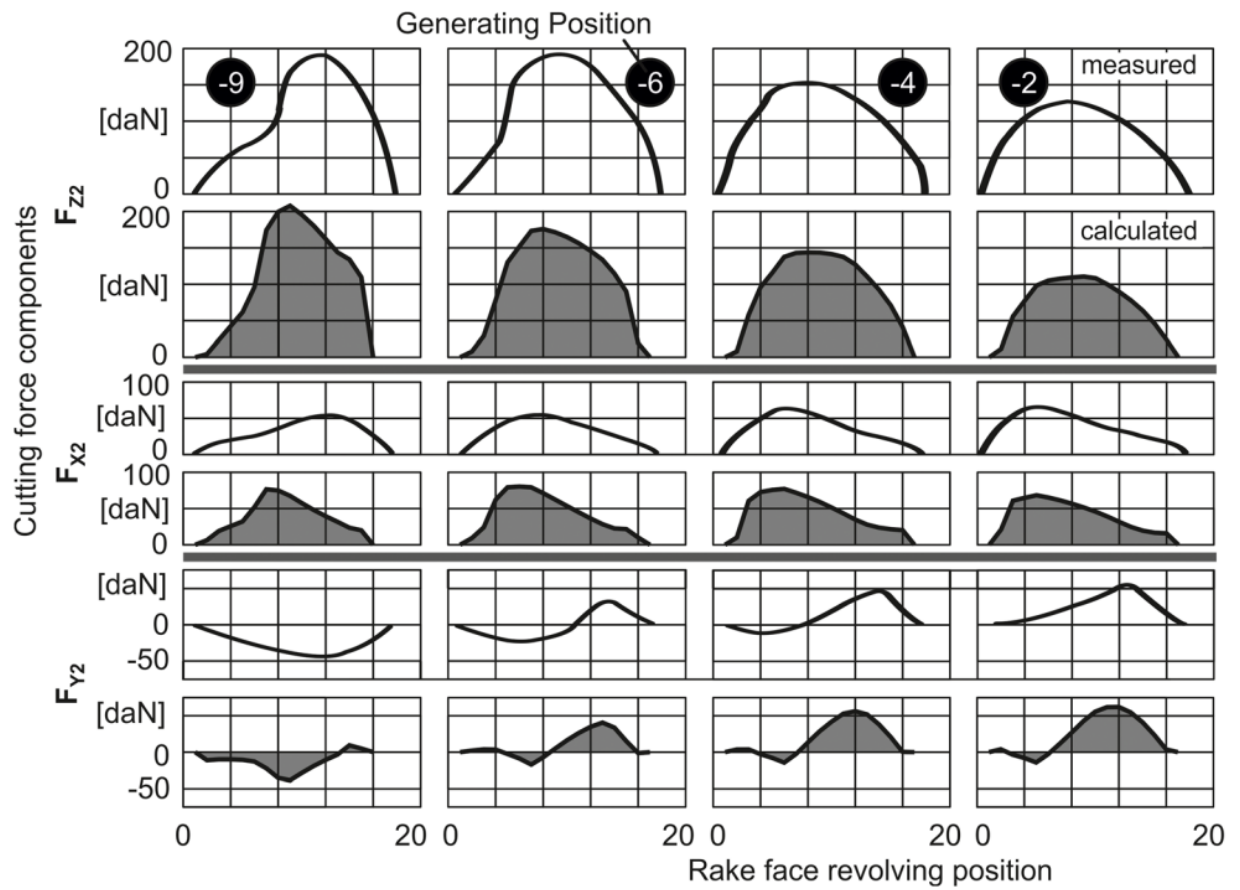
Figure A.4: Predicted and measured cutting forces in [56]